THE UNIVERSITY OF CHICAGO

QUANTUM FLUIDS IN A BOSE-HUBBARD CIRCUIT

A DISSERTATION SUBMITTED TO
THE FACULTY OF THE DIVISION OF THE PHYSICAL SCIENCES
IN CANDIDACY FOR THE DEGREE OF
DOCTOR OF PHILOSOPHY

DEPARTMENT OF PHYSICS

BY
GABRIELLE LYA CASTIAUX ROBERTS

CHICAGO, ILLINOIS
DECEMBER 2023

To my family, friends, and to you, the reader!

"I wanna talk about what I have learned

The hard-won wisdom I have earned [...]

The people will hear from me

One last time" - *Hamilton*, Lin Manuel Miranda

TABLE OF CONTENTS

LIST OF FIGURES

LIST OF TABLES

ACKNOWLEDGMENTS

This thesis would not have been possible without the wonderful people around me, both in lab and at home, none of whom I can thank enough. I kept getting stuck writing this section because it seems so difficult to properly convey appreciation for the individuals and communities that have supported me through my PhD, and that mean so much to me - yet, I will still try!

First, thank you to my advisors, Dave and Jon. You come up with creative ideas that are incisive to the field and often orthogonal to what everyone else has been thinking about, and your infectious excitement is inspiring and energizing. Thank you for granting me patience and flexibility when I needed it early on in graduate school. Dave, I appreciate the deep insights you share into the intricacies of circuit QED during project discussions, your wizardry for proposing debugging solutions to baffling technical problems, and the vast wealth of experimental resources that you provide to students in your group. Jon, thank you for the time and effort you spend ensuring that your students understand the physics underlying our experiments at a fundamental level, your attention to the meta of how to do science, you general high energy, and for providing among many other things invaluable theory support to the experiments described in this thesis.

Thank you to Schusterlab and Simonlab, an absolutely lovely group of people! I am grateful for the supportive, kind, and enthusiastic lab culture that has persisted throughout my graduate time and across two different campuses. Special thanks to my partners on the Bose-Hubbard project, fellow graduate student Brendan Saxberg and postdoc Andrei Vrajitoarea. Brendan, you were the first one to welcome me onto the project and help orient me to experiment. Thank you for your wise teachings, whiz coding and simulation abilities, experimental creativity, and general good humor. Andrei, I have learned so much from your deep understanding of the field, methodical approach to debugging, and excellent scientific ideas. Thank you for your cheerful mentorship and dry humor (and tolerating my

puns). I'm very excited to see what you accomplish as a new faculty. Special appreciation as well to Margaret Panetta, part of the larger Schusterlab quantum simulation subgroup, an invaluable officemate, scientific partner, and fantastic friend.

Grad school would not have been the same without the community of fellow students in my UChicago physics cohort. Thank you for companionship during late-night pset sessions, the most fun I've ever had creating a two hour long sketch show, and generally many evenings playing boardgames and hanging out. Thank you also to the members of the intramural soccer and frisbee teams, Quantum Ball Effect and Accretion Disks. Together we stand strong against the professional schools (in spirit, if not in victory).

Thank you to my housemates throughout the years (all the more important given several years of pandemic). Aurora, thank you for teaching me to skateboard, your enthusiasm for holiday decorations, and being up for the absolute wackiest adventures. Jeri, I am in awe of your infections energy and high spirits, and deeply appreciate your scientific excitement. Mimi, for movie nights, excellent culinary taste, and proper appreciation of the value of good snacks. Lavanya, for braving the lab move together and finding joy in silliness. Anora, thank you for your care and shared adventures. Nasim, we have been roommates through college and into graduate school, and it has been a pleasure and an honor sharing these past seven years. It's rare these days and in academia to be able to live for so long with such a good friend. You have pushed me to learn new things and grow more confident. Thank you for adventures throughout Chicago and beyond, support during challenging times, fascinating discussions, and generally the best of times.

Finally, thank you to my parents, for your unconditional love and support. None of this would have been possible without you.

ABSTRACT

A central challenge of contemporary physics is understanding strongly correlated quantum matter at the microscopic level, with important applications in materials, medicine, and infrastructure. Particle-level dynamics and correlations are often inaccessible to conventional condensed matter experiments dealing with real solid-state materials, and simulating these systems on classical computers rapidly becomes intractable because of the large space of variables involved. Inspired by Feynman, one way to approach this problem is to recreate the physics of interest in pristine quantum simulators.

In recent years, microwave photons in superconducting circuits have proven to be a rich testbed for modeling many-body phenomena. This platform boasts excellent single-particle and single-site control, site-resolved readout, long quantum state lifetimes compared to the timescale of dynamics, flexible geometries, and prospects for engineered cooling, opening up a variety of avenues to showcase new techniques for gaining physical intuition about manybody physics.

In this thesis, we use superconducting quantum circuits to construct and probe strongly interacting quantum fluids in a 1D Bose-Hubbard circuit. We deterministically prepare fluid eigenstates of our system using particle-by-particle assembly and adiabatic control of lattice site detuning. Site-resolved readout allows us to characterize these multi-particle fluids and probe particle entanglement and correlations. This state preparation technique is reversible; combining it with a manybody Ramsey experiment, we prepare cat states of quantum fluids, and then localize the information about energy differences of these highly entangled and delocalized states into one qubit for measurement. With this single qubit measurement, we then extract information about the manybody eigenstates, the associated excitation spectrum, and thermodynamic observables, a compelling example of how control and measurement overhead need not scale with system size.

CHAPTER 1

INTRODUCTION

1.1 Quantum Simulation and Model Building

One of the defining dreams of 21$^{\text{st}}$ century physics is to understand and control materials at the quantum level. Such capabilities would enable huge leaps in active research areas such as high temperature superconductivity, quantum biology, and molecular chemistry, with valuable applications in medicine, materials, and infrastructure [1]. However, elucidating the quantum structure and dynamics of molecules or materials is a very difficult problem. When probing materials and chemistry in traditional condensed matter experiments, noise, disorder, and other unwanted processes can obscure the exact causes and mechanisms of delicate quantum effects; further, important microscopic quantities such as specific quantum correlation functions are often inaccessible to classical probes [2, 3].

A common method of tackling difficult problems in physics is building a model: making a smaller or simplified version of the system that still captures the fundamental physics of interest, but with better control, less noise, and the ability to access quantities that would otherwise be difficult to measure. Models can either be digital, for example running an aerodynamics simulation on a computer, or physical, such as building a windtunnel. Unfortunately, digitally simulating quantum systems on classical computers rapidly becomes computationally intractable even for our best supercomputers. The space of relevant variables in quantum systems grows exponentially in system size; for example, describing N interacting spins such as electrons in a metal requires 2^N degrees of freedom, such that simulating even just 300 particles would require at least 2^{300} bits. For reference, 2^{300} is more than the estimated number of protons in our observable universe. Feynman proposed a solution to this problem in keynote address in 1982, stating "Nature isn't classical, dammit, and if you want to make a simulation of nature, you'd better make it quantum mechanical" [4]. Physi-

cists have spent the last few decades developing techniques to build such quantum models: aiming to assemble quantum systems from the ground up, engineer desired Hamiltonians, and initialize, time-evolve, and measure quantum states [1, 5].

In this chapter, we will discuss approaches to quantum simulation (digital and analog) and offer a brief survey of current state-of-the-art quantum simulation experimental platforms. We will introduce the Bose-Hubbard model studied in this thesis, a deceptively simple Hamiltonian that nonetheless supports several quantum phases and provides a clean test-bed for state preparation and characterization techniques. Finally, we will provide an overview of this thesis' chapters.

1.2 Digital Quantum Simulation

One way to approach quantum simulation is to use a quantum device as a digital quantum computer [6]. In analogy to a classical bit which holds a binary value, either 0 or 1, a quantum bit (qubit) is any two level system that can be in a superposition of both its $|0\rangle$ and $|1\rangle$ state [7]. A quantum state can be thought of as a vector in complex space, rather than simply a number. A qubit state is described as $|\Psi\rangle = \alpha|0\rangle + \beta|1\rangle$, where α and β are complex numbers with $|\alpha|^2 + |\beta|^2 = 1$. A system of multiple qubits can also feature entanglement, where the state of one qubit cannot be fully described without also taking into account the state of other qubit/s with which it is entangled. With these properties, it is possible to carry much more information in an array of quantum bits than in a classical system. However, at the end of an experiment, measurement collapses the superposition and the final value measured is classical (with the probability of measuring a specific value after many experiment repetitions given by the squared amplitude of that state's complex coefficient). Despite this measurement constraint, the special quantum properties of superposition and entanglement allow for new kinds of algorithms that cannot be run on classical computers, with clever uses of interference to obtain the right answer; examples include Shor's factoring

algorithm, Grover's search algorithm, the boson sampling problem, and variational quantum eigensolvers (VQE) [7, 8].

In digital quantum simulation, the global Hamiltonian of interest is broken up into local Hamiltonian terms composed of discrete one- and two-qubit gates, $H = \sum_l H_l$ with H_l the local terms. If all the local Hamiltonians commute, unitary evolution is then given as $|\Psi(t)\rangle = U(t)|\Psi_0\rangle = e^{-it\sum_l H_l}|\Psi_0\rangle = \prod_l e^{-itH_l}|\Psi_0\rangle$. For many Hamiltonians of interest, these local Hamiltonians do not commute. Using the Trotter-Suzuki formula [9], one can bypass this problem by only applying each local unitary for a very short amount of time δt and then repeating the sequence to approximate continuous evolution,

$$|\Psi(t)\rangle \approx \left(\prod_l e^{-it/NH_l}\right)^N |\Psi_0\rangle. \tag{1.1}$$

In the limit of infinite N, the approximation converges. In this way, a fault-tolerant quantum computer could be used to investigate any Hamiltonian with great accuracy, operating as a universal quantum simulator! Currently however, noise limits both the physical scaling and the number of coherent gates that can be carried out on existing quantum computing devices. The largest devices with some degree of individual control are in 100s of qubits range; we are in what has been termed the NISQ (nosy intermediate scale quantum device) era. Numerous schemes have been proposed to encode quantum logic in redundant degrees of freedom enabling error detection and correction, with the goal of building logical qubits whose lifetime exceeds that of their constituent hardware [10, 11]. While there have been a number of exciting results in the past decade, with the break-even point for a single qubit reached first reached in 2016 [12], so far error correction has been limited to small numbers of qubits and often also to limited sets of errors.

1.3 Analog Quantum Simulation

In the absence of a universal quantum computer, near term physics results can still be achieved by using well-controlled intermediate scale devices as analog models for materials physics [13]. The goal is to map the Hamiltonian of a system of interest directly onto the quantum device over which we have control. For example, the Ising model describes interacting spins; from the point of view of relevant properties such as critical points, dynamics, and correlations, the results are the same if the spins are electron spins in a metal, Rydberg atoms in optical tweezers, or photons in circuit structures parametrically driven to recapture spin interactions. Analog quantum simulators are specific in purpose - they can only simulate the physics for which they have been built. However, unlike digital quantum simulators, they involve less control overhead and do not require large numbers of perfect gates. These simulators are especially useful in cases where specific rather than complete state information, such as two-body ordering, equation of state, or entanglement growth, is required. In recent years, analog quantum simulation experiments have provided valuable insights into: the interplay of disorder and dynamics in localization [2, 14–16]; Fermi-Hubbard models [17, 18] and mechanisms of high-temperature superconductivity [3, 19]; topological matter and the fractional quantum Hall effect [20–25]; time crystals [26, 27]; manybody scars [28]; measurement-induced phase transitions [29]; and open quantum systems [30–33], among many other topics.

Despite these many results in creating and probing a variety of manybody states, the analog quantum systems under control are just in the 100s of particles and/or sites, with academic circuit systems closer to 10s of sites. The reader may be unimpressed with these small systems sizes of the NISQ era, especially given that many of the features of smaller quantum simulation platforms (this work included) are still within the reach of being numerically solvable using classical computers.

One goal even for smaller simulators is to develop tools and mappings for preparing and

characterizing states of interest. How to implement Hamiltonian terms, prepare specific states out of an exponentially large Hilbert space, and extract parameters in a robust and efficient way are all non-trivial questions that smaller devices can tackle at our current level of hardware. Methods development in quantum simulation is an important creative space, similar to ideas for error correction or new gates in quantum computing world. Especially exciting prospects include recent development of programmable quantum simulators across several platforms, which combine analog platforms with the digital controls of quantum computers, opening new avenues for manybody preparation and characterization, as well as expanding the flexibility for one analog device to explore a range of parameter regimes [34–37].

Further, the arrangements of quantum particles prepared and probed in analog quantum simulators aren't just models, but quantum materials, albeit synthetic ones! In this sense, analog quantum simulators are a platform on which to perform condensed matter experiments on very small sample sizes. In providing a new platform to tinker around with condensed matter physics with a wealth of possible measurements and controls, synthetic materials can uncover open questions, or provide more intuitive ways of thinking about physics previously mostly discussed in theory but never realized in the lab, both in the cases of measuring particular effect signatures impossible to probe in traditional samples [2, 3, 19, 28], or exploring parameter regimes beyond natural analogs [26, 38–40].

Having motivated quantum simulation generally and in the context of our current technological capabilities, I will now introduce experimental platforms for quantum simulation, including the one used in this thesis, superconducting circuits.

1.4 Experimental Platforms

What makes a good quantum simulator?

Somewhat tautologically, we need to be able to operate our device in a regime where

quantum effects are important. Generically in any experiment, we want the system to be dominated by physics of interest rather than noise or loss (noise is low compared to the relevant energy scales, loss slow compared to timescale of dynamics and interactions). These requirements are particularly stringent if we want to observe quantum effects, a regime where physical parameters' discrete nature is only revealed when strongly isolated from the environment. Heuristically, to be able to operate in the quantum regime and address discrete eigenstates, we need states' linewidth to be narrower than the energy spacing between them. Further, we need the thermal background in our system to be low compared to qubit energies, so that we can confidently prepare specific states rather than just thermal states.

We also need the ability to build interesting Hamiltonians, the ability to prepare MB states and induce dynamics, and the ability to probe what is going on in our simulator. This is the great difficulty of quantum simulation and computation: we need very precise control and readout (ie strong coupling) to systems that we are trying to completely *decouple* from the outside world to avoid noise and loss and see quantum effects.

In the past decades, several different experimental platforms have risen to the challenge of designing and controlling quantum systems. Some of the major players include:

- **Ultracold atoms in optical lattices [41, 42]:** Atoms are trapped by lasers in a vacuum chamber, cooled with electric and magnetic fields, and loaded into an optical lattice made of several interfering laser beams forming a fully controllable periodic light structure. The main quantum degree of freedom used is the lattice sites' occupancy (is there an atom a given lattice site or not). High filling fractions of large lattices (up to 3000 atoms) can be achieved [1]. For emulating condensed matter problems, atom arrays neatly implement a lattice with identical particles interacting through spin or particle exchange (much like electrons in a material are identical, and can interact or hop between potentials defined by periodic arrays of atomic nuclei). Both bosons and fermions can be trapped; atoms can hop between lattice sites, and na-

tively interact with contact interactions; additional nearest-neighbor spin interactions can be encoded into the hyperfine Zeeman states. Lattice geometry, dimensionality, and depth can be controlled by choosing different configurations of interacting laser beams. Synthetic magnetic fields can be generated from global lattice shaking or laser-induced tunneling, and spatial light modulators (SLMs) can imprint patterns of disorder and doping. Quantum gas microscopes can perform site-resolved readout, and time-of-flight measurements can probe momentum distribution. Current challenges in the platform include engineering long range interactions, achieving not just local but site-resolved control and loading, cooling atoms even further (for example cooling all excitations in a given superfluid), and speeding up experiment cycle times. Many of the earliest manybody simulations of correlated particles were done in ultracold atom lattice experiments (one of the first results probed the Mott insulator to superfluid transition [43]).

- **Rydberg atoms in tweezers [44]:** Atoms in a vacuum chamber are individually trapped in optical tweezers, and excited to high valence states (Rydbergs) that have a blockade radius preventing other nearby atoms from being similarly excited to the Rydberg state. This is a great platform for investigating spin models: tweezers can be arranged in arbitrary lattice patterns, and Rydberg excitations can be mapped onto interacting spins in a magnetic field (both XY and ZZ/Ising models are possible); here the main quantum degree of freedom/"particle" is the Rydberg excitation. Because of the deep tweezer trap holding the atom in place, Rydberg atoms' motional degree of freedom does not need to be as extensively cooled when aiming to build a lattice. The Rydberg excitation is also higher energy than room temperature thermal background. For a while, this platform was limited by low filling fractions. This issue was addressed by starting with a larger array of tweezers, and then reconfiguring them so that only the filled ones formed a lattice (current lattice sizes range around 250 sites). Rydberg

atoms can be individually addressed, and read out with single-site resolution using quantum gas microscopes. Current challenges in the field include attaining particle exchange terms; it is challenging to place the tweezers close enough and couple them strongly enough to see Rydberg atom hopping between tweezers.

- **Trapped molecules [45]**: Molecules in a vacuum chamber are cooled and trapped in optical lattices. Molecules have rich internal structures, dipoles that give rise to longer range interactions, and can also be used to observe chemical reactions in real time/at the atom-by-atom level! However, because of their rich internal structure molecules are correspondingly difficult to cool and control, and to achieve good filling fractions in lattices. This is a platform still under active development, but very promising.

- **Trapped ions [34, 46]:** Atomic ions in a vacuum chamber are laser cooled and trapped in linear (Paul trap) or 2D (Penning trap) arrays, with state of the art array sizes of around 50 ions. The internal energy levels within each ion can be mapped to effective spins (main quantum degree of freedom used for simulation). Long-range and tunable spin-spin interactions are generated through collective lattice phonons; ions truly can implement all-to-all connectivity. Synthetic magnetic fields can be generated with appropriate laser drives. Ions can be individually controlled and read out (techniques developed for performing digital quantum computing on the platform). Current challenges in the field include scaling up while maintaining control given the very long-range connectivity, and implementing ion tunneling between lattice sites.

- **Electron spins in nitrogen vacancy centers[27]**: Nitrogen vacancy centers are a type of point defect in diamond, where a nitrogen atom is substituted for a carbon atom, leaving an unpaired electron which serves as the quantum degree of freedom to be controlled (can be mapped to a two-level spin after applying a magnetic field). Collections of such defects can be globally optically initialized, detected, and manipu-

lated, and experience long-range magnetic dipolar interactions. The spins are subject to multiple sources of disorder inherent to a given sample, and are thus a neat test-bed for studying localization effects. Many nitrogen vacancies can be created in a sample, and no cooling/trapping overhead is required. Challenges of this platform include lack of tuning knobs (nitrogen vacancy location, density, frequency, and coupling is determined by sample fabrication) and lack of individual site control and readout when many vacancies are closely packed together.

- **Photons in engineered waveguides and metamaterials [47]:** Chip-based or beamsplitter arrays can implement non-interacting boson models for photons, with the quantum degree of freedom used in simulation either photon polarization, path, or angular momentum. Photons can be manipulated and addressed with simple optical components, and be shuttled around in free space or waveguides. The challenges of this platform include generating interactions (some work has been done generating synthetic interactions through measurement, as well as confining photons to arrays of nanopillars to generate polaritons with weak interactions), controlled generation of single photon states, and detection of single photons.

- **Superconducting circuits [38, 48]:** Circuits are not at first glance an intuitive choice for a system with good enough quantum control to implement interesting quantum simulation; circuits are large, macroscopic objects with many electrons, loss channels, and degrees of freedom. This is the magic of superconductivity: at cold enough temperatures in certain metals, electrons condense into a collective wavefunction that can be described with just a few degrees of freedom and flows in the metal with no classical resistance/loss. Therefore, if we fabricate circuits out of the right metal and cool the circuit to below that metal's superconducting point, we can treat the collective excitations of these circuits (microwave photons), as fundamentally quantum-mechanical. In superconducting circuit quantum simulation, these photon excitations

act as particles, and the arrangement of circuit elements forms the lattices on which they move [38]. In vacuum, photons do not interact or have complicated momentum structures. However, when interacting with matter, photons can inherit properties of interest. Lattice geometries of circuit element sites enable interesting couplings and band structure. A circuit element known as the Josephson junction provides a lossless nonlinearity that allows the photons to interact. Challenges in the platform include the fact that photons are inherently lossy when coupled to an external environment for control. Because circuits are fabricated and thus vary some in specific geometry/parameters, not all elements are identical; extra control lines are needed to bring elements on resonance. Because of the extra drive control, circuit systems are still on the smaller side compared to atoms and ions; the biggest circuit chip with individual site control is around 400 qubits [49], with most academic groups closer to $10-20$ qubits. However, circuits also have a number of promising strengths. Lifetimes may be on the order of 10s-100s of μs for large devices [49, 50], but interactions are on the scale of 10ns of ns – circuits have a very strong interaction to coherence ratio; it is possible to observer physics of interest before the system decays (this also means circuits have very fast data collection times). Circuits also have extremely good single site control: individual sites can be driven and tuned around in frequency, and individually read out. The fact that photons are lossy actually opens up possibilities for dissipative stabilization and other engineered loss physics difficult to achieve in other platforms. Fabrication enables arbitrary lattice geometry and connectivity.

Though circuits are relatively new to the quantum simulation party, the past decade has seen a proliferation of exciting circuit results, with groups investigating among other things exotic band structures for photons [15, 39], artificial magnetic fields [23, 51], strong interactions in photonic lattices [16, 37], and engineered reservoirs for dissipatitive state preparation [31, 33]. In this work we concern ourselves with implementing the Bose-Hubbard

model.

1.5 Hubbard Models

Originally studied in the context of superfluid-insulator transitions in liquid helium [52], the Hubbard model describes bosonic particles hopping around a lattice with on-site (pseudo-contact) interactions. The Hamiltonian is given by

$$\mathbf{H}_{\mathrm{BH}}/\hbar = J \sum_{\langle i,j \rangle} a_i^\dagger a_j + \frac{U}{2} \sum_i n_i \left(n_i - 1\right) + \sum_i \delta_i n_i,$$

where J is the tunneling strength, U is the interaction strength, and δ is the variation in lattice site energy. In a superconducting circuit implementation, lattice sites are transmon qubits (capacitor combined with a Josephson junction) which act like a nonlinear quantum harmonic oscillator [53]. Particles are microwave photon excitations of these sites. Particle hopping terms are created by adding a coupler to connect neighboring transmon qubits. The interaction term comes from the Josephson junction nonlinearity, or the fact that two photons in one lattice site are a different energy than one photon in each of two lattice sites [38, 48].

Depending on ratios of different parameters, the phase of the Hubbard model ground state can be a Bose glass, a superfluid, a strongly interacting fluid, or a Mott insulator [52]. The model also offers a clean system to investigate phase transitions, localization, scrambling, reservoir engineering, and manybody dynamics more generally. We are one of several circuit groups around the world investigating Hubbard models in circuits! (See for example [16, 37, 39, 54, 55], and many more!)

In our lab, we have used a Bose-Hubbard simulator platform as a jumping-off point to investigate broadly applicable techniques for state preparation and manybody characterization. Our group's initial implementation of this model in circuits demonstrated dissipative

stabilization of the Mott insulating phase, see Ref. [31]. In the experiments in this thesis, we turned to preparing and exploring the properties of strongly interacting photon fluids.

1.6 Thesis Overview

In this work, we will discuss preparing fluids of light in a 1D Bose-Hubbard system, and using these fluids to explore new methods of state preparation and characterization. The following topics will be covered in order:

In Chapter 2, we will give a brief overview of the history and physics of strongly interacting fluids in 1D.

In Chapter 3, we will discuss circuit building blocks of our device in greater depth.

In Chapter 4 we will discuss tuning up and operating a Bose-Hubbard device.

In Chapter 5, we will explore adiabatic preparation of quantum fluids through deterministic control of lattice site detuning, as well as probe density profiles, density correlations, and entanglement of these states.

In Chapter 6, we will build upon our adiabatic preparation technique to generate superpositions of quantum states, interfere them, and localize the interference fringe into a single qubit for measurement. We will use this method to investigate thermodynamic quantities of strongly interacting fluids in 1D.

Finally in Chapter 7 we will conclude and discuss potential future paths for this work.

CHAPTER 2

BOSE-HUBBARD MODEL AND 1D FLUIDS

In this chapter, we will do an in-depth dive into the Bose-Hubbard model's properties and history, with the aim to build intuition and context for this type of physics. Since our system is one-dimensional (1D), there is a further body of theoretical work relevant to characterizing the manybody states of our system, which we will discuss as well.

2.1 Bose-Hubbard Hamiltonian In-depth Dive

The Bose-Hubbard model describes bosonic particles hopping around and interacting on a lattice. The Hamiltonian is given as

$$\mathbf{H}_{\mathrm{BH}}/\hbar = J \sum_{\langle i,j \rangle} a_i^\dagger a_j + \frac{U}{2} \sum_i n_i \left(n_i - 1\right) + \sum_i \delta_i n_i. \tag{2.1}$$

The a_i and $a_i^\dagger$ terms are the bosonic annhiliation and creation operators for site i, with bosonic commutation relations $[a_i, a_j^\dagger] = \delta_{ij}$. n_i is the number operator. The $a_i^\dagger a_j$ terms describe a particle hopping from lattice site i to lattice site j, with tunneling amplitude J; here, we restrict ourselves to nearest-neighbor hopping. The sum

$$J \sum_{\langle i,j \rangle} a_i^\dagger a_j \tag{2.2}$$

can be thought of as equivalent to kinetic energy. The

$$\frac{U}{2} n_i \left(n_i - 1\right) \tag{2.3}$$

term describes on-site particle interactions: there is an energy penalty of magnitude U to having more than one particle per site. (For example, with one particle on site i, this

term adds $1 \times (1-1) = 0$ energy; if there are two particles on site i, this term adds $2 \times (2-1)U/2 = U$ energy). If U is negative, the interaction will instead be attractive, and there will correspondingly be an energy gain to having more than one particle per site. δ_i describes the energy differences between lattice sites (disorder). This model is particle-conserving.

To build some intuition about the different ground states of the model, let's consider a few extreme cases in the in the case of repulsive interaction (positive U).

Case 1, only J terms: Here, the Hamiltonian is given by

$$\mathbf{H}/\hbar = J \sum_{\langle i,j \rangle} a_i^\dagger a_j. \tag{2.4}$$

This reduces to the tight-binding Hamiltonian familiar from solid state class! Eigenstates consist of particles delocalized across the lattice. With periodic boundary conditions, when a particle is first added to an empty lattice, the ground state will be the particle in an equal superposition of every lattice state. Since particles are bosons, the ground state is all particles occupying the same lowest-momentum state; without interactions, the particles cannot "see" each other. The ground state wavefunction can be written as

$$|\Psi\rangle \propto \left(\sum_i a_i^\dagger \right)^N |0\rangle. \tag{2.5}$$

With open boundary conditions, the wavefunctions is constrained to be zero at the edges, so instead we get a sinusoidal particle in a box state,

$$|\Psi\rangle \propto \left(\sum_i \sin\left(\frac{\pi(x_i+1)}{V+1} \right) a_i^\dagger \right)^N |0\rangle. \tag{2.6}$$

Since in the ground state all the particles are in the same lowest-momentum eigenstate, the ground state energy as a function of particle number is just given as $E(N) = N \times E_{|\Psi_{k=0}\rangle}$.

In 1D with open boundary conditions for example, $E(N) = N \times 2J\cos\left(\frac{\pi}{L+1}\right)$. In the limit of large lattice, the energy $\delta E/\delta N$ to add an extra particle goes to zero, or in other words, the state is compressible. The states of this Hamiltonian are said to be in a superfluid phase.

Case 2, only U terms: Here, the Hamiltonian is given by

$$\mathbf{H}/\hbar = \frac{U}{2}\sum_i n_i\,(n_i - 1). \tag{2.7}$$

This Hamiltonian commutes with the lattice number operator n_i; in the ground state, all sites have a well-defined number of particles. At even filling with n particles per site, the ground state wavefunction is

$$|\Psi\rangle \propto \prod_i \left(a_i^\dagger\right)^n |0\rangle. \tag{2.8}$$

Adding particles to an empty lattice at first costs no energy. When all sites have one particle, adding an additional particle to the lattice costs energy U (at least one site is going to have to have two particles on it!). There is a large cost to adding another particle; we say this state is "gapped" in energy and is thus an insulator, called here "Mott insulator." To understand how the energy to add another particle (i.e. the chemical potential) changes at higher and higher filling more explicitly, consider the following: say I attach my Bose-Hubbard lattice to an external bath of particles, such that adding a particle to the lattice is favorable in energy by amount μ. Adding particles up to unit filling (one particle per site) doesn't cost any energy, so the lattice will completely fill. To add an extra particle beyond that costs U. If $\mu < U$, no new particles will enter the lattice. As soon as $\mu = U$, since the energy gain and energy penalty terms cancel out exactly, it is once again net zero energy to add particles. The lattice will completely fill up to two particles per site. This is the structure of a Mott insulator: as the external chemical potential is changed, the phase diagram exhibits plateaus of constant particle number gapped by energy U.

Case 3, both U and J terms: The ground state phase diagram when both terms

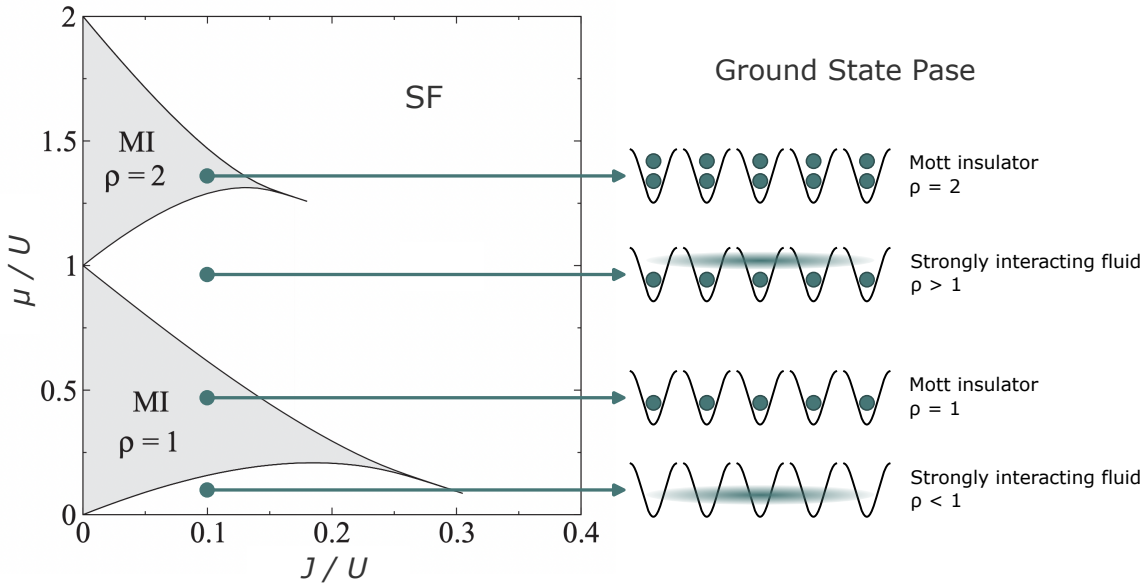

Figure 2.1: **1D Bose-Hubbard Phase Diagram** This figure is adapted from Ref. [56].

are present is presented in Fig. 2.1, where the y-axis is the chemical potential per particle normalized by U and the x-axis is the J to U ratio. Consider, for example, the case where $J/U = 0.1$. Here, there are both strong interactions and hopping terms. The presence of hopping terms means configurations where particles are smeared out in a superposition across the lattice are favorable from a kinetic energy standpoint, but because of interactions the particles can now "see" each other and take an energy penalty if they spread onto the same site. Particles still delocalize, but can no longer all go into the same state. Adding particles now requires energy, albeit less than U – the state is still compressible. One can imagine that pushing in a particle requires existing particles to be confined to a smaller volume (since they cannot occupy whatever site the new particle is in) – it takes some energy to compress the existing particles. This regime is the "strongly interacting fluid" regime. As the external chemical potential is increased, the density of the strongly interacting fluid increases until it hits unit filling. To add another particle at this point takes energy $\approx U$. As chemical potential is further increased but still below μ, the lattice remains at unit filling (Mott insulator lobe $n = 1$) until $\mu \approx U$, at which point we see another strongly interacting fluid

region. As $J \approx U$, the energy gained by delocalizing starts to out-compete the repulsive interactions; the energy bands of the strongly interacting fluids start to meld together and we get a superfluid regardless of U; the gap closes.

Thus, the Bose-Hubbard models provides a few interesting parameter ranges to explore; Mott insulators, $J \gg U$ superfluids, and $U \gg J$ strongly interacting fluids [52]. There are also many variations on this basic Bose-Hubbard model, including models with longer range interactions [37], disorder [15, 16], confining potentials [57], and hopping phases giving rise to synthetic magnetic fields or synthetic spin degrees of freedom [51, 58].

2.2 Realizations of the Bose-Hubbard Hamiltonian

The Bose-Hubbard model was first studied theoretically in the context of phase transitions for superfluid helium [52]. In 1998 it was noticed that the model could be implemented in optical lattices with cold atoms, where the trap depth determines the tunneling rate [59]. Atoms are loaded by starting the system in a Bose-Einstein condensate and then turning on the optical lattice lasers. Greiner et al. demonstrated the first realization of such a Bose-Hubbard lattice in experiment [43]; similar realizations in many other groups soon followed [42]. In these optical lattices, it is possible to use Feshbach resonances to independently tune the interaction U and explore the full U/J parameter space; time-of-flight (TOF) measurements to probe momentum space distributions; optical gas microscopes to readout on-site population and position-space correlation functions; laser configurations to change geometry and imprint fixed disorder patterns; and global lattice shaking for synthetic magnetic fields [42].

Bose-Hubbard models can also be realized in superconducting circuits, where sites are implemented as transmon qubits, particles as microwave photon excitations of the qubits, tunneling (J) as capacitive coupling between the qubits, and onsite interactions (U) as transmon anharmonicity (with U negative since the transmon anharmonicity is negative) [53]. The strength of circuits as a platform is extremely good single-site control: not only can sites

be individually read out as in quantum gas microscopy, but the state of each site can be individually controlled through microwave drive lines for particle addition/subtraction and full state tomography, and lattice site energies (qubit frequencies) can be individually & dynamically tuned using flux bias lines [60, 61]. Each hopping term can be dynamically tuned using lattice site frequency modulation or through the addition of tunable couplers between neighbors [62, 63]. Since photons are inherently dissipative, superconducting circuits are also an excellent platform for studying Bose-Hubbard models in the context of open quantum systems and dissipative engineering [31, 33, 38]. Because of control overhead to correct for differences between lattice sites/qubits from the fabrication process, circuit Bose-Hubbard simulators involve fewer atoms/sites than atom simulators, but they have much better controls, and are well-equipped to explore complementary techniques to the atom experiments.

Previous research from our group explored dissipative stabilization of a Mott insulator in a 1D Bose-Hubbard model predicated on that state's impcomressibility/the manybody U gap [31]. In this thesis, we operate in the strongly interacting fluid regime of the phase diagram of the 1D Bose-Hubbard model, and investigate preparation and characterization of strongly entangled compressible manybody states.

We've introduced the Bose-Hubbard model. In the strongly interacting regime in 1D, there are a number of analytic expressions one can derive to describe the system that helped guide our inquires and describe the states we prepared. The following sections discuss these theories and derivations.

2.3 Tonks Gas and the Jordan-Wigner Tranformation: Mappings between Bosons and Fermions in 1D

If half the battle of quantum simulation is creating desired Hamiltonians, and the other half is guiding these simulators to specific desired manybody states of interest out of an

exponentially large Hilbert space, then the last half of the battle is then finding clever ways to probe and characterize these states. (I realize I have too many halves – there are a lot of battles in experimental quantum simulation, research is hard). Before descending into a dense forest of analytic expressions, let us first take a step back and ask, what properties of manybody states can we measure to learn about their structure? Here are a few:

- Eigenstate properties: wavefunction of eigenvectors in position space, wavefunction of eigenvectors in momentum space, correlation functions (e.g. spin ordering, phase coherence, etc.), entanglement (one body, manybody, how does it grow as a function of system area or volume)

- Ground state energy as a function of parameters such as particle number, volume, interaction strength, disorder; thermodynamic quantities corresponding to derivatives of ground state energy (temperature $T = 0$) and thermal states ($T \neq 0$) as a function of system parameters (for example $P = -dE/dV$, $\mu = dE/dN$)

- Dynamics, excitation spectrum/quasiparticle energies, speed of sound, quantum walks, measures of ergodicity/integrability

- Effect of adding disorder and impurities, for example exploring cases where different lattice sites have different energies, hoppings, or different species of particles

Since one of quantum simulation's strengths is providing detailed insight into a system by building intuition from the ground up, we often start by characterizing ground states which tell us interesting facts about the target Hamiltonian's underlying structure, and then after that start adding in excitations and exploring dynamics in a controlled fashion.

When wondering how a particular model will behave, it is often useful to see what theorists have to say about it. Interacting bosons do not *a priori* have easy to derive expressions for the observables we listed above. However, in 1D bosons with strong repulsive interactions are well described by the Tonks-Girardeau gas formalism. A Tonks-Girardeau

(TG) gas is a set of particles confined to one dimension in a continuum where the interactions are so strong that the particles can be said to be hardcore, i.e. it is extremely costly to have two particles on one site. In 1D, this means that particles cannot pass each other, since to do so they would have to hop over each other with great energy cost. Rather than collapsing into a simple condensate where the wavefunction is nearly a product of single-particle states, the TG boson wavefunction exhibits zeros whenever two bosons occupy the same position in space [64, 65]. Girardeau made the observation in 1960 that this constraint can be implemented mapping it to the Pauli exclusion principle and related hardcore bosons to non-interacting spinless fermions. Specifically,the bosonic wavefunction of N particles $\Psi_B(x_1, ..., x_N)$ can be written as:

$$\Psi_B(x_1, ..., x_N) = S(x_1, ..., x_N)\Psi_F(x_1, ..., x_N) \tag{2.9}$$

where $\Psi_F(x_1, ..., x_N)$ is the wavefunction of a 1D gas of non-interacting spinless fermions and $S(x_1, ..., x_N) = \prod_{i>j=1}^{N} \text{sign}(x_i - x_j)$ compensates for the sign change whenever two particles in Ψ_F are exchanged, yielding a wavefunction that follows Bose statistics [66, 67]. For quantities where the sign term does not affect measurement, observables for the bosonic particles in 1D will be the same as if they were fermions! This holds for a number of interesting properties that have very convenient closed-form expressions once mapped to non-interacting fermions, including position-space wavefunction and pair correlation function of eigenstates of the Hamiltonian, energy spectrum, and thermodynamic quantities. The mapping is not universal to all observables; for example, the density matrix of a non-interacting fermion gas is different from that of the strongly interacting boson gas since in this case the sign function does not cancel out [66].

If the gas in question is on a lattice, a corresponding mapping may be done using the the Jordan-Wigner transform [68], which maps spin operators onto Fermi operators. First, we

go from hardcore (strongly interacting) bosons to Pauli spin-1/2 operators for each site i:

$$\sigma_j^+ = a_i^\dagger \sqrt{1-n_i}, \quad \sigma_j^- = a_i \sqrt{1-n_i}, \quad \sigma_j^z = 2n_i - 1, \tag{2.10}$$

Next, relate $S = 1/2$ spins to fermions by defining operators that implement the desired exchange statistics $\{f_i f_j^\dagger\} = \delta_{ij}$:

$$f_i^\dagger = \left(e^{+i\pi \sum_{k=1}^{i-1} \sigma_k^+ \sigma_k^-}\right) \cdot \sigma_i^+ \tag{2.11}$$

$$f_i = \left(e^{-i\pi \sum_{k=1}^{i-1} \sigma_k^+ \sigma_k^-}\right) \cdot \sigma_i^- \tag{2.12}$$

$$f_i^\dagger f_i = (\sigma_i^z + I)/2 \tag{2.13}$$

Note that the definition of the fermionic operators is non-local with respect to the bosonic operators (spin operators): the phase of a given raising or lower operator depends on an entire chain of operators to the left of the site the fermionic operators are defined with respect to (equivalent to the sign function in the continuum Girardeau mapping). One should not think of adding a boson in the lattice site basis as equivalent to adding a fermion; they are different eigenbases that offer complementary ways of viewing the same Hamiltonian, with the same spectrum, thermodynamics, and because $f_i^\dagger f_i = a_i^\dagger a_i$ the same density functions.

Having worked through the mapping between strongly interacting bosons and non-interacting fermions in 1D, in the next section we will proceed to detail what theoretical predictions we can actually make about the observables we care about.

A quick aside for the reader who may be interested in reading the original theoretical papers on 1D gases, a brief review and set of definitions for common terms:

- Bethe Ansatz (1931): ansatz for finding ground state wavefunctions of manybody models, applicable to 1D lattice problems [69]. (Fun fact: the original paper remains untranslated. The ambitious reader is encouraged to learn German.)

- Jordan-Wigner (1928): mapping from local spin operators to delocalized fermionic operators. Helpful for analytically solving spin problems such as the Ising model or XZ model; often used in quantum simulation with qubits, where qubits can naturally be described as spins and then mapped to fermions. Originally derived for 1D systems only, has since be extended to arbitrary dimensions [66, 68]. (Another German paper for the linguistically-inclined.)

- Tonks-Girardeau gas (1960): a Bose gas in the continuum in 1D, with strong δ-function type interactions, in the limit where the interaction strength U -> infinity. The system can be mapped onto non-interacting fermions, and then solved analytically. [67]

- Lieb-Liniger model (1963): a model describing a Bose gas in the continuum in 1D, with δ-function type interactions, where U interaction strength can take any value. Wavefunctions can be solved for using the Bethe ansatz. [70, 71]

- Tomonaga-Luttinger liquid (proposed 1950, refined 1963, correctly solved 1965): a model describing the interacting properties of fermions in 1D, either interacting or not [72].

I also highly recommend Cazalilla's review of bosons in 1D Ref. [66].

2.4 Derivations for a 1D Gas on a Lattice

In the following, we will calculate the predictions for quantities that we measure in experiment in Chapters 5 and 6.

2.4.1 Negative U Problem and the Equivalence of Highest and Lowest Energy State

We want to explore the properties of the ground states of the repulsive Bose-Hubbard model $H_{\mathrm{BH}}(t)/\hbar = J\sum_{\langle i,j\rangle} a_i^\dagger a_j + \frac{U}{2}\sum_i n_i\,(n_i-1) + \sum_i (\omega_{lat} + \delta_i(t))n_i$, so that we can use all the useful theory described up above. However, the physical Hamiltonian implemented in our experiment has the sign of U and J flipped (ie, we are realizing the attractive Bose-Hubbard model); $H_{\mathrm{physical}} = -H_{\mathrm{BH}}$. Because the two Hamiltonians differ only by a minus sign, the eigenstates are the same, just with flipped eigenvalues. Since our system is dissipation-less, the dynamics and observables of the highest excited state of our physical model are the same as those of the ground state of the repulsive model (with reversed time and negative values for thermodynamic/energy observables because of the minus sign). Thus, we measure observables of the highest excited state of our system, which maps onto the ground state of a repulsive Bose-Hubbard Hamiltonian. For the rest of the thesis, we refer to the state we measure as the "ground state"; the eigenvectors are the same, and the analytic values we derive for the ground state quantities match our data up to a minus sign.

2.4.2 Finite-Size and Finite-U effects

The accuracy of the Girardeau's and Jordan-Wigner's mapping depends on the relative strength of the interaction term and the tunneling term; terms that break the mapping scale as powers of J/U (to first order they appear like fermion interactions) [73]. In our experiment $J/U = 0.04$, and all corrections are small compared to the size of the features we are interested in measuring. For example corrections to energy/chemical potential/pressure are small, on average 1.2 MHz, the same order of magnitude as deviation from exact numerics ($700 - 800$ kHz, see SI B.3.2).

The mapping onto fermions ONLY depends on interaction strength, and is not affected by the size of our lattice. However, if we want to use expressions for continuum physics for

our lattice model, then we start having to be careful; how quickly continuum expressions break down depends on the system's coherence length, and we do in our experiment see finite size effects, see Sections SB.3 and SA.4.

2.4.3 Wavefunction: 1 Particle

With only one particle, there are no other particles to interact with or experience exchange statistics with. Thus, it does not particularly matter if the particle is a fermion or a boson, and the interaction term is irrelevant.

From the tight binding model for a single particle in a 1D lattice with V sites, tunneling $-J$, and open boundary conditions, the eigenvector wavefunctions are:

$$|\Psi(x)\rangle = \sin\left(\frac{n\pi(x+1)}{V+1}\right) \cdot \frac{1}{\sqrt{\frac{V+1}{2}}}, \tag{2.14}$$

x discrete variable indicating lattice site 0, 1, etc. With V lattice sites, the system has V single particle eigenvectors: n runs from 1 to V. x_i is the lattice site index and runs from 0 to $V-1$. These eigenvector wavefunctions can be thought of as particle-in-a-box wavefunctions, or quasi-momentum states $|\Psi q\rangle$ with $q = n\pi/(V+1)$.[1]

Flipping the sign of J just changes which quasi-momentum state is the ground state. With J positive the $n = V$ quasi-momentum state is the lowest in energy, with J negative the $n = 1$ quasi-momentum state is the lowest in energy.

When measuring in the population basis, the density probability distribution is given by

$$|\Psi(x)\rangle = \sin\left(\frac{n\pi(x+1)}{V+1}\right)^2 \cdot \frac{1}{\frac{V+1}{2}}. \tag{2.15}$$

1. For particles in a box, or on a lattice with open boundary conditions, wavefunctions are constrained to be zero at the edges of the lattice. Unlike in an infinite system or periodic system, momentum eigenstates e^{ikx} are no longer eigenstates of the Hamiltonian; instead wavefunctions are sinusoids with appropriate boundary conditions $\propto e^{ikx} - ie^{-ikx}$; the magnitude of the momentum is well defined, but not its direction, hence "quasi-momentum" states.

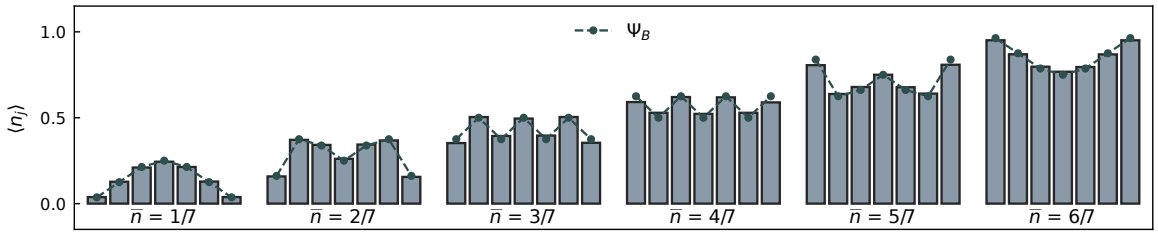

Figure 2.2: **TG Gas Wavefunction Compared to Exact Diagonalization** The bar plots correspond to the densities calculated numerically from exact diagonalization, while the dashed lines come from the analytic TG gas Bijl-Jastrow [74, 75] wavefunction. with slightly differences coming from finite U/J.

The probability distribution of the highest and lowest energy states in fact look the same, as the wavefunctions differ only by a phase on each lattice site.

2.4.4 Wavefunction: Many Particles

Given the assumption of infinite repulsive interactions, we can write a 1D ground state many-body wave function of the Bijl-Jastrow [74, 75] form $\Psi_B(\mathbf{x}) = \phi(\mathbf{x})\varphi(\mathbf{x})$, for $\mathbf{x} = (x_0, x_1, \ldots, x_N)$ the position of each particle, where ϕ describes particles' independent motion, and φ the effects of particle interactions. In our system, independent particle motion is described by

$$\phi(\mathbf{x}) = \prod_{i=0}^{N} \sin(\pi(x_i + 1)/(L + 1)) \tag{2.16}$$

i.e. all particles are in the same single particle ground state. The two-particle component is

$$\varphi(\mathbf{x}) = \prod_{i<j} |\cos(\pi(x_i + 1)/(L + 1)) - \cos(\pi(x_j + 1)/(L + 1))| \tag{2.17}$$

and implements the TG gas impenetrable boson requirement (not the most intuitive function, for the derivation see Ref. [76]). Using this trial wavefunction, we calculate density profiles for different particle numbers in the potential, and find very close agreement between exact diagonalization of our lattice and the results from the analytic wavefunction (see Fig. 2.2).

Wavefunctions of excited states for given volume and particle number can be solved analytically, but it's a pain [70]; for the purposes of our experiments we just calculated numerics.

A fun consequence of the strongly interacting limit is that we have particle-hole symmetry, as evidenced by the highest density wavefunction being equal to 1-the lowest density wavefunction; the probatility of one particle in seven sites is the same as the probability density of one hole in seven sites.

2.4.5 Correlation Properties

The TG gas also very closely captures the behavior of density-density correlators in our system, as shown in Fig. 5.8. Our system exhibits both particle repulsion and fermionization-induced Friedel oscillations predicted by TG gas model [66].

Note that because we have a a finite system, at larger x separations our results begin to diverge from the unconstrained TG gas result; because of finite size effects and the hard open boundary of our system, correlations drop at larger separations (see SI Fig. SA.4). This effect is captured in our numerics when we exactly diagonalize our system for up to 6 particles.

2.4.6 Energy Spectrum, Chemical Potential, and Pressure of Ground State

In the experiment described in this Chapter 6, we compare ground state energies of various particle and volume manifolds. This means we measure ground state observables, i.e. chemical potential, pressure, etc. for $T = 0$ and fixed entropy. The following thermodynamic calculations can be done assuming constant temperature and entropy. Our data matches these expressions up to a minus sign, as we measure the highest excited state of our system.

The energy eigenvalues for a single particle in a 1D fermionic lattice with V sites, tun-

neling $+J$, and open boundary conditions is

$$E_k = 2J\cos\left(\frac{\pi k}{V+1}\right) \tag{2.18}$$

where k are quasi-momenta.

Exercise 2.0: Calculate E_k for a single particle (since there is only one particle, it doesn't matter if that particle is a boson or fermion!) in a 1D lattice with V sites, tunneling $+J$, and open boundary conditions from the tight binding model. The main takeaway is that the "V+1" term comes from open boundary conditions.

The ground state energy of N fermions in a lattice, by the Pauli exclusion principle, is the sum of all single-particle energies from the lowest energy state up, here from $k = N$ to $k = N - V$:

$$E_N = \sum_{k=N}^{N-V} 2J\cos\left(\frac{\pi k}{V+1}\right) = -J\left[\csc\left(\frac{\pi/2}{V+1}\right)\sin\left(\frac{\pi(N+\frac{1}{2})}{V+1}\right) - \frac{1}{2}\right]. \tag{2.19}$$

This expression is used to derive thermodynamic quantities below.

To calculate E in the thermodynamic limit, we take ρ constant and send N and V to infinity:

$$\lim_{N,V\to\infty} E_N = \lim_{N,V\to\infty} -J\left[\csc\left(\frac{\pi/2}{V+1}\right)\sin\left(\frac{\pi(\rho V+\frac{1}{2})}{V+1}\right) - \frac{1}{2}\right] = \frac{-2JV\sin(\pi\rho)}{\pi}. \tag{2.20}$$

The chemical potential at constant entropy is defined as $\mu = \left.\frac{\partial E}{\partial N}\right|_{S,V}$. Plugging in the expression for E from Eq. 2.19 gives:

$$\mu = \frac{-J\pi}{V+1}\csc\left(\frac{\pi/2}{V+1}\right)\cos\left(\frac{\pi(N+\frac{1}{2})}{V+1}\right) \tag{2.21}$$

.

In the thermodynamic limit, sending N and V to infinity while holding $\rho \equiv \frac{N}{V}$ constant,

$$\lim_{N,V\to\infty} \mu = -2J\cos(\rho\pi). \tag{2.22}$$

The pressure at constant entropy is defined as $P = -\frac{\partial E}{\partial V}\Big|_{S,N}$. Plugging in the expression for E from Eq. 2.19 yields:

$$P = \frac{J\frac{\pi}{2}}{(V+1)^2}\csc\left(\frac{\frac{\pi}{2}}{V+1}\right)\left[\cot\left(\frac{\pi/2}{V+1}\right)\sin\left(\frac{\pi(N+\frac{1}{2})}{V+1}\right) - (2N+1)\cos\left(\frac{\pi(N+\frac{1}{2})}{V+1}\right)\right] \tag{2.23}$$

.

In the thermodynamic limit, holding ρ constant while sending N and V to infinity,

$$\lim_{N,V\to\infty} P = 2J\left(\frac{\sin(\pi\rho)}{\pi} - \rho\cos(\rho\pi)\right). \tag{2.24}$$

2.4.7 Energy Spectrum of Excited States

For single particles, the energy spectrum of eigenstates other than then ground state is given by the tight binding model;

$$E_n = -2J\cos\left(\frac{n\pi}{V+1}\right) \tag{2.25}$$

.

The full energy spectrum of states with many particles starts to get more complicated analytically, especially with finite interactions at the U-band starts to interact with the normal band. We solve the system numerically in Fig. 2.3.

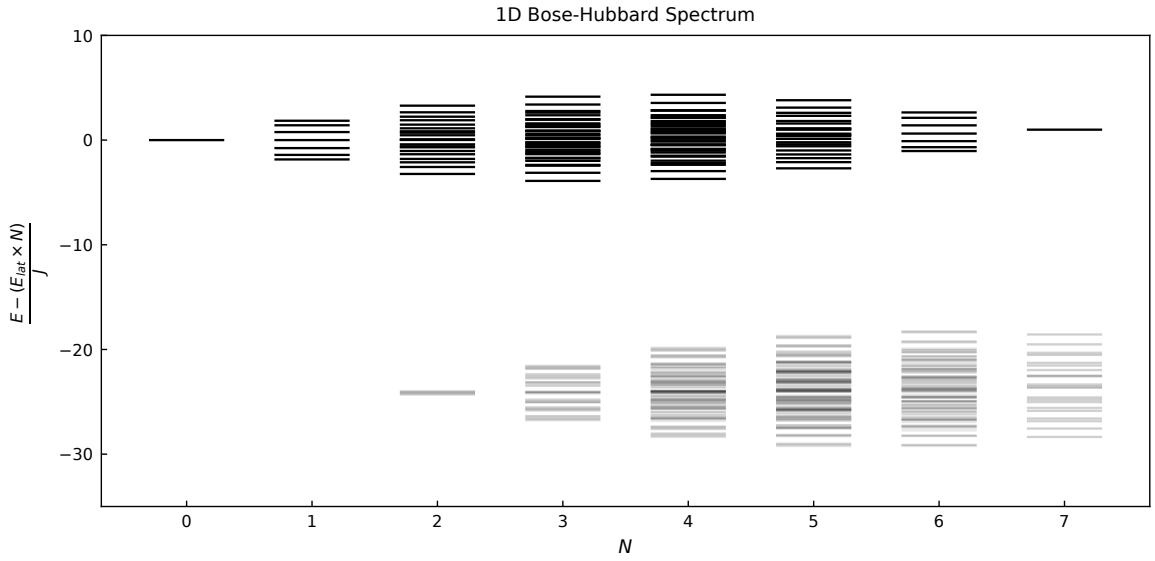

Figure 2.3: **1D Bose-Hubbard Spectrum** States in dark are excitations of the hardcore band (ie no more than one particle per site), which extends in energy from $-4J$ to $4J$. Energy levels are grouped by particle sector. States in light grey are doublon excitations (one site has two particles), centered around $U = -24J$. The rest of the spectrum is not shown in this figure.

2.5 Simulations

To verify our experimental results, we simulate properties and dynamics of this system using the python package Qutip. In our simulations, we use a Hamiltonian of the form:

$$\mathbf{H}_{\mathrm{BH}}/\hbar = -\sum_{\langle i,j\rangle} J_{ij} a_i^\dagger a_j + \frac{U}{2}\sum_i n_i\left(n_i - 1\right) + \sum_i \left(\delta_i + \omega_0\right) n_i.$$

plugging in experimentally measured values for J, U, and δ. We truncate our Hilbert space at the $|3\rangle$ state (3 photons) or $|2\rangle$ state (2 photons) of each qubit depending on the intensity of the simulation, choosing the lower cutoff for time-intense simulations. We operate in the energy restricted (ENR) subspace of 6 total excitations for our simulations for faster computation times. We numerically diagonalize the Hamiltonian in order to obtain the eigenergies and eigenstates to verify many-body state spectrum, thermodynamic quantities,

profiles, global entanglement, and $g^{(2)}$.

In order to simulate our dynamics and obtain theory for adiabiticity times, we numerically solve the Schrodinger equation for different eigenstates of the Hamiltonian.

CHAPTER 3

CIRCUIT QED BACKGROUND

So, how do we actually build the Hamiltonian and controls that we want out of superconducting circuits?

3.1 Circuit QED Review

For an excellent overview of all of the building blocks we will discuss in this section, see Brendan Saxberg's thesis "Creating Compressible Many-Body States of Light through Adiabatic Tuning of Disorder" Chapter 2 [77], where he discusses his considerations when designing the chip used in this experiment. I will give a shorter review of the main highlights here.

When building a quantum simulator, it is important to consider what components you have accessible in your particular platform, and how to use them to both a) implement the Hamiltonian to study and b) enable control over system (to probe states, prepare states, or programmatically change Hamiltonian properties). In this section, we will review the components of our Bose-Hubbard simulator step-by-step.

3.2 Creating the Bose-Hubbard Hamiltonian

First, we create a system described by the Bose-Hubbard Hamiltonian: the 1D chain of qubits highlighted in red in Fig. 3.2. How much flexibility do we have to engineer different ratios of theses parameters?

Lattice sites and U: Lattice sites are implemented as transmon qubits, and particles as the microwave photon excitations of these qubits [38]. U is determined by the transmon qubit anharmonicity. For a transmon qubit, the energy of adding a photon and the anharmonicity

$$H_{BH}/\hbar = -J \sum_{\langle i,j \rangle} (a_i^\dagger a_j + a_j^\dagger a_i) + \frac{U}{2} \sum_i n_i(n_i - 1) + \sum_i \delta_i n_i$$

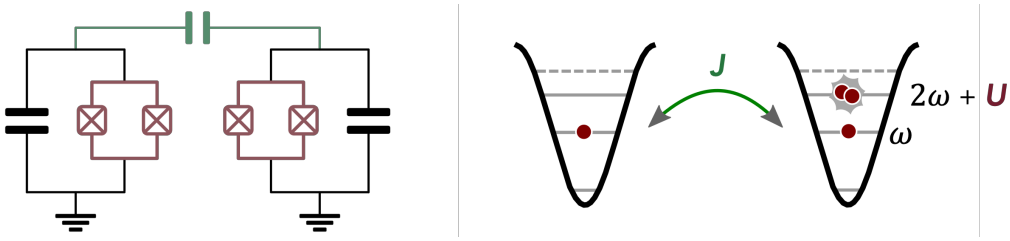

Figure 3.1: **Elements of a Bose-Hubbard Chain** The transmon qubits (circuit on the right) serve as lattice sites for photons (diagram on the left), where interactions come from the qubit anharmonicity U and the tunneling J arise from the capacitive coupling (green) between the two sites.

are:

$$\omega_{01} \approx \sqrt{8E_J E_C} \tag{3.1}$$

$$U \approx -E_C \tag{3.2}$$

where E_J is the Josephson energy and E_C is the transmon charging energy. Both are fixed by fabrication. $E_C \propto 1/C_\epsilon$, so the magnitude of U can be adjusted by changing the total capacitance of the qubit to ground. $E_J \propto 1/R$ the room temperature resistance of the junction, which can be adjusted by changing the junction's area and oxide thickness during the fabrication process (see Refs [77, 78] for exact derivations). To stay in the transmon regime and maintain long phase coherence, keep $E_J \gg E_C$.

Tunneling J: The tunneling term J arises from the capacitive coupling between qubits, also in our case fixed by fabrication:

$$H_{tunnel} = -J(a_i + a_i^\dagger)(a_j + a_j^\dagger) \tag{3.3}$$

with the tunneling energy

$$J \approx \frac{C_g}{2\sqrt{C_i C_j}} \sqrt{\omega_i \omega_j} \tag{3.4}$$

with C_g the capacitance between the two qubits and $C_{i/j}$ the respective capacitance of each qubit to ground (see Refs [77, 78] for exact derivations).

Combined, this gives us the Hamiltonian:

$$H = -J \sum_{\langle i,j \rangle} (a_i + a_i^\dagger)(a_j + a_j^\dagger) + \frac{U}{2} \sum_i n_i \left(n_i - 1\right) + \sum_i \left(\omega_{\text{lat}} + \delta_i\right) n_i \tag{3.5}$$

Applying the rotating wave approximation, we can throw out terms that don't conserve energy

$$H = -J \sum_{\langle i,j \rangle} (a_j^\dagger a_i + a_i^\dagger a_j) + \frac{U}{2} \sum_i n_i \left(n_i - 1\right) + \sum_i \left(\omega_{\text{lat}} + \delta_i\right) n_i \tag{3.6}$$

To recover the form of the Bose-Hubbard model often quoted in literature, rotate the system at the lattice frequency:

$$H_{\text{BH}} = -J \sum_{\langle i,j \rangle} (a_j^\dagger a_i + a_i^\dagger a_j) + \frac{U}{2} \sum_i n_i \left(n_i - 1\right) + \sum_i \delta_i n_i \tag{3.7}$$

where $\delta_i = \omega_i - \omega_{lat}$.

Hurray! We have the Bose-Hubbard Hamiltonian that we wanted. We can design different chips with different ratios of U/J, but in a given chip the ratio is fixed by the physical capacitances and junction parameters.

3.3 Designing Controls and Probes

What controls and probes have we designed into this sample?

Frequency Tunable Qubits. In this device, each transmon's nonlinearity comes not

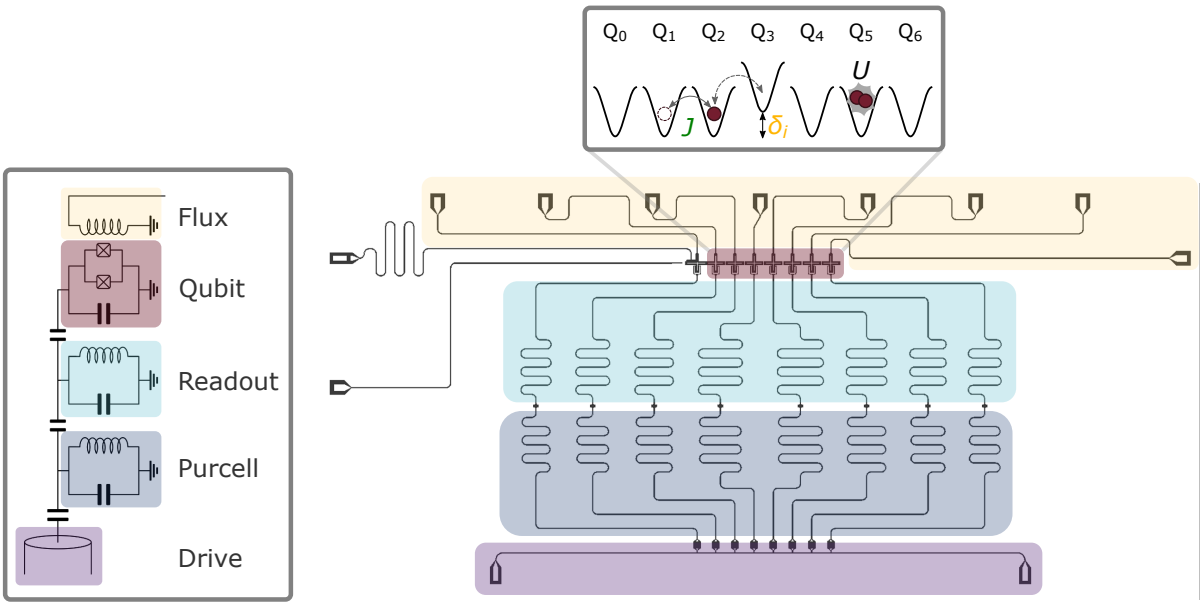

Figure 3.2: **BH circuit chip** Pictured here is our device, with a diagram of each component on the left. The qubit chain is highted in red, the frequency tuning (flux) lines are highlighted in yellow, the readout resonators are highlighted in light blue, the Purcell filters are highlighted in dark blue, and the communal drive/readout line is highlighted in purple.

from one Josephson junction, but two in a SQUID loop. The Josephson energy can be tuned or modulated by passing current through this loop [53, 77, 78]:

$$E_J(\Phi) = (E_{J1} + E_{J2})\cos(\pi\Phi/\Phi_0)\sqrt{1 + d^2\tan^2(\pi\Phi/\Phi_0)} \tag{3.8}$$

$$E_J^{max} = E_{J1} + E_{J1} \tag{3.9}$$

$$E_J^{min} = |E_{J1} - E_{J1}| \tag{3.10}$$

$$\omega(\Phi) = \sqrt{8E_J(\Phi)E_c} - E_c \tag{3.11}$$

where E_{J1} and E_{J2} are the respective Josephson energies of the two junctions in the SQUID loop, Φ is the external magnetic flux through the loop, Φ_0 is the superconducting flux quantum, and $d = \frac{E_{J1}+E_{J2}}{E_{J1}-E_{J2}}$. In our device the tuning range is from $3 - 6$GHz.

Each qubit has its own individual flux tuning line (highlighted in yellow in Fig. 3.2). This way, we can choose the frequency configuration of our qubit, and can modulate a

qubit's frequency.[1] Our sample also has a magnet attached to the packaging, allowing us to additionally globally tune flux across all qubits SI D.2.

Readout and Purcell Resonators. Each qubit has its own individual readout resonator, highlighted in light blue in Fig. 3.2. Using dispersive readout, this allows us to read out the qubit state in the population basis [78] in a non-demolition way.

In a system where a qubit is dispersively coupled to one readout resonator, there exists a loss channel for qubit excitations leaving the system through the measurement channel of the resonator referred to as Purcell loss. By adding another element, a Purcell filter, between the resonator and the 50-Ohm environment we can re-shape this impedance and increase the limited transmon lifetime we would face from this loss process. To implement this simply, we add yet another linear resonator between the existing readout resonator and the environment, highlighted in dark blue in Fig. 3.2. This new filter resonator is designed with a large linewidth centered at the readout frequency such that photons at the readout frequency pass to the measurement environment while photons at the qubit frequency are mostly reflected.

Communal Drive and Readout Bus for Resonators. We have one communal drive line to probe qubits and resonators, highlighted in purple in Fig. 3.2, that all the resonator/Purcell pairs are connected to (and that all the qubits are connected to through the resonator/Purcell filters). There are several consequences of this:

All resonators will see a given tone sent through the feedline; we rely on frequency separation to selectively drive individual resonators. Since the resonators are narrow linewidth ($\sim 200 - 500$kHz) and spread comparitively far apart in frequency (~ 100MHz), with a narrowband drive one can address a given resonator and be far enough detuned from the others that the drive has no effect on the others. If one wants to probe multiple resonators at once, one can send in a drive pulse with several frequency components, each corresponding to the

1. Qubit frequency modulation can be used to generate new resonance conditions and/or tune couplings, see SI B.2.2.

resonators we want to drive (known as frequency multiplexing, see for example Ref. [79]).

Our wiring is set up to send microwave signals in from one side of the feedline, and to directionally deliver microwave signals out to our measurement setup to record the state of the resonators for readout on the other side of the feedline, see SI E for more details.

Communal Drive for Qubits We drive the qubits through the communal feedline as well; we also rely on frequency separation here (both between qubit and resonators, and qubit to qubit) to selectively drive individual transitions. If we want to address qubits locally, this means that we have to first arrange them in a frequency configuration where they CAN be driven locally, i.e. far enough apart ($\delta \gg J$) such that eigenstates look like particles localized on single sites. Since we are relying on frequency separation to not drive unwanted qubits, we also have to be careful about not driving qubits with pulses that are too short/that have large frequency spread for fear of hitting other qubits nearby in frequency. This is not an issue in systems with individual charge lines for each qubit.

Since we are driving each qubit through its resonator/Purcell pair, which each in turn are spaced out in frequency, we expect the coupling of each qubit to the feedline to be slightly different (i.e. each qubit will have a different π-pulse time).

Extra Elements Not Used in this work The astute reader will notice that there are two elements of our chip that I haven't discussed, two lines leading to the end of the qubit chain (unhighlighted in Fig. 3.2). One is a drive line coupled just to the edge qubit, the other is a lossy resonator also coupled just to the edge qubit. These two elements can be used for experiments in dissipative stabilization (see Ref. [31]), but were not employed in the experiments described in this work. For experiments in this thesis, the edge qubit was far detuned from the rest of the qubits and from the lossy resonator, to not introduce extra decay from the lossy resonator to the main lattice of qubits.

Summary and Outlook See SI C for a full table of measured parameters of the sample at operating points for the experiments described in this thesis.

When considering the next iteration of a quantum simulator platform, it is always worth asking what Hamiltonian terms you want to aim for and why, what controls you want and why, and for both cases what the particular strengths of your platform/your design are compared to the rest of what is being done in the field. Examples of circuit elements worth considering for future samples: tunable couplers between lattice sites enable control of the tunnelling in amplitude and phase (though also more hardware overhead), going from 1D to a ladder or a square opens up new kinds of physics, coupling all qubits to a waveguide generates beyond nearest-neighbor interaction [37], using different types of qubits such as fluxonia for lattice sites opens up new kinds of Hamiltonians, etc!

In this section we have reviewed sample design; sample fabrication, packaging, and measurement setup are detailed in SI D and E. The next section covers sample calibration.

CHAPTER 4

CHARACTERIZATION AND OPERATION OF A BOSE-HUBBARD DEVICE

4.1 Philosophy

This section will provide a step-by-step guide to characterizing and tuning up a Bose-Hubbard device once it is in a cryostat. The section is aimed at younger graduate students taking on the current sample or building a new but similar device. Many of the characterization steps we discuss here have also been covered in a more general context in other references; see Refs. [60, 61, 80, 81] for complimentary discussions.

This is a rather technical section, but I argue that tuning up a sample properly is *the core* of quantum experiment. Being able to quickly and accurately control a complicated device is at a fundamental level what enables accurate generation of desired Hamiltonians, trustworthy extraction of information about highly entangled states, and the flexibility of control needed for creative solutions to the problems of manybody state generation.

With that in mind, it is often helpful to begin a series of characterization tests with a clear idea of what exactly are the parameters you aim to measure and why they matter to the experiment. Are there certain characteristics that mean the sample will likely not be able to implement the experimental sequences you have in mind? How do the parameters measured compare with historic values? How long will you need to average to get clean signal? Etc.

4.2 Quick Aside: Qubit Configuration During Calibration

With flux-tunable qubits, we can decide where to place the qubit transitions, $\omega_0 1$ etc., in frequency (hereafter, I just say "qubit" for "qubit $\omega_0 1$ transition"). In general, for qubit

characterization, we place the qubits so that they are effectively decoupled from each other: we found best results by placing neighboring capacitively coupled qubits $\sim 400 - 500$ MHz apart and next to nearest neighbors $\sim 20 - 50$ MHz apart. This ensures that:

- $\delta_{nn} \gg J$ i.e. nearest neighbor detuning is larger than tunneling, so nearest-neighbor qubits are not significantly hybridized; eigenstates of our system correspond to particles localized to individual qubits, i.e. we can effectively treat the qubits as decoupled.

- $\delta_{nn} \neq U$ so populating an upper qubit does not shift the frequency of a lower qubit significantly compared the the bandwidth of our qubit drive (and vice versa), which can happen if the energy of having a particle in upper and lower qubit is close to the energy of two particles in the upper qubit (i.e. energy of $|11\rangle$ state is close to the energy of $|20\rangle$ state). We found having $\delta \gg U$ helpful for suppressing readout crosstalk.

- next two nearest neighbors are also detuned to avoid virtual transitions through intermediate qubits, and to be able to drive qubits individually relatively quickly without hitting other qubits close in frequency.

- $|\delta - \omega_{\text{lattice}}|$ is within the range of our RF tuning of qubit frequency, so that we can bring all qubits onto resonance during the course of an experiment. When operating on the slope of our qubits' ω vs. tuning flux curve, our range was typically on the order of $200 - 400$MHz (see Sec. E.)

- all qubits close enough to readout resonators for high-fidelity readout (in the current sample, anything above about 4GHz was acceptable).

A typical configuration is shown in Fig.4.1.

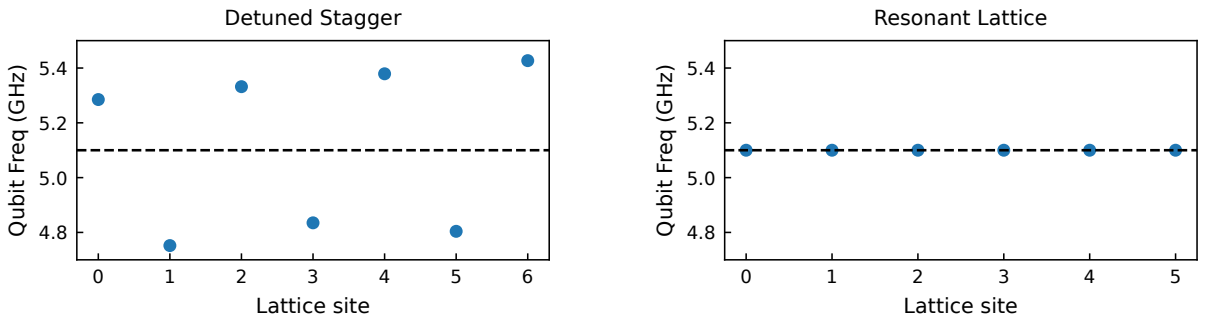

Figure 4.1: **Qubit Configurations** An example of qubit configurations used when: (left) qubits are detuned for individual control and readout; and (right) when qubits are on resonance in a lattice configuration.

Exercise 4.0: Calculate the eigenenergy shifts from the bare frequency and plot single particle eigvenvectors in the population basis with nearest neighbors 500MHz apart and next to nearest neighbors 30MHz apart. Plot eigenvalues as a function of neighboring detuning and next-to-nearest neighbor detuning. If you place neighors close to U apart, check the energy of adding a particle to either qubit a) starting from vacuum state or b) starting with the neighbor occupied.

4.3 Continuous Wave Measurement

The first set of measurements involve sending one or several continuous tones to the sample, and measuring the relative magnitude and phase of the signal that returns relative to the signal we send in. These measurements do not require preparing the qubits or resonators in any given state; we are just doing spectroscopy. Our device is set up to do "hanger" style measurements through a common feedline; refer to Ref [82] for the details of measuring resonators in transmission, reflection, or with a hanger.

Sanity check before starting continuous wave (CW) spectroscopy: Attach the signal source and signal readout to the fridge (we often use a VNA, or vector network analyzer), and do a large sweep in frequency at a power low enough to not fry any amplifiers.

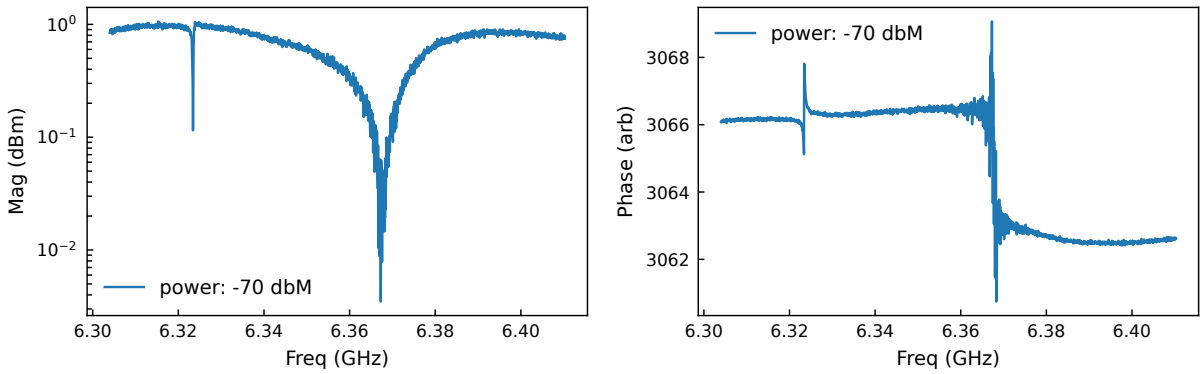

Figure 4.2: **Resonator-Purcell Scan** The resonator is the narrow feature on the left, the Purcell filter is the broad feature on the right.

Is the background you see what you expect if you add up all your attenuators and all your amplifiers? This is a great check to make sure you are attached to the right lines going to your sample, and that all the amplifiers (which are actice microwave components) are supplied with power. Here you can also check on circulators (for example, if the circulators only work from $4 - 8$ GHz, there should be a drop off in signal outside of that range) and filters, see Sec. E for the configuration used in our experiments.

4.3.1 Roll Call: Are Resonators and Qubits Present

Goal: Determine locations of resonators and Purcell filters in frequency by doing continuous wave single tone spectroscopy, and check if qubits are alive through "punch out" power sweeps on the resonators.

Step 1: Check if the resonators are visible. We first do a broad frequency sweep to identify the Purcell-resonator pairs. In the device used here, the Purcell and readout filters are slightly off resonance from each other due to fabrication defects, and so instead of being hybridized are separated into distinct high-Q resonator features and broad Purcell features. If we can see all of the pairs at approximately the expected frequencies, success! Nothing terrible has happened yet. Since resonator-Purcell pairs are coupled to flux-tunable qubits,

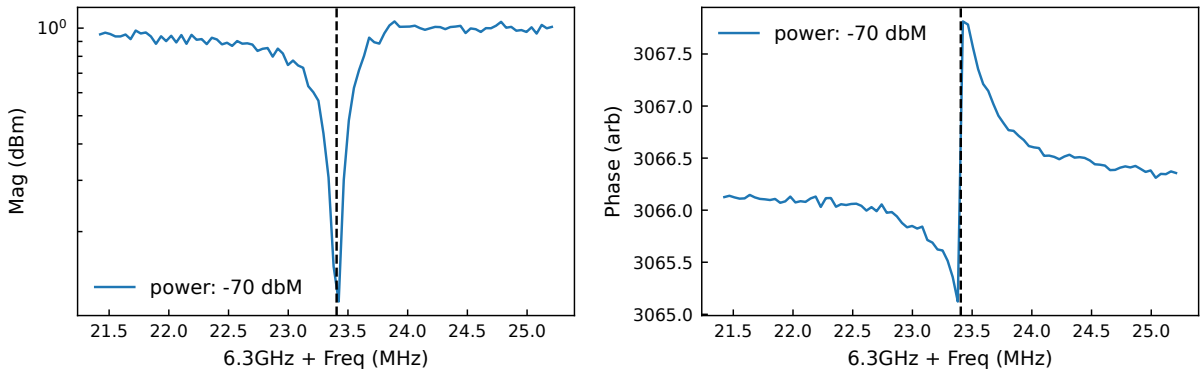

Figure 4.3: **Resonator Frequency Scan**

their dressed frequencies will depend on the qubit frequency – the resonator frequencies will move as the qubits are tuned. Because there is some random amount of flux frozen into the qubit SQUID loops during the cooldown, at zero external bias the qubits and thus the resonators will be randomly distributed somewhere within their frequency tuning range. You can calculate from expected qubit couplings and tuning range what the expected resonator frequency range should be, and see if what you measure is within that range.

Step 2: Check if the qubits are alive (the nonlinear Josephon junction is functioning) through resonator power sweeps. When the resonator is probed at low power, we see the dressed cavity-qubit mode frequency. When probed at higher power, the qubit nonlinearity is overwhelmed (see Ref. [78] for details) and the cavity snaps to its bare (i.e. uncoupled) frequency. Therefore, by varying the power of the resonator and seeing if the resonance frequency changes or not, we can check if there is a functional qubit coupled to the resonator. Check all the qubits! Power sweeps like this are also helpful to determine where the end of the low-power range for that resonator lies, as this is often the best place to probe without heating the qubit. Anywhere where the resonator shape starts to shift can be dangerous. The resonator shift gives an approximate measurement of the dispersive shift $\chi = g^2/\Delta$, with g the resonator-qubit coupling, and δ qubit-readout detuning [80]. To watch out for: if your material has kinetic inductance, at high enough power your resonator will start shifting

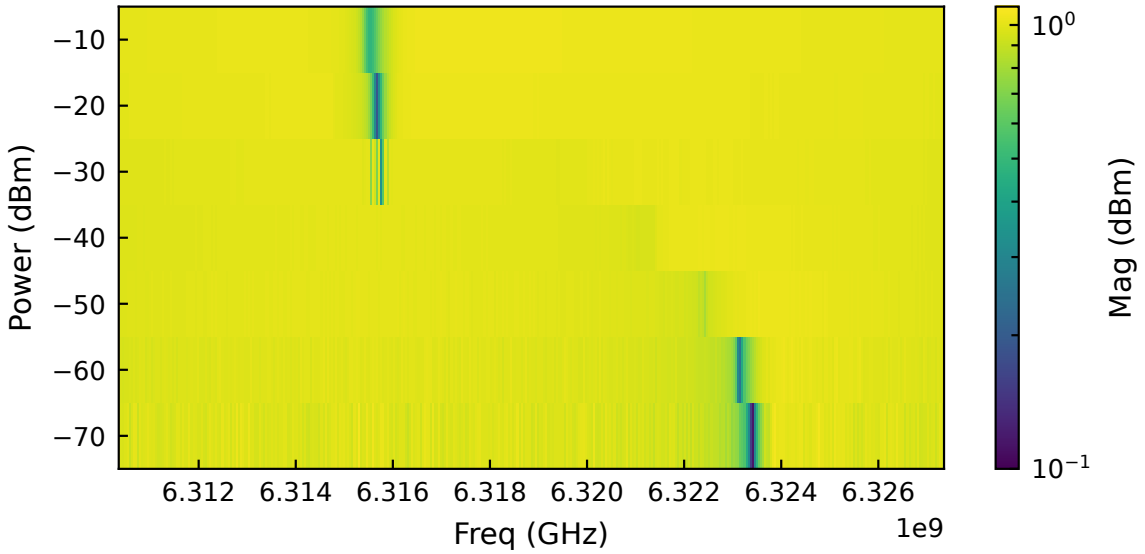

Figure 4.4: **Resonator Power Scan** At high drive powers, the resonator center frequency snaps to its bare frequency.

in frequency regardless if its attached to a qubit or not. Consider ahead of time if this might be an issue in your sample (often happens if metal layer very thin, $\ll$ 100nm). Also to watch out for: resonators are indirectly coupled to nearby qubits; even if the main qubit it is coupled to is dead, it may shift a small amount from the nearby qubits' nonlinearity. Check to see if the χ-shift (scale of the punchout) makes sense.

Debugging tip: strange resonator features. If your resonator appears to have multiple peaks spaced apart by expected χ shift, it may be that your qubit is hot and number-splitting the resonator [78]; your qubit is in a superposition of a few different states, so your resonator is in a superposition of a few different resonant frequencies.

4.3.2 Qubit Spectroscopy

Goal: Identify qubits in spectroscopy, get a general estimate of appropriate power and averaging necessary to see each qubit.

Step 1: Find the qubits! Now that the readout resonators are identified and we have

confirmed that each is attached to an alive qubit, it is time to try to actually find the qubit in frequency. To search for the qubits, we perform a two-tone measurement: one continuous tone is applied at the resonator center frequency, a second tone is swept around the expected qubit frequency, and we monitor the amplitude or phase of the return signal at the resonator center frequency. Because the qubit and resonator are coupled, when the qubit gets excited, the resonator peak frequency will shift, causing the signal at the original frequency to change in amplitude or phase (see Refs. [60, 61, 78] for an in-depth discussion of dispersive readout). Because the qubits are flux tunable, they could be anywhere in frequency! For each resonator-qubit pair, do a large sweep of the qubit tone at varying powers to try to find the qubit peak. In this sample, it is possible that the qubits might be in some confusing configuration: if two neighbors happen to be near to each other, they will hybridize and show up as two peaks in spectroscopy. If a qubit is too close or too far from the readout resonator, it will similarly be difficult to see. We know the qubits are alive from punch-out measurements. If it is not possible to find qubits where they are now we can do qubit frequency vs. flux scans and try again at a better flux point later. Write down necessary drive power and number of averages needed to get a good signal for the qubits you can see.

Step 2: For the qubits you do find, features to look for: at high probe powers, a second peak should appear, the $\omega_{02}/2$ transitions (if you drive at half the frequency of ω_{02}, you will excited a two-photon process where your qubit will oscillate between $|0\rangle$ and $|2\rangle$ without populating the $|1\rangle$ state). The distance between the ω_{01} and ω_{02} should be half the anharmonicity. If a third peak appears further out from the main peak by exactly the anharmonicity, that could be the ω_{12}; this is a sign the qubit is hot, and already has some population in the $|1\rangle$ state. If your qubit is split into several peaks separated by χ, this can mean there are several photons in your resonator that are number-splitting your qubit (i.e. you are driving the resonator such that there are multiple photons in it, or your resonator is hot).

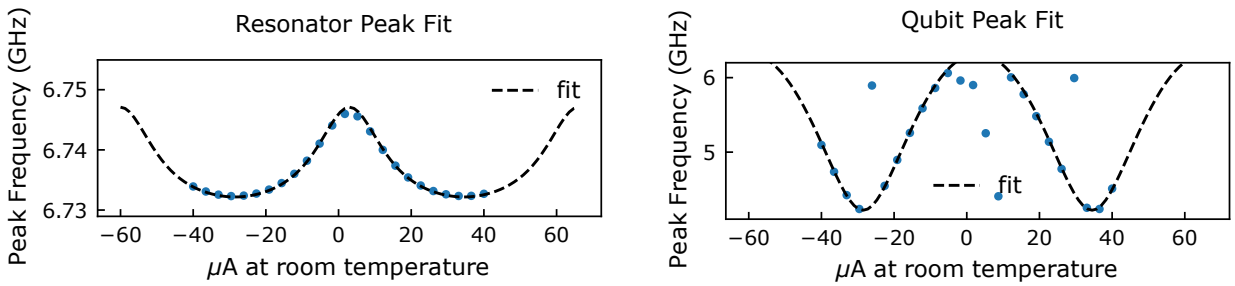

Figure 4.5: **Fitting Resonator and Qubit Peaks vs Solenoid Current to a Jaynes-Cummings model**

4.3.3 DC Flux Tuning

Goal: Check that qubits can be tuned in frequency. Fit tuning vs. flux curves for qubits and resonators. Use global solenoid magnet to bias the qubits as close as possible to desired static qubit configuration (detuned stagger configuration).

Remeber from Sec. 3.3 that the qubit frequency vs. applied magnetic flux through the SQUID loop is:

$$\omega(\Phi) = \sqrt{8E_J(\Phi)E_c} - E_c \text{ with}$$
$$E_J(\Phi) = (E_{J1} + E_{J2}) \times \cos(\pi\Phi/\Phi_0)\sqrt{1 + d^2\tan^2(\pi\Phi/\Phi_0)}$$

where E_{J1} and E_{J2} are the respective Josephson energies of the two junctions in the SQUID loop, Φ is the external magnetic flux through the loop, Φ_0 is the superconducting flux quantum, and $d = \frac{E_{J1}+E_{J2}}{E_{J1}-E_{J2}}$. Roughly, the qubit tuning is sinusoidal in magnetic flux.

Because the qubits and resonators are coupled, if the qubits tune in frequency, we should be able to see the resonators moving around too. Resonators are easier to see, so let's start by tracking them.

Step 1: We have a solenoid attached to our sample package that allows us to simultaneously put magnetic flux through all the qubits' SQUID loops (Sec. E). First, change the current through the solenoid (and thus the magnetic flux through the qubits' SQUID loops)

and measure how the resonators move in frequency. The shape should be periodic. Identify the current I_ϕ needed to tune each resonator by a full period in frequency for each qubit, which corresponds to putting one magnetic flux quantum through the SQUID loop. I_ϕ will be slightly different for each resonator, as the solenoid field is not spatially uniform across the on-chip area spanned by the qubits. Also mark the minimum and maximum resonator frequencies (this flux point corresponds to the qubit max. and min. frequencies, known as the "sweet spot" since at the max./min. points the first derivative of the frequency with respect to flux is zero, so to first order the qubits are not sensitive to flux noise and have high coherence times). To watch out for: the qubit will tune over a much greater range than the resonator (the resonator only tunes because it is weakly hybridized with a qubit), so as the magnetic flux is swept the relative qubit-resonator detuning changes – you may have to adjust power accordingly. If none of the resonators move, either all the qubits have a broken SQUID loop, or something is wrong with the global magnet. If some of the resonators move and some do not, the ones that do not move probably have broken SQUID loops.

Step 2: Tune the resonators in frequency with the individual qubit flux lines. Here, we pass magnetic flux through each qubit's SQUID loop by applying DC current through each qubit's dedicated on-chip line (Sec. 3.3). We use a DC voltage source with a large resistor in front to source the current(Sec. E). For each flux line, track the resonator as a function of voltage applied at room temperature, and measure V_Φ, the voltage necessary to tune a full period/apply a magnetic flux quantum through the SQUID loop.

Step 3: Repeat the above two steps, but with two-tone measurements, tracking the qubit frequency! These measurements take longer, but from the steps done so far you should already know what current tuning range is reasonable to see a full period, the appropriate power and average number settings for each resonator, and approximately the right power/averaging settings for each qubit from the initial two-tone characterization. Because as a qubit moves around it will sometimes hit neighbors in frequency, some flux points will

have to be thrown out. If you already know the approximate expected tuning range of your qubits from room temperature characterization of the E_J's of the SQUID loop (see Sec. D), from the resonator sweeps you can usually make a pretty good guess as to where the qubit will be at a given tuning current, and thus search for the qubit peak over a narrower range of frequencies (faster experiment!).

Step 4: Fit the resonator and qubit frequency vs. applied current data using analytic expressions from the Jaynes-Cummmings Hamiltonian + flux tunable qubit energy spectrum; once we measure and correct for crosstalk between flux tuning lines, these flux vs. frequency curves will allow us to determine what flux to apply to place the qubits in any desired frequency configuration. The fitting process enables us to extract estimated resonator-qubit coupling g, E_{J1} and E_{J2}, V_Φ, and ϕ offset flux.

Fit parameters: bare qubit ω_{max} and ω_{min}, bare resonator resonance ω_{res}, qubit-resonator coupling g, qubit anharmonicity E_c, voltage to tune a full period V_Φ, flux offset ϕ in units of voltage $\phi_V = \phi \times V_\Phi/\Phi_0$ (because voltage is proportional to current, and current is proportional to magnetic flux though the SQUID loop, we can relate flux to voltage using the constant V_Φ/Φ_0).

Fit steps:

- From fit input parameters, calculate $E_J^{max} = (\omega_{max}+E_c)^2/8E_c$ and $d = (\omega_{min}/\omega_{max})^2$.
- Calculate the bare qubit eigenenergies as a function of flux. In our current analysis code, we diagonalize the transmon Hamiltonian in the charge basis. The reader could also just solve for the qubit ω_{01} transition as a function of flux.
- Calculate the dressed $\omega_{01}(V)$ energies for the resonator and qubit – this is what we are fitting to the data. Our code calculates these dressed frequencies by numerically diagonalizing the Jaynes-Cummings Hamiltonian:

$$H_{JC}(V) = \omega_r a_r^\dagger a_r + \omega_q(V) a_q^\dagger a_q + g(a_r^\dagger + a_r)(a_q^\dagger + a_q)$$

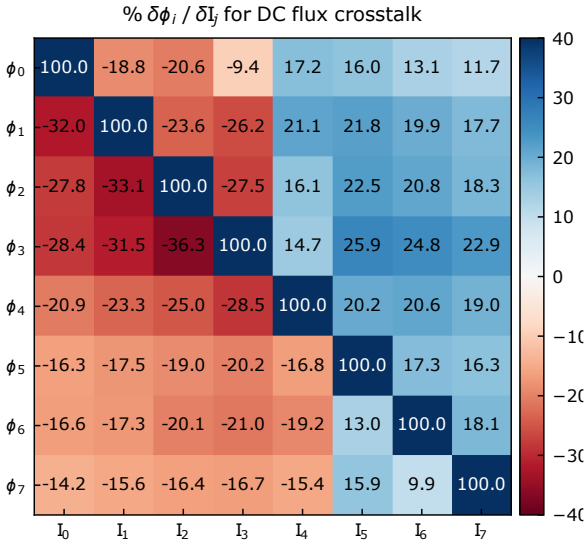

Figure 4.6: **DC Crosstalk Matrix**

Interpolate the fit to generate $\omega(V)$ (and $\omega(\Phi)$ since $V = \Phi \times V_\Phi/\Phi_0$).

Step 5: Passing constant DC current through the global magnet to set the constant frequency bias of the qubits does not heat the fridge as current is carried on a superconducting NbTi wire. Sending constant DC current through the individual flux lines can heat the fridge (we suspect the bias-tees, which have a large non-superconducting solenoid Sec. E). To minimize the amount of DC tuning from the flux line needed to hit the desired static qubit configuration, interpolate the flux vs. frequency curves for the global magnet, and determine what magnet current you need to get all the qubits as close as possible to the desired static qubit configuration. Go to that point, and confirm qubit locations.

4.3.4 DC Flux Crosstalk Matrix

Goal: Measure crosstalk matrix between flux lines and qubits, invert it to cancel crosstalk.

In an ideal world, each flux line would only be coupled to its respective qubit. Tragically, there is often some cross coupling between a flux line and other nearby qubits, where run-

ning current through a flux line applies magnetic flux through both its intended loop and neighboring loops. Since we can take mutual inductance relations here to be linear, if we want to cancel the crosstalk, there should be a linear matrix that tells us what currents we should apply to each line. We now proceed to measure the matrix!

For a single qubit i, the relation between flux and applied current is $\Phi_i = M_{ii} I_i$, where Φ_i is the flux, M_{ii} is the mutual inductance between the current line and the qubit SQUID loop, and I_i is the current applied. Crosstalk is captured by terms like $\Phi_i = M_{ij} I_j$, when current on the j flux line puts flux into qubit i's SQUID loop. To enact a particular Φ vector, i.e. desired quantity of flux in each loop, we invert the matrix to calculate how much current to apply on each line, $\overrightarrow{I} = M^{-1}\overrightarrow{\Phi}$. While we cannot directly measure the flux ϕ through a qubit's SQUID loop, we can measure the qubit's frequency $\omega(\Phi)$ as a function of applied voltage at room temperature (which is proportional to applied current at the sample). In section 4.3.3, we measured $\omega(V)$. From measuring the period, we know the voltage it takes to tune a full period, i.e. Φ_0/V_Φ.

We also cannot directly measure crosstalk elements, but we can measure $\delta\omega_i/\delta V_j$ by measuring local frequency response of a qubit to small changes in another qubit's flux at a fixed point in frequency ω_a. So,

$$M_{ij} = \Phi_i/V_j = \frac{\delta\Phi_i}{\delta\omega_i}\bigg|_{\omega_a} \frac{\delta\omega_i}{\delta V_j}\bigg|_{\omega_a} = \frac{\Phi_0}{V_\Phi}\frac{\delta V_i}{\delta\omega_i}\bigg|_{\omega_a} \frac{\delta\omega_i}{\delta V_j}\bigg|_{\omega_a} \tag{4.1}$$

We can choose whatever ω_a we want for this calculation; when measuring slope, it is easiest to do it in linear part of the $\omega(V)$ curve, and find a point where there are no other qubits/avoided crossings nearby.

To then place qubits at a particular frequency vector, we first convert that frequency vector to a flux vector $\overrightarrow{\phi}(\overrightarrow{\omega})$ and then apply the crosstalk matrix $\overrightarrow{V} = M^{-1}\overrightarrow{\phi}$.

Calculating DC crosstalk in this way is limited by how well we measure $\omega(V)$ relations and the matrix. To correct for errors, assume all errors can be mapped to phase offsets to

the $\Phi(\omega)$ relations. The correction procedure is as follows:

- Define ω_{intended} as intended frequency, and ω_{measured} as measured frequency after applying the flux tuning functions and DC crosstalk matrix.
- We previously determined $\omega(\Phi)$, which can be inverted to get $\Phi(\omega)$. Define $\Delta\Phi = \Phi(\omega_{\text{intended}}) - \Phi(\omega_{\text{measured}})$.
- Calculate $\Phi(\omega)_{\text{corrected}} = \Phi(\omega) + \Delta\Phi$, and use this as relation going forward.
- With new $\Phi(\omega)_{\text{corrected}}$ and crosstalk matrix, calculate new $\overrightarrow{V}$

We were usually able to place qubits within $10-50$ MHz on a first try, and within 100s of kHz after $1-2$ rounds of correction. A more precise way to correct the matrix and relations can be accomplished by using machine learning, see for example Ref. [83].

4.3.5 Resonator and Purcell Filter Parameters

Goal: After placing the qubits in the desired static frequency-detuned stagger configuration, extract Purcell-resonator linewidths.

Take a high resolution scan of each resonator and Purcell filter pair now that we know qubits are far detuned, and fit to linewdiths, resonator-Purcell coupling & detuning. See Refs. [79, 84] for fit function details.

4.4 Time-domain Measurement - Technical Points

So far, we have discussed measurements that involve sending and receiving continuous microwave tones. In this section, we are interested in doing characterization that involves preparing the qubit in a specific state and observing its properties under time evolution. We thus want to use discrete time pulses (time domain measurements, vs spectroscopy measurements).

4.4.1 Pulsed Signal Generation

Let us start with a few quick experimental notes of things to keep in mind when generating time domain pulses. We want to control the frequencies of our pulses, their amplitude/power, their phases, and their envelope shapes. We would also like to be able to read out the amplitude and phase of pulses returning from interacting with our sample.

Ideally, we would just specify our waveform digitally in code as an array of voltage points, and play that on our signal generation device. AWGs (arbitrary waveform generators) come close to this: they accept uploaded arrays of voltage values, and can play them back at some sampling rate, interpolating between digital points; they are digital to analog converters (DACs). However, all AWGs have some finite sampling rate of points (for example, an AWG might have a rate of 1 Gigasample per second 1GS/s, a sampling rate of 1 GHz). With a finite sampling rate, we cannot generate any signals with frequency components greater than, at minimum, 1/(2×sampling rate); to consistently generate clean signal, 1/(4×sampling rate) is safer [85].

Exercise 4.1: With a 500MS/s AWG (i.e. an AWG that can output 500 million samples in one second), what is the highest frequency you can reliably generate? What happens to the amplitude and frequency of the resulting (interpolated analog) signal as you go above and below that limit? Sweep signal phase and note effects.

The AWGs used in our experiment have a sampling rate of 1GS/s (see Sec E), too slow to directly generate tones at the frequencies of our qubits ($3-6$GHz in this experiment) and resonators ($6-7$GHz in this experiment). To get around this issue, we use an IQ mixer to mix our AWG pulses with a constant high-frequency RF signal source which we call the "local oscillator", or LO. Thus, we can can have high-frequency pulses while maintaining control of the lower-frequency pulse envelope and phase with the AWG. See Refs. [78, 80] for details on IQ mixing.

With mixers, there is always some leakage of LO signal through to the mixer output. We usually place our LO slightly detuned from the qubit transition to avoid weakly driving qubits even when the AWG is off, and then up-convert with the AWG when we play pulses. We can also send several frequency components with the AWG simultaneously to drive multiple qubits at once. The problem with up-converting is that the IQ mixer always generates sidebands at higher multiples of the upconversion frequency (lower in power than the main signal, but still present). So, when choosing the frequency of the LO, we aim to choose a frequency where we can drive all the qubits within the bandwidth of the AWG, and also choose qubit frequency placements relative to the LO such that sidebands are as far detuned as possible from all potential transitions.

4.4.2 Downconversion for Readout

To read out the signal returning from the sample, ideally we would be able to convert the analog waveform to digital for computer processing (using analog to digital converter, ADC, or digitizer) with infinite sampling rate. Once again, the real world falls short; digitizers also have finite sampling rates! Fortunately, we can do the inverse of the up-conversion process; we can use mixers, the return signal, and another RF generator to downconvert the signal frequency to something the digitizer can sample appropriately. If we use the same RF generator to downconvert as was used to produce the signal, we call it "homodyne" detection, using a different RF generator is known as "heterodyne" detection. In homodyne detection, the signal is mixed down to DC (a higher frequency image is also generated that can be filtered out), and amplitude and phase get mapped to the mixer I and Q channels as $\sqrt{I^2 + Q^2}$ for magnitude and $\tan^{-1}(I/Q)$ for phase. In heterodyne detection, the signal is mixed down to the difference between the incoming tone and the reference tone.

4.4.3 Pulse Shaping

To understand the effect of a time-domain pulse envelope, it is often instructive to look at its Fourier transform, or frequency components. For example, we often want our pulses to be as fast as possible (resulting in more physics before our particles decay). At first glance, it is tempting to try to drive with the maximum possible power to quickly excite a qubit or resonator: make a tall, very short square pulse. Looking in the frequency domain, however, it becomes apparent that the shorter the pulse, the larger its frequency spread. Square pulses, while providing the most amount of power over time compared to other shapes (Gaussian, etc), also have broad frequency components because of their sharp features. Such a square pulse works well if there are no other transitions nearby. However, for qubits, the ω_{12} transition is close enough that driving with a short pulse can cause leakage to the $|2\rangle$ state. One can solve this with specific pulse shaping (like DRAG pulses) if there is just one transition to avoid. In our case where we have one drive line for all the qubits, we rely on frequency separation to not drive qubits we do not want to drive. Thus, we use Gaussian pulse shapes and take care that the frequency bandwidth of our pulses is less than the inter-qubit spacing. The frequency domain version of a Gaussian pulse is also a Gaussian pulse, with the sigmas given by: $\sigma_t \sigma_f = 1/(2\pi)$.

Sanity check: If possible, always check your generated pulses in an oscilloscope both in the time and frequency domain! A lot of errors can be caught this way. Similarly, a wise tip from David Schuster: running the generated pulses directly to the ADC can be very helpful for looking at shot-by-shot results and catching obtuse timing and triggering errors.

4.4.4 Lattice Configuration Revisited

As mentioned in Sec. 4.2, our static qubit configuration had nearest neighbors staggered by $400 - 500$ MHz. Since our AWG has a 1GS/s sampling rate, we cannot use just one LO and AWG combo to hit all the qubits (with 1GS/s, we can upconvert or downconvert

the LO frequency by *at most* ± 500MHz). Instead, we use two pulse generation setups, one for the upper branch of qubits and one for the lower. We use the same LO frequency for each qubit within a branch – the sidebands that the AWG has to generate are defined by $f_{AWG} = f_{qb} - f_{LO}$. To choose the ideal LO position, we run an optimizer to see which sidebands are the safest/would not hit unwanted transitions if they were not properly suppressed by the IQ mixer.

4.5 Qubit Control and Characterization

4.5.1 Readout Revisited

Goal: Make sure resonator is still visible when using pulsed setup, choose a starting pulse length.

Though we have already done readout and qubit spectroscopy using the network analyzer, the first thing to do upon switching to the pulsed measurement setup is to repeat these experiments! This is a helpful sanity check to make sure all measurement components are working well now that we have switched setups, and is good for calibrating powers and averaging time.

The resonator measurement is much the same as when measuring using the network analyzer – sweep readout tone in frequency and fit the result to a Lorentzian to find the peak, sweep in power to find the low vs. high power limit using the pulsed setup. If you know the output power of your pulsed setup, you should be able to predict when then low vs. high power limit occurs from the network analyzer data. The data from the digitizer will be in the form of I and Q values (see Refs. [78, 80] for details); take $\sqrt{I^2 + Q^2}$ for magnitude and $\tan^{-1}(I/Q)$ for phase.

Since our readout pulse is now finite in time, we also have to think about how long to make the readout pulse. This pulse time is chosen by taking into account several different

factors. Our goal is to check if the resonator has been shifted by the qubit being in the $|e\rangle$ state or not with high fidelity. Running the pulse for longer gives us more signal to average over for a particular shot. With a quantum-limited amplifier, averaging time for high fidelity readout is often in the 100s of ns; with just amplifiers at the 4K fridge stage the amount of signal averaged for a shot is closer to $1\mu s$. (This is the case in our experiment, and why we do not worry about arbitrary control over readout waveform shape – the pulse is narrowband enough that we do not worry about hitting other transitions). Why not just drive the pulse for an arbitrarily long amount of time to get good single-shot averaging? The problem is the qubit lifetime: the longer one reads out, the exponentially more likely it is that the qubit will relax back to the ground state – running the readout pulse for longer only gets you so far.

After choosing a starting pulse length, see how many averages are needed to get a low-noise readout peak – this will tell you approximately how much you need to average for all the rest of the experiments, because all of our qubit measurements are based on resonator $|g\rangle - |e\rangle$ voltage contrast. You can try different readout pulse lengths to see how that affects the noise in your readout signal, though we will also be doing a more quantitative calibration later in Sec. 4.6.

4.5.2 Qubit Pulse Probe Spectroscopy

Goal: Make sure qubit is still visible when using pulsed setup. Measure un-Stark-shifted frequency.

Now time for qubit spectroscopy! The principle is the same as for using the network analyzer, with a few extra factors to take into consideration given finite-time pulses.

For example: when doing two tone using the network analyzer, the resonator tone and the qubit tone are both on at the same time. This is not how we want to operate when preparing specific qubit states: the resonator tone dephases the qubit, and can only be applied at the

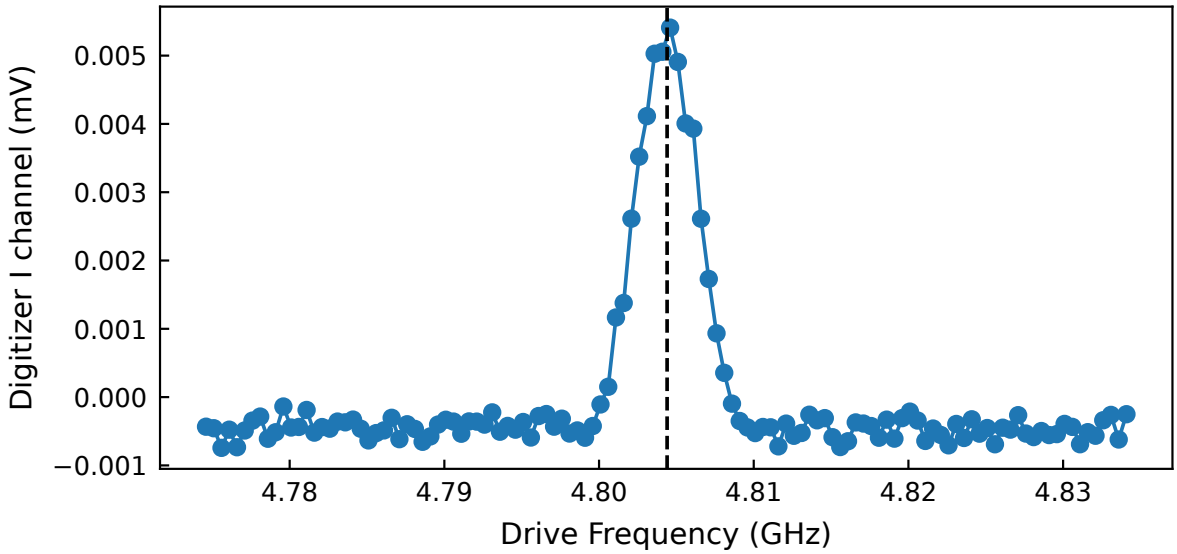

Figure 4.7: **Qubit Spectroscopy with Pulsed Measurement** Qubit peak center is marked with dashed line.

end of an experiment for readout. With both drives on at the same time, photons in the resonator can also number-split the qubit, and the resonator drive can AC Stark shift the qubit frequency. To that end, in pulsed spectroscopy we apply the qubit pulse first, then the readout pulse (hence, pulse then probe name of the measurement).

We probe the qubit with a long (narrow in frequency) low-power pulse, and hope to see a Lorentzian peak to which we can calculate a fit. A peak will show up in I and in Q. At a given readout power and frequency, you can digitally rotate the quadratures into each other to get all the signal in one quadrature going forward.

Things that can go wrong, and how to debug:

Seeing several peaks When a qubit is driven on resonance, its state flops between $|0\rangle$ and $|1\rangle$ until it dephases and settles at an average population of 0.5. If it is driven partially off resonance, it will also flop, at faster frequency and without ever fully reaching the $|1\rangle$ state. So, if you drive for shorter than the dephasing time and scan frequency, you can end up with some very strange looking spectroscopy! If you see strange features and are confused,

it can be helpful to do a Rabi chevron experiment, where you scan over both frequency and pulse length to understand what is going on. This is why we start by driving at low power and for long times, to attempt to only get one feature. You can also go directly to Rabi chevron, but these scans take a bit longer since you are doing a 2D sweep.

Seeing several peaks even when driving longer than the dephasing time There are several possibilities here, a few of which could be:

(1) The resonator is hot/has several photons in it, you are seing your qubit being number-split by the resonator (the same way the resonator has a different center frequency depending on the state of the qubit, the qubit's frequency also depends on the number of photons in the resonator).

(2) You are coupled to some mystery transition, often termed "TLS" or "two-level system." These lossy elements can be dangling bonds, flux vortices, or any number of other lossy defects. Most often they just kill a qubit's lifetime at a given point in frequency, but if the coupling is strong they can also split the qubit peak. If this happens, try tuning that particular qubit to another point in flux and try again.

(3) The mystery peak might be another qubit. Ideally, you have placed the qubits in a staggered configuration as specified in Sec. 4.2 so that no neighbors are close to each other, but maybe you made a mistake! If you see a peak at a frequency that does make sense for another qubit to be at ($\sim$ 50 MHz away from the qubit you are characterizing), that just means that the readout resonator of the qubit you are characterizing is also sensitive to that other qubit's state (which should not happen but sometimes does, see Sec. 4.6.3).

What determines width of peak When driving the qubit with a finite pulse, several factors will determine the width of the peak: the qubit's inherent dephasing time, the frequency components of the drive pulse (a pulse broad in frequency will create a broad peak response), and drive strength (power-broadening). If your peak is real, it can be interesting to drive with a very long pulse (i.e. narrowband) with lower and lower powers to see the

qubit shrink to its natural linewidth as the peak fades into the noise background.

Don't see anything, even though within $\sim$ 50MHz of value predicted from network analyzer Sanity checks:

- Do the raw IQ values make sense given what you would expect from resonator spectroscopy (does the background of the qubit scan match the resonator voltage expected from the unshifted resonator peak?)?
- Overlap the qubit and the readout pulse, in case the issue is that the qubit lifetime is so bad it is decaying before you can average enough on the readout.
- Check if the frequency spacing you are scanning over is dense enough; if the qubit peak is 1 MHz and you are only taking points every 2 MHz, you might just be missing the qubit peak.

If you are feeling ambitious, you can redo the qubit frequency vs. flux fitting and DC crosstalk matrix using pulsed spectroscopy. It will be more accurate, since there are no Stark shifts! We usually measure tuning features with the network analyzer first rather than pulsed measurements since to ensure nice peaks the qubit pulses need to be longer than the dephasing time, and without knowing exactly the transmon frequency vs. flux curves one needs to scan over on the order of 100MHz in frequency; the Keysight PXI system we use does not have the memory to do an appropriately frequency resolved scan of that bandwidth with long pulses in one run.

4.5.3 Rabi and Pi-Pulse Calibration

Goal: Calibrate qubit π-pulse

Having verified where the qubit is in frequency, we now want to calibrate a π-pulse that will bring the qubit from $|0\rangle$ to $|1\rangle$. The Rabi pulse sequence is as follows: pulse the qubit on resonance while varying pulse time or pulse power, and fit the resulting decaying sine wave.

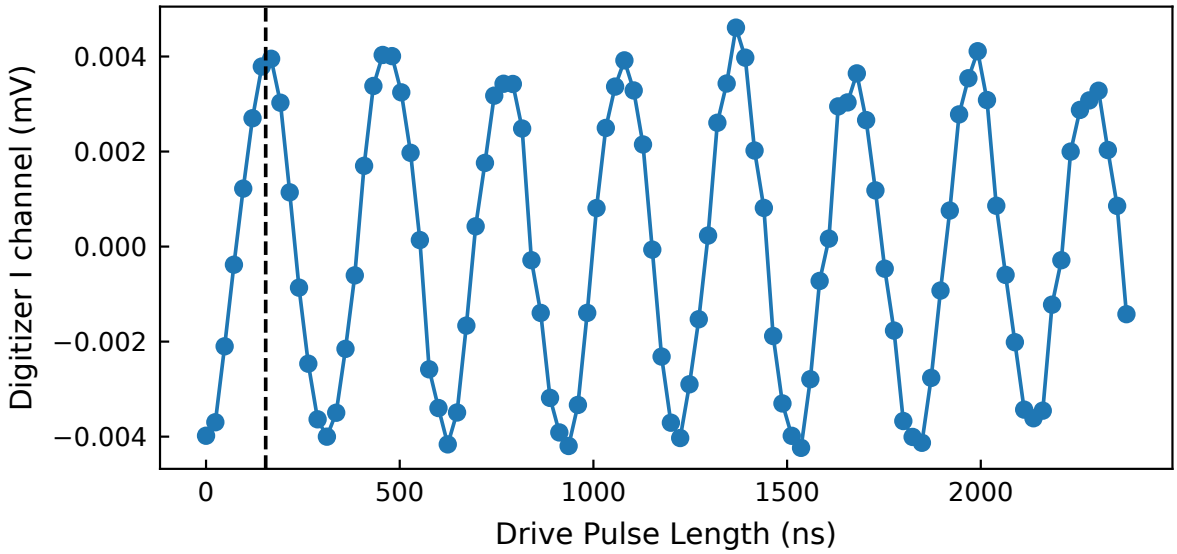

Figure 4.8: **Qubit Rabi** π time marked with vertical dashed line

The π-pulse time/power can be extracted from that sine fit! Sweeping in time first is usually easier to get the expected oscillation (more range to make longer pulses than to vary pulse power in our experiment setup), but varying pulse power while keeping time fixed ensures your pulse always has the same bandwidth.

To avoid hitting nearby qubits in frequency, we usually use Gaussian pulses and adjust power until our π-pulses can be done with $\sigma \sim 30$ns for a pulse with a 4σ cutoff). We usually take our $\pi/2$-pulse to be half the power of our π-pulse (we do not want to take it as half the time for fear of changing the bandwdith). To more carefully calibrate these pulses, one can use randomized benchmarking [60].

4.5.4 T1

Goal: Measure qubit lifetime.

The next step on our pulse journey is to measure the qubit lifetime. For each qubit, we π-pulse it, wait a variable time t, and then perform readout. Then, we fit the corresponding

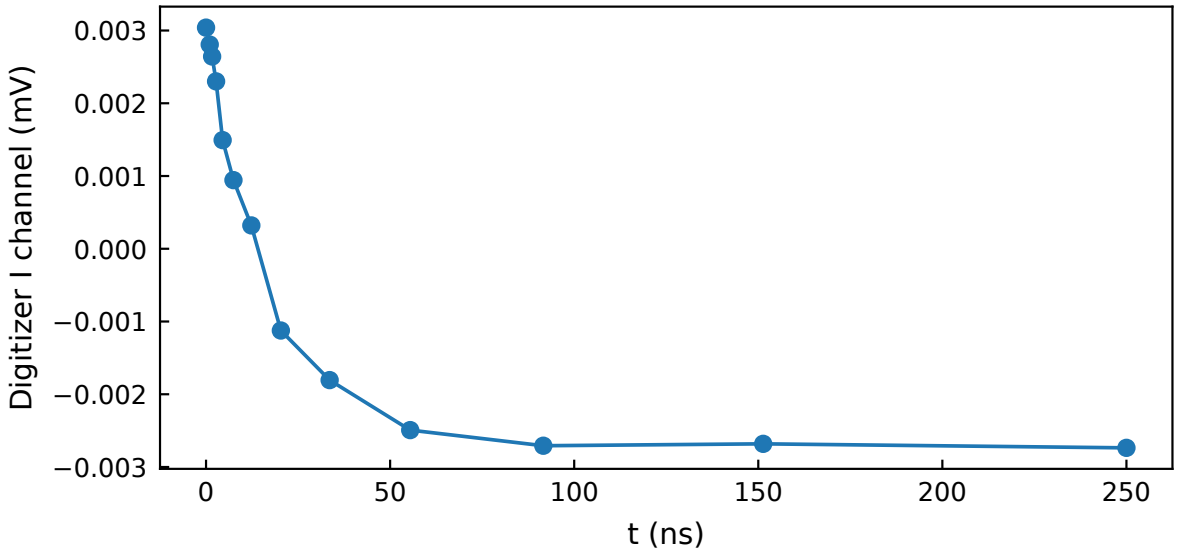

Figure 4.9: **Qubit T1**

exponential decay curve to extract the qubit lifetime T_1.

If you see multiple decay rates, maybe you have partially excited the qubit's higher states and are seeing them decay too.

We found our qubits' lifetimes changed both over the course of minutes for some qubits, and more drastically over the course of days for all qubits. We usually ran a T_1 calibration scan on repeat for $5-10$ minutes to measure average and variation. Moving to alternate qubit configurations sometimes helped get away from especially low lifetime or high fluctuation spots.

4.5.5 T2 Ramsey

Goal: Measure qubit dephasing time.

Next, we perform a Ramsey measurement to quantify both the qubit's dephasing time and to measure its frequency more precisely.

In this pulse sequence, we first perform a $\pi/2$-pulse, wait a variable amount of time t,

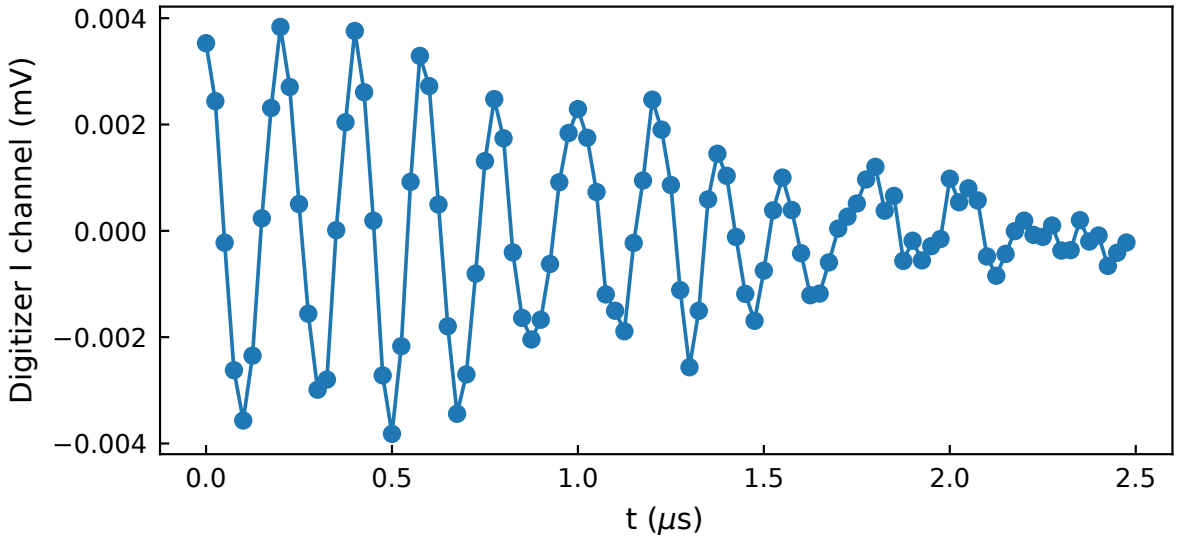

Figure 4.10: **Qubit Ramsey measurement**

and then apply a second $\pi/2$-pulse. Since our drive tone is rotating at the qubit frequency, the drive tracks the qubit's rotation; without any dephasing, both pulses are performed with the same phase relative to the qubit phase. If the qubit does have some frequency jitter/dephasing, it will correspondingly have some frequency jitter with respect to the drive, and the second pulse will no longer be applied with the right phase; on average, this causes an exponential decay in the signal. The decay is both from pure dephsaing and from particle loss, with the exponent given as:

$$\frac{1}{T_2^*} = \frac{1}{2T_1} + \frac{1}{T_\phi} \tag{4.2}$$

.

Consider that if we detune our drive on purpose (or add a time-dependent phase shift to the second $\pi/2$-pulse), the second pulse will be applied in a rotating phase along the Bloch sphere, with the corresponding trace oscillating at the difference δ between the qubit frequency and the drive. This is useful for precise measurements of the qubit frequency: adding in a virtual drive offset means you can have your oscillations be for example at

5MHz$\pm\delta$ (with a time trace of 1μs you already have 5 periods) rather than just at δ which might be in kHz and difficult to measure without waiting very long time ranges t.

Flux-tunable qubit coherence is generally limited by noise coming through the flux line, which directly jitters the qubit around. To measure the noise in flux quanta, normalize by the frequency vs. flux slope at your current qubit's parked location.

4.5.6 Echo

Goal: Measure dephasing noise spectrum.

To learn more about the noise spectrum of the qubit dephasing noise, one can apply one (or several) refocusing π-pulses before the second $\pi/2$-pulse. Consider: if my qubit had drifted slightly off resonance, it would accumulate some phase difference from the drive in the first sequence, but after being reflected by a π-pulse would refocus completely. By varying the number and frequency of refocusing π pulses one can learn about the noise spectrum.

4.5.7 Characterizing Qubit ef Transition

Goal: Calibrate ef transition controls.

Finally, we can repeat all these experiments (resonator optimization, qubit transition spectroscopy, π and $\pi/2$ calibration, T_1 and T_2^* measurement) with the qubit $|1\rangle$ to $|2\rangle$, or ef transition! We usually start all these calibrations by first π-pulsing the qubit to get it into the $|1\rangle$ state, and then proceed as detailed above.

A few things to be wary of: we are trying to cover both a qubits' ge *and* ef transition with the same AWG, but the frequency difference of these two transitions is close to 250MHz, at the limit of what we can do with our AWG sampling rate, especially if the ge transition is already detuned from the LO by up to 200MHz to try to hit all qubits in a given branch! Sometimes we used our two setups, one to do the ge pulse and one to do the ef pulse; sometimes we set a special AWG point just to characterize ef; do as you will.

The other thing to be careful of: readout is currently parked at the peak of the resonator position when qubit is in $|0\rangle$. Depending on the resonator shift, it might be difficult to distinguish resonator shift from the qubit being in the $|1\rangle$ vs $|2\rangle$ state. One option is to choose a resonator frequency to instead be centered on the resonator position when it is in the $|1\rangle$ state.

4.6 Readout Optimization

4.6.1 Binning and Confusion Matrix

Goal: Bin readout shots into 0 or 1, calibrate and apply a confusion matrix to correct for binning errors.

Speaking of readout, let's revisit our good friend the resonator!

Up until now, in each experiment shot we have been taking the average downmixed DC voltage of the return readout pulse, and then taking many shots to average out noise and obtain good measurement statistics. With this method, we cannot tell exactly what the distribution of $|0\rangle$ and $|1\rangle$ states are for a given averaged measurement. We can do better! We can bin each shot as either $|0\rangle$ or $|1\rangle$, and then average over the binned shots instead.

For each shot, we average the readout voltage for $1-5\mu$s, and then based on the averaged voltage value bin that shot as either the transmon $|0\rangle$, $|1\rangle$, or $|2\rangle$ state. We choose two different readout frequencies, ω_{read01} and ω_{read12}. At ω_{read01} the distinguishability of $|0\rangle$ from $|1\rangle/|2\rangle$ is maximized, while the distinguishability of $|1\rangle/|2\rangle$ is minimized. Similarly, at ω_{read12} the distinguishability of $|2\rangle$ from $|0\rangle/|1\rangle$ is maximized, while the distinguishability of $|0\rangle/|1\rangle$ is minimized. With these optimized readout points, we measure a single shot fidelity for binning $|0\rangle$ and $|1\rangle$ at ω_{read01} of $85\% - 95\%$.

With $85\% - 95\%$ fidelity, binning errors are non-negligible. To correct for this, we use a confusion matrix measured at the end of each experiment. To measure the confusion matrix,

we apply a readout pulse (qubit should be in $|0\rangle$) and measure $|0\rangle$ and $|1\rangle$ counts. Then, we apply a π-pulse (qubit should be in $|1\rangle$) and measure the number of $|0\rangle$ counts and $|1\rangle$ counts. From these measurements, we can construct a 2×2 confusion matrix. Inverting this matrix and applying it to our data corrects for binning errors. It also corrects for both average rates of population loss and thermal excitations during readout. For simultaneous two-qubit measurements, we measure and calibrate using a two-qubit (4×4) confusion matrix.

4.6.2 Readout Histogram

Goal: Calibrate binning procedure, optimize readout fidelity.

To calibrate state binning, we perform a histogram experiment: we do a large number of shots of preparing the qubit in the $|0\rangle$ and $|1\rangle$ states, and check the corresponding voltage distributions. From here, we fit two Gaussians (we use a machine learning algorithm to figure out what the underlying two Gaussians are for the entire distribution). To bin, we draw a line between the center of the Gaussian distributions corresponding to each state; to the right of the line the qubit state is binned as 1, to the left it is binned at 0. Singleshot fidelity (with how much confidence can you determine the qubit state in a single shot) is calculated by the overlap of the two Gaussians.

Histograms are a fast experiment, and a nice way to optimize readout fidelity: one can sweep readout power, frequency, and pulse length and measure the corresponding fidelity for each quit. This is a useful debugging tool: it can track heating (when you prepare g, do you have some Gaussian component in e in addition to usual Gaussian overlap?) and decay (the opposite process).

4.6.3 Readout Crosstalk

Goal: Measure and correct crosstalk between readout resonators.

Readout crosstalk occurs when a readout resonator is sensitive to a qubit other than the

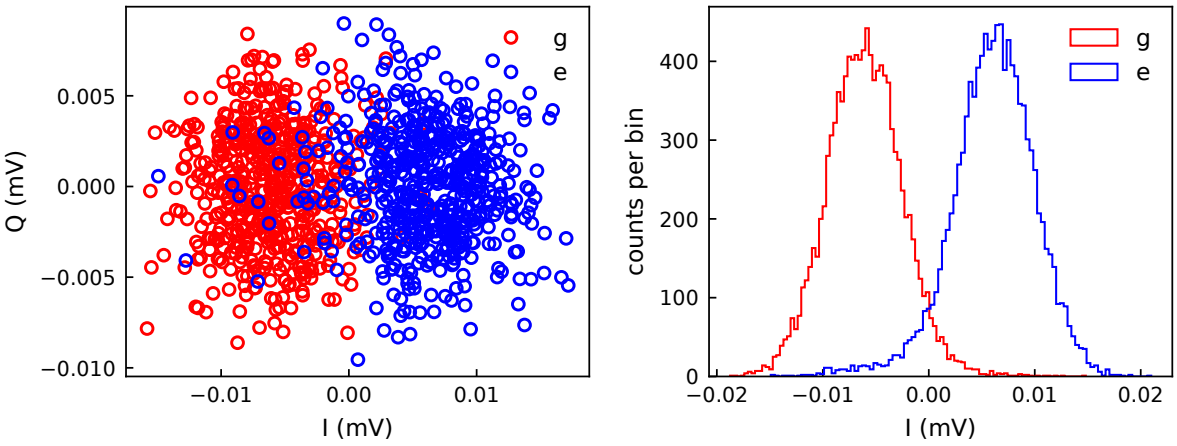

Figure 4.11: **Qubit Histogram**

one to which it is directly coupled to, causing binning errors depending on the population of that other qubit. The source of this type of crosstalk in our system is not completely apparent to us. We measure that the crosstalk is worse the closer the qubits are together in frequency, but even with the qubits at the large disordered stagger we were unable to find a frequency configuration without at least some readout crosstalk. At the large disordered stagger used for experiments, we measure negligible crosstalk between all elements except for between Q1 and Q3 (see Fig. 4.12). We suspect this crosstalk is caused in part by a chip package mode coupling the resonators.

When first characterizing crosstalk, it is illustrative to do resonator spectroscopy scans as a function of which qubits are excited. For example, let us consider the case of two qubits A and B. We would do spectroscopy on A's resonator with:

- QA in $|g\rangle$ QB in $|g\rangle$
- QA in $|e\rangle$ QB in $|g\rangle$
- QA in $|g\rangle$ QB in $|e\rangle$
- QA in $|e\rangle$ and QB in $|e\rangle$

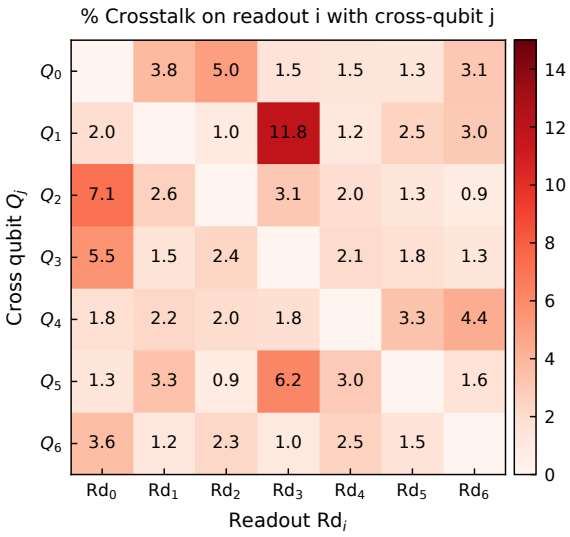

Figure 4.12: **Readout Crosstalk** Measure of how sensitive readout resonator Rd_i is to the state of qubit Q_j, normalized to the shift of resonator Rd_i in response to the state of qubit Q_i.

- QB in $|e\rangle$ and QA in $|e\rangle$ (sometimes the order mattered for the observed crosstalk!)

and see how A's resonator profile changes. This helps distinguish different between different possible readout issues. If the problem is qubit drive crosstalk, for example, driving qubit B will shift A's resonator peak between its normal g and e center frequncies. If qubit B has some parasitic coupling to resonator A, driving qubit B will shift resonator A between its $|g\rangle$ center frequency and a new center frequency determined by its χ shift to qubit B. In our device, we noticed a further asymmetry: sometimes, resonator A would not shift if qubit B was excited and A was in the ground state, but would shift to a new resonance frequency if qubit A *and* B were excited.

After determining the shape of the problem (in our device, we convinced ourselves that the problem was not qubit drive crosstalk, but some particle-number-dependent parasitic coupling between non-paired resonators and qubits), we tried to find resonator settings that minimized this crosstalk. We swept resonator power and the frequency, and measured qubit

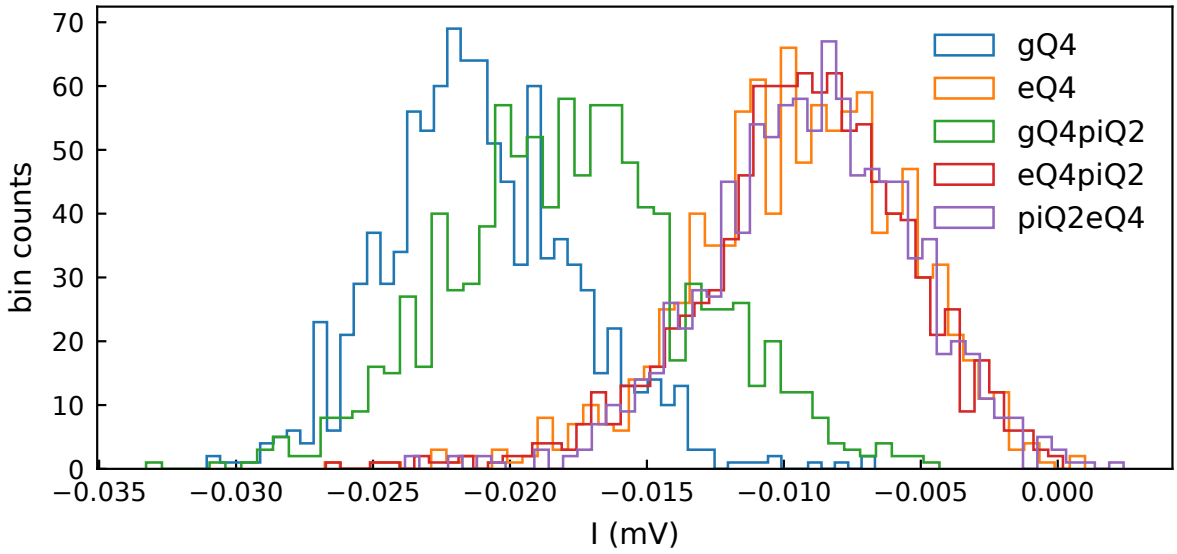

Figure 4.13: **Qubit Histogram: Readout Crosstalk** At a given readout power and frequency, measuring Q4's readout histogram as a function of the state of Q4 and another qubit (here Q2). See that when Q2 is in e, the resonator voltage shifts (even though Q4 is still in g).

histograms at each point for different combinations of qubit pulses, searching for the highest fidelity/lowest crosstalk point.

We found that our crosstalk was significantly worse between neighboring qubits if the lower qubit was anywhere near the upper qubit's $|f\rangle$ state.

4.7 Automated Program to Find Ideal Parameter Space

Goal: Check qubit parameters at a multitude of different frequency points to find ideal configuration.

Once all qubits are characterized at one frequency configuration, we sweep the whole qubit stagger around in frequency to test for nearby TLS or other low lifetime spots, and ensure the entire range in which we operate boasts relatively high qubit lifetime. To calibrate this, we have written automation code that steps through different frequency positions and

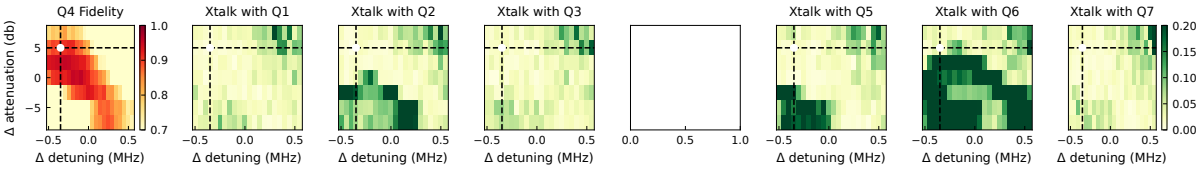

Figure 4.14: **Qubit Histogram Crosstalk Sweep** Example crosstalk sweep, here given for Q4. We sweep the readout frequency (x axis) and readout attenuation (i.e. power, on y-axis). For each column i, we run different combinations of pulse sequences with Q4 and Qi, plotting the maximum readout crosstalk at that power/frequency point. Percent crosstalk is calculated as, for example, if Q4 is in g, and Qi is pulsed, and then new average voltage gets binned as Q4 e 20% of the time, I call that 0.2% crosstalk. The far left plot is readout fidelity for Q4.

characterizes qubits at each frequency position, leading to plots such as in Fig. 4.15.

The logic sequence of the automation code is as follows: Run resonator spectroscopy, run pulse-probe spectroscopy to get new qubit frequency, run Rabi to get new qubit π-pulse, run $T1$, run $T2$, run histogram to get a rough measure of readout fidelity. Shift the entire qubit configuration by Δ step specified by user using DC flux biasing, and then repeat!

The code sequence has a few error conditions it looks out for, namely looking for random qubit frequency jumps or DC tuning not lining up with expected value (in which case it attempts to correct the DC voltage value), bad fits (looks for unphysical parameters and robustness of fit), consequences of extremely low qubit coherence (sometimes $T1$ can drop so low it is impossible to see the qubit in spectroscopy, or properly fit a π-pulse; assuming such areas are localized in frequency, the code then jumps to the next detuning step and tries again).

This type of scan was run passively on several long scans in experiments described in Chapters 5 and 6 to catch and correct for qubit drift in between experiments.

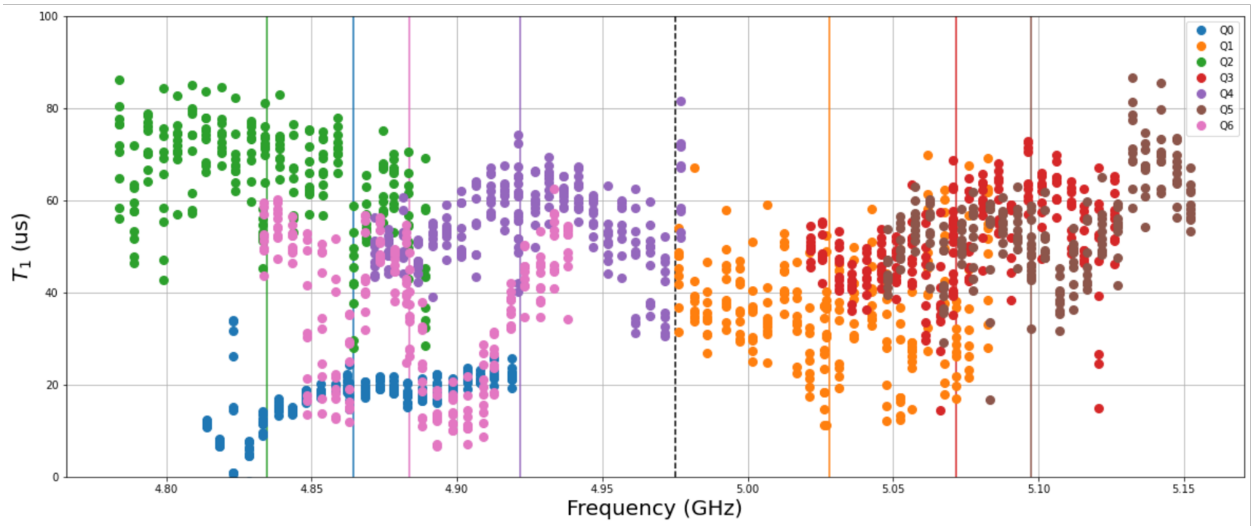

Figure 4.15: **T1 scan vs frequency**

4.8 Fast Qubit Frequency Tuning

Now let's add in flux tuning during an experiment! We do this with AWG voltage cards. Important note throughout: whenever we make a flux pulse during an experiment, we also do the opposite of that flux pulse at the end of the experiment after readout, to make sure that there is net zero flux (to avoid long-term transients such as an inductor or capacitor being charged up) [86].

4.8.1 RF Flux Crosstalk

Goal: Calculate crosstalk between qubit tuning lines at RF.

We calibrate the RF flux crosstalk the same way as for DC crosstalk, just using pulses instead of continuous RF and DC tones. We calculate $dV/d\phi$ first, then calculate the voltage crosstalk matrix $d\omega_i/dV_j$, and use both measurements to place qubits in frequency deterministically.

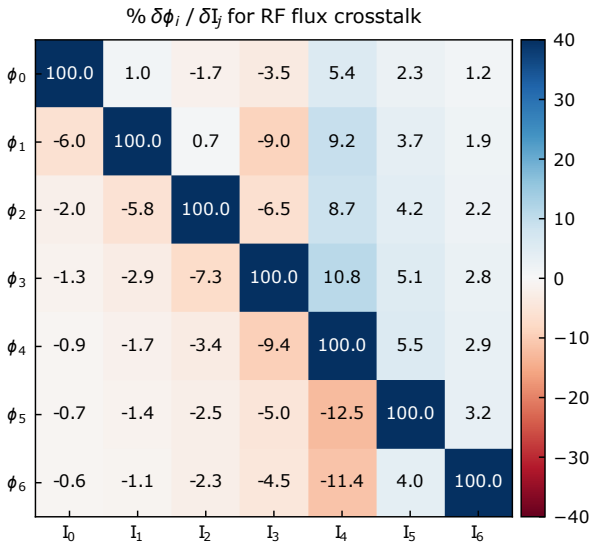

Figure 4.16: **RF crosstalk matrix**

4.8.2 RF Qubit Tuning Pulse Shape Distortion Correction

Goal: Correct for distortion in qubit tuning pulses.

We would like to control the qubit frequencies with great precision using RF flux. However, the flux signal is distorted by low-pass filtering on the RF line (in our case, AWG distortion is negligible). We use the same procedure as in [31] to measure the distortion using qubit spectroscopy and correct for it. An example of a flux step pulse pre- and post-correction is plotted in Fig. 4.17. For the corrected signal, the qubit frequency $\omega/2\pi$ settles to within $< 0.125\%$ (0.5 MHz for a 400 MHz jump, which is the largest jump in our experiments) in 400 ns. It is possible to do a better correction than this if one can readout and control the qubit near the sweet spot, see Ref. [87].

4.8.3 Landau-Zener Transitions

Goal: Calculate order of magnitude of unwanted transitions.

Whenever we diabatically jump qubits past each other, there can be unwanted population

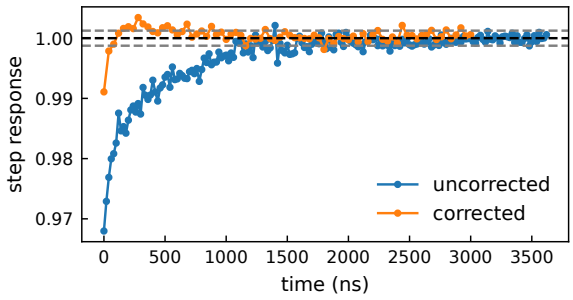

Figure 4.17: **Qubit Frequency Response to a Step Function in Flux With and Without Kernel Correction**

transfer from Landau-Zener (LZ) transitions when qubit levels cross each other. In this experiment, the level crossings of concern are ω_{01^Q} with $\omega_{01^{NN}}$, and ω_{01^Q} with $\omega_{12^{NN}}$ where NN is the nearest neighbor of qubit Q. We measure the ω_{01^Q} with $\omega_{12^{NN}}$ transition from the small disordered stagger to the large disordered stagger to be $<5\%$ for all qubits. Since the jump from degeneracy to the large disordered stagger is bigger and thus the qubits move past each other faster, we can assume that the LZ transition for that frequency jump will also $<5\%$ for all qubits. We calculate that the ω_{01^Q} $leftrightarrow$ $\omega_{01^{NN}}$ transition probability will also be $<5\%$ for all qubits.

4.9 Bose-Hubbard Parameters

4.9.1 Tunneling

Goal: Measure Bose-Hubbard tunneling J.

We π-pulse one qubit, and bring both it and its neighbor on resonance at the frequency which we use for Bose-Hubbard lattice physics. We then wait a variable amount of time, and snap both qubits back to their detuned configuration (stagger) and measure the frequency of particle exchange.

As a sanity check, one can also measure the avoided crossing between the two qubits in

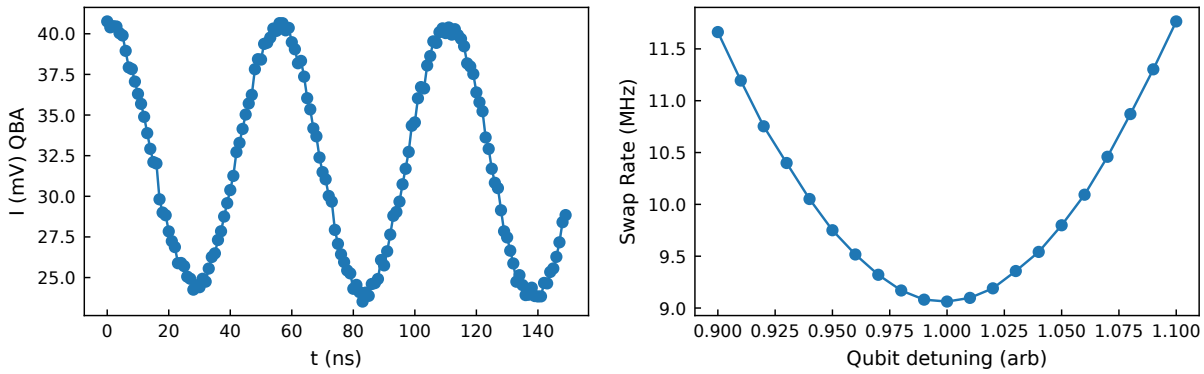

Figure 4.18: **Measuring Bose-Hubbard J** We measure the swap rate between neighboring qubits at different detuning to be sure to choose the correct (lowest) swap rate.

spectroscopy.

4.9.2 Anharmonicity

Goal: Measure Bose-Hubbard interaction strength U.

To measure the anharmonicity of a qubit, we first π-pulseit to the $|1\rangle$ state, use an RF tuning pulse to quickly bring the qubit to the lattice frequency, and then perform ef qubit spectroscopy (i.e. sweep the qubit drive frequency around the ω_{12} transition while monitoring the readout at a frequency that is sensitive to the readout position when the qubit is in $|1\rangle$ vs $|2\rangle$.

4.9.3 Multi-Qubit Preparation Fidelity in Detuned Configuration

Goal: Ensure high-fidelity state preparation at the detuned stagger configuration.

So far we have talked about single qubit calibrations. However, for our experiment we want many particles! How well can we add in several particles, and readout particle correlations?

To test how well we add in particles, π-pulse several different qubit collections, and then readout them out in the population basis. Were upi able to drive into the correct state?

Similarly, try to read out two qubits simultaneously – does having another readout drive on affect ideal readout frequency/power settings of the first readout drive? We found we did not have to adjust parameters when having two readout pulses on at the same time in the current device.

CHAPTER 5

DISORDER-ASSISTED ASSEMBLY OF STRONGLY CORRELATED FLUIDS OF LIGHT

Guiding many-body systems to desired states is a central challenge of modern quantum science, with applications from quantum computation [10, 11] to many-body physics [38] and quantum-enhanced metrology [88]. Approaches to solving this problem include step-by-step assembly [89, 90], reservoir engineering to irreversibly pump towards a target state [91, 92], and adiabatic evolution from a known initial state [93, 94]. Here we construct low-entropy quantum fluids of light in a Bose Hubbard circuit by combining particle-by-particle assembly and adiabatic preparation. We inject individual photons into a disordered lattice where the eigenstates are known & localized, then adiabatically remove this disorder, allowing quantum fluctuations to melt the photons into a fluid. Using our platform [31], we first benchmark this lattice melting technique by building and characterizing arbitrary single-particle-in-a-box states, then assemble multi-particle strongly correlated fluids. Inter-site entanglement measurements performed through single-site tomography indicate that the particles in the fluid delocalize, while two-body density correlation measurements demonstrate that they also avoid one another, revealing Friedel oscillations characteristic of a Tonks-Girardeau gas [67, 95]. This work opens new possibilities for preparation of topological and otherwise exotic phases of synthetic matter [24, 38, 96]. This thesis chapter is adapted from [97].

5.1 Introduction

Synthetic materials, which are composed of interacting ions [46], atoms [41] or photons [22, 38], rather than interacting electrons as in solid state materials, offer a unique window into the equilibrium and dynamical properties of many-body quantum systems. Near-equilibrium, minimal realizations of superconductors [98], Mott insulators [43], and topological bands [24,

25] have elucidated the essential physics of these materials. Lattice-site [99] and time [100] resolved probes have exposed previously inaccessible quantities like entanglement [101] to direct observation.

Recently, synthetic matter efforts have begun to explore explicitly out-of-equilibrium phenomena including time crystallinity [26, 27], many-body localization [2, 15], quantum scarring [28], and bad-metal transport [102], with prospects to explore phenomena including light-induced superconductivity [103] and measurement-induced phase transitions [29]. These experiments are particularly impactful for benchmarking computational tools, as late-time dynamics of moderately sized quantum systems are already beyond the capabilities of state-of-the-art numerics [104].

Often neglected is the fact that preparing equilibrium states is itself an intrinsically non-equilibrium process, because driving a quantum many-body system to a desired target state requires *dynamics*. This challenge is typically overlooked in the solid state, where thermalization of long-lived electrons with broadband thermal reservoirs allows for robust entropy removal despite fundamentally inefficient thermalization. In synthetic materials, limited particle lifetimes make it crucial to develop optimized state preparation schemes that approach the fundamental quantum speed limits.

Efficient preparation of many-body states of ultracold atoms typically involves: (i) Laser cooling, where scattered light removes entropy from individual atoms; (ii) Evaporative cooling, where collisions dump entropy into consequently-lost atoms, producing a Bose-Einstein condensate (BEC); and (iii) Adiabatic variation of the Hamiltonian, so that the weakly interacting (BEC) ground state of the initial Hamiltonian evolves into the strongly interacting ground state of the final Hamiltonian. This approach has been employed to produce, for example, Mott insulating [43] and magnetically ordered [17, 105] synthetic matter.

Materials composed of microwave photons [38] offer the unique possibility of efficient thermalization via coupling to arbitrarily-designed low-entropy reservoirs shaped through

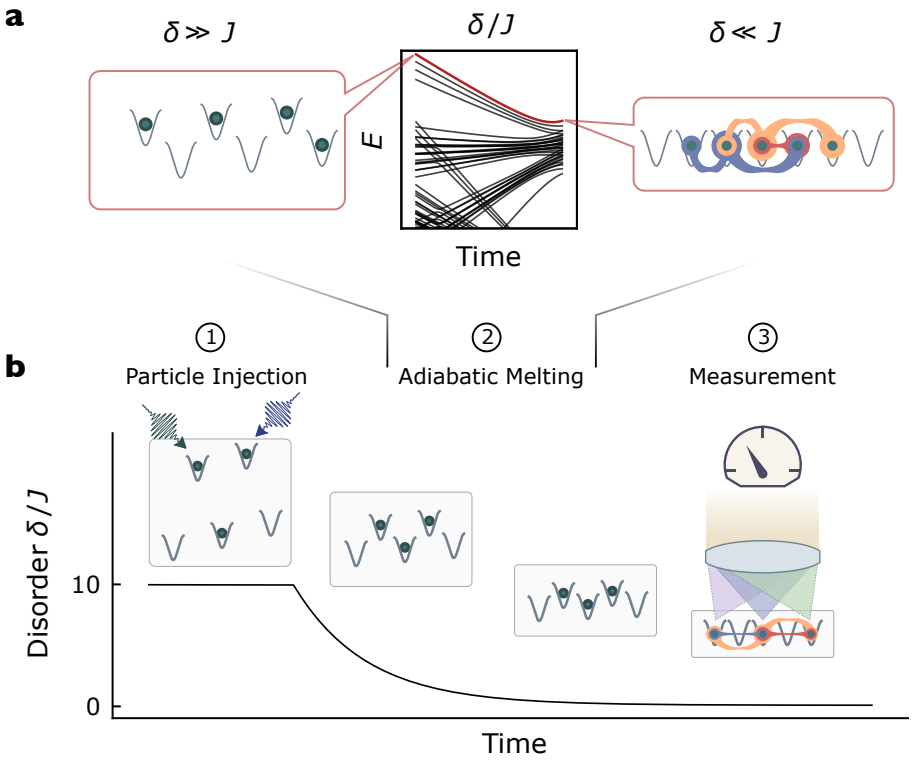

Figure 5.1: **Individually addressed many-body states in the Bose-Hubbard circuit**. **a,b.** To prepare (near) arbitrary eigenstates of the disorder-free Hubbard lattice, we impose strong ($|\delta_i| \gg |J|$) controlled disorder, ensuring that all eigenstates are products of localized photons on individual sites. ① In this disordered configuration it is then straightforward to excite an arbitrary eigenstate by injecting photons into individual lattice sites. ② If the disorder is slowly removed ($|\delta_i| \to 0$), the adiabatic theorem ensures that the system always remains in the same instantaneous many-body eigenstate, resulting in a highly entangled many-body state of the disorder-free lattice. ③ We characterize this many-body state via site-resolved occupation and correlation measurements. This figure is adapted from [97].

resonant filters [106]. This approach has been employed to stabilize Mott states of light [31], with prospects for Devil's staircase [107] and Laughlin-like [108] matter. Such reservoir engineering works extremely well to stabilize incompressible matter; preparation of compressible phases like superfluids [57] and certain quantum spin liquids [109] requires new approaches.

In this work we harness another strength of photonic materials platforms – particle-resolved *control*, to explore a new class of state preparation schemes compatible with compressible matter. Our approach marries the addressability of particle-by-particle injection with the robustness of adiabatic evolution, enabling us to assemble arbitrary-density fluids of strongly interacting microwave photons in our 1D Bose-Hubbard circuit [31]. We first localize all eigenstates by imposing disorder much stronger than the tunneling. We then inject individual particles into localized lattice orbitals, populating a single- or many-body eigenstate of our choosing. Finally we adiabatically remove the disorder, melting this localized eigenstate into a strongly correlated fluid via tunneling-induced quantum fluctuations. To characterize the fidelity of the preparation scheme, we introduce a reversible ramp protocol that maps diabatic and decay-induced excitations of the fluid onto localized excitations in the disordered lattice. We then characterize the fluid in two ways: (i) Two-body correlation measurements, which reveal that the photons avoid one another in the fluid phase, with a universal structure characteristic of a Tonks gas; and (ii) Inter-site entanglement measurements, via the purity of single-site density matrices, which reveal that the photons delocalize during the melt and relocalize when disorder is adiabatically re-introduced.

In what follows, we first introduce the Bose-Hubbard circuit platform and its capabilities. We then describe the disorder-localized preparation scheme and test it by assembling arbitrary single-particle quasi-momentum states. We validate adiabaticity of the scheme via the reversibility of the protocol, directly measuring entropy generation in the disordered lattice. We then apply the preparation scheme to assemble few-particle states, characterizing them using new tools which reveal that the particles simultaneously delocalize and anti-bunch,

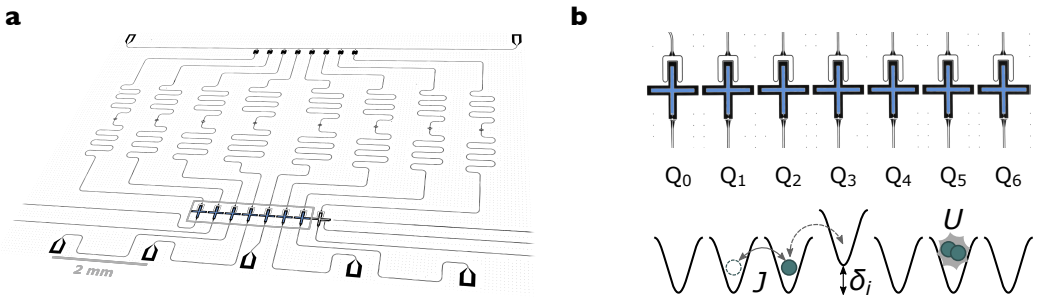

Figure 5.2: **Bose-Hubbard circuit platform**. The physical system, shown in **a**, consists of a one-dimensional array of capacitively coupled transmon qubits patterned on a large-area superconducting microwave circuit. This system behaves as a tight-binding lattice for photons [31] with site-resolved readout performed via microwave resonators dispersively coupled to each qubit, and real-time tuning of lattice disorder controlled by inductively coupled flux bias lines. **b.** The physics of this 1D circuit is well characterized by the Bose-Hubbard Hamiltonian describing the dynamics of interacting particles on a lattice. The transmon qubits (highlighted in blue) realize the lattice sites in which the photonic particles reside [53], with inter-site tunneling J arising from their capacitive coupling, and the on-site interaction U stemming from their anharmonicity. The flux bias lines tune the transmon energies to provide site-resolved control over lattice disorder δ_i. This figure is adapted from [97].

hallmarks of a strongly interacting fluid of light.

5.2 The Bose-Hubbard circuit

Our experiments take place in the quantum circuit shown in Fig. 5.2a, whose physics is captured by a one-dimensional Bose-Hubbard model for photons (illustrated in Fig. 5.2b):

$$\mathbf{H}_{\mathrm{BH}}/\hbar = J \sum_{\langle i,j \rangle} a_i^\dagger a_j + \frac{U}{2} \sum_i n_i \left(n_i - 1\right) + \sum_i (\omega_0 + \delta_i) n_i. \tag{5.1}$$

The operator $a_i^\dagger$ (a_i) creates (destroys) a microwave photon on site i, with the number operator on site i given by $n_i = a_i^\dagger a_i$. J is the nearest-neighbour tunneling rate, U is the on-site interaction energy, $\omega_0 + \delta_i$ is the energy to create the first photon in site i, and $\hbar$ is the reduced Planck constant.

The lattice sites in which the photons reside are realized as transmon qubits [38]. The anharmonicity of the transmon provides the photon-photon interaction on that site. Capacitive coupling between adjacent transmons allows for nearest-neighbor tunneling, and flux loops permit qubit-by-qubit tuning of the on-site energies. We operate with $J/2\pi = 9$ MHz, $U/2\pi = -230$ MHz; note that we have fixed the (otherwise arbitrary) gauge of the Hamiltonian with a tunneling term whose sign is opposite convention to compensate for our $U < 0$ and ensure that the highest energy single-particle states have the *lowest* quasi-momenta.

Site frequencies are tunable in real time over $(\omega_0 + \delta_i)/2\pi \in [4.1, 6.1]$ GHz (see Methods), enabling introduction of disorder δ_i up to 2 GHz, much larger than the tunneling energy. The photon lifetime in the lattice is $T_1 > 10\,\mu$s, so $|U| \gg J \gg 1/T_1$ providing ample time for the photons to collide, organize, and become entangled prior to decaying (see SI C.1). Site-resolved microscopy is achieved by capacitive coupling of each transmon to an off-resonant coplanar waveguide resonator, enabling direct readout of each transmon's occupation number through the dispersive shift of the resonator (see Sec. 3.2). Because the system operates in the hard-core limit $|U| \gg J$, the many-body states prepared are expected to be lattice-analogs of a Tonks-Girardeau gas of impenetrable bosons [64, 65].

5.3 Single-Particle Melting

Our protocol for preparing arbitrary eigenstates of a Hubbard lattice is highlighted in Fig. 5.1a,b. We begin by introducing strong disorder ($|\delta_i| \gg J$) in the lattice by controllably detuning the sites (see Sec 4.8). In this disordered configuration, tunneling is suppressed and all eigenstates are products of localized photons on individual sites. Such states are easily prepared by injecting photons into individual sites with calibrated microwave π-pulses. The lattice sites are then tuned into resonance by reducing the disorder $|\delta_i| \to 0$ slowly enough to maintain adiabaticity, allowing the system to remain in the same instantaneous eigenstate, which melts the particles into a correlated fluid. We then characterize the prepared states

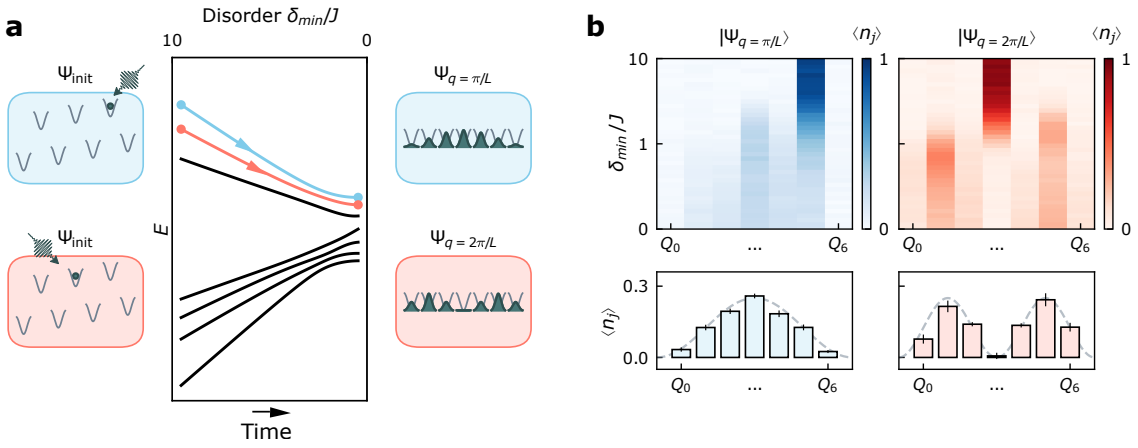

Figure 5.3: **Adiabatic assembly of single-particle eigenstates**. The simplest demonstration of the preparation protocol is the construction of single-photon particle-in-a-box states. In **a**, we plot the numerically-computed instantaneous eigenstate energies of a photon in a lattice, as disorder is reduced to zero over time. We highlight the highest (second-highest) energy eigenstates in blue (red). In the disordered lattice, the highest (second-highest) energy eigenstate is a particle localized to the single highest(second-highest) energy site, and as disorder is decreased this state is adiabatically transformed into the particle-in-a-box state with lowest (second-lowest) quasi-momentum. We demonstrate this process experimentally in **b** by assembling these lowest two quasi-momentum states. The blue (red) plots show the occupation of each of the lattice sites over time, as the disorder is adiabatically reduced to zero; here a single photon initially occupying the highest (second-highest) energy site, Q_5 (Q_3) delocalizes into the corresponding quasi-momentum state $q = \pi/L$ ($q = 2\pi/L$), shown at the final time in the bottom panels. Error bars reflect the S.E.M. This figure is adapted from [97].

by site-resolved probes of occupation, coherence, and correlation.

We begin by applying this preparation protocol to construction of single-photon particle-in-a-box eigenstates. The dependence of these eigenstates upon disorder, and their corresponding energies, are displayed pictorially in Fig. 5.3a. At maximum disorder (Fig. 5.3a, left) each eigenstate is localized to a single site, while near zero disorder the eigenstates are delocalized particle-in-a-box states (Fig. 5.3a, right). Adiabatic evolution ensures that the system remains in the same instantaneous eigenstate, forming a unique connection between the lattice site the photon occupies in the disordered configuration and the state into which it delocalizes. In Fig. 5.3b we prepare the highest-energy localized states and measure the

evolution of their densities as we adiabatically reduce the disorder to zero. The blue (red) data show the dynamics of a single photon prepared in the highest (second-highest) energy site, Q_5 (Q_3), as it delocalizes near degeneracy. The measured density profiles of the final states are sinusoidal, with zero and one nodes, respectively, matching the probability distributions for the $q = \pi/L$ and $q = 2\pi/L$ particle-in-a-box/quasi-momentum states.

Because photon loss renders our quantum system inherently open, we must balance the need for slow evolution (set by the energy gaps) to satisfy adiabaticity with the need to evolve faster than photon loss. We have developed a protocol to experimentally probe the adiabaticity of the process and extract the optimum ramp rate, without needing to perform tomography on a highly entangled state: We ramp the disorder down to zero and then back up, exactly reversing the downward ramp. We then measure the fraction of the time that the photon returns to its initial lattice site. Because all eigenstates are localized in the final, disordered lattice, this is a direct measure of the overlap of the final state with the initial state $|\langle\Psi_{\text{final}}|\Psi_{\text{init}}\rangle|^2$. Performing this experiment versus total evolution time $2t_{\text{ramp}}$, provides a measure of adiabaticity.

This process is depicted in Fig. 5.4a for a single particle, where it is applied to the preparation of the highest-energy quasi-momentum state as shown in Fig. 5.4b. For very fast ramps $t_{\text{ramp}} \ll J^{-1}$, the photon remains in its initial site because it lacks the time to tunnel even to its nearest neighbor. For intermediate ramp speeds $t_{\text{ramp}} \sim J^{-1}$, the photon has time to delocalize but not to adiabatically follow, and thus undergoes diabatic transitions to other quasi-momentum states as the disorder is reduced, leading to a decreased population of the initial site. When the ramp is sufficiently slow $t_{\text{ramp}} \gg J^{-1}$ the photon is able to delocalize, adiabatically follow the same eigenstate, and relocalize, resulting in near-unity occupation in the initial site. We employ extensions of this technique to multiple particles (see Extended Data Fig. SA.1) behind the scenes in order to optimize performance throughout the remainder of this work. This approach is particularly powerful because it is

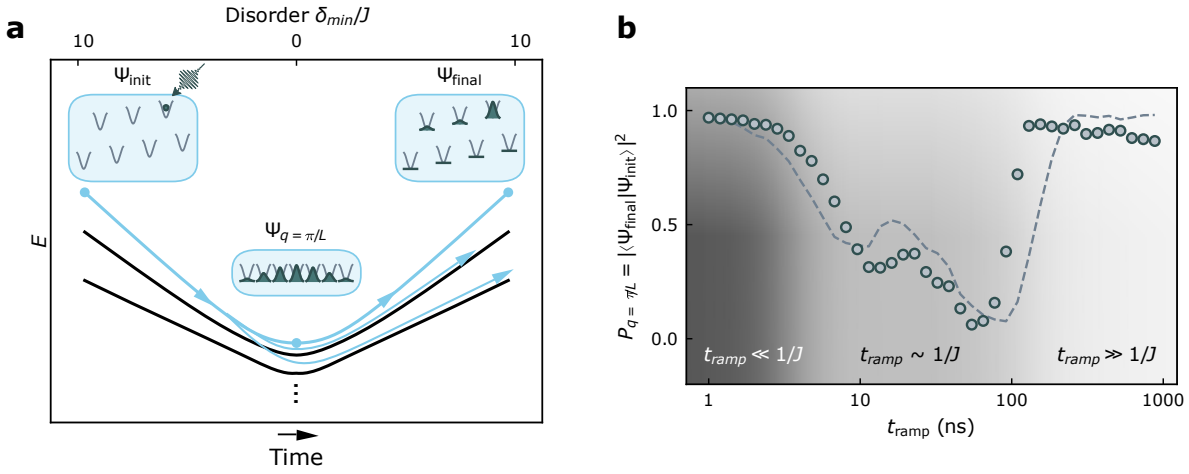

Figure 5.4: **Adiabaticity Criterion**. To characterize the time required for the adiabatic sweep, we follow the protocol depicted in **a**: (i) A photon is prepared in a particular site in the presence of disorder. (ii) The disorder is ramped down and back up over a variable time $2t_{ramp}$. (iii) The final occupation of the initially prepared site $|\langle\Psi_{\text{final}}|\Psi_{\text{init}}\rangle|^2$ is measured. The result of this protocol for the highest energy state, shown in **b** (with dashed parameter-free theory), demonstrates that extremely fast ramps $t_{\text{ramp}} \ll J^{-1}$ do not afford the photon sufficient time to tunnel and thus the photon remains in its initial site. At intermediate ramp speeds $t_{\text{ramp}} \sim J^{-1}$ the photon undergoes diabatic transitions to other eigenstates and thus ends up in other lattice sites, reducing the occupation of its initial site. Only slow ramps $t_{\text{ramp}} \gg J^{-1}$ allow the photon to adiabatically follow the initial eigenstate, delocalizing and subsequently relocalizing to its initial site. It is these slowest ramps that we employ for state preparation. Error bars reflect the S.E.M.; in **b** they are smaller than markers. This figure is adapted from [97].

agnostic to the details of the physical platform and target state.

5.4 Correlated Fluid Melting

When multiple photons simultaneously reside in our Hubbard circuit, interactions strongly modify the behaviour of the system. At unit average occupancy ($\bar{n} \equiv N/L = 1$, where N is the number of photons and L is the number of sites), the ground state is a Mott insulator [31] because the photons cannot move without immediately hitting a neighbor, so transport is fully impeded. Away from unit occupancy the ground state is a fluid: even if U fully blocks photons passing through one another, they can still delocalize, move, and exchange momentum with their neighbors.

Strongly interacting fluids are challenging to prepare by reservoir engineering techniques [106], which rely on irreversible photon injection that halts when adding the next photon costs substantially more energy than prior photons. The delocalization of the photons in the fluid makes it compressible: the energy required to inject additional photons changes smoothly with density, changing abruptly only at the unit-filled Mott state.

Here we prepare a compressible, strongly correlated fluid of light away from unit filling via a multi-particle variant of our disorder-assisted preparation scheme: we determine the filling by the number of photons that we coherently inject, and eigenstate by the sites into which we inject photons. In our $L = 7$ site lattice we inject up to $N = 6$ photons in order to remain below unit filling. Since our interactions are attractive, $U < 0$, the 'ground' state is actually the highest energy state for a given photon number; beyond this detail, the sign of U does not impact the physics.

Fig. 5.5a depicts the many-body spectrum for various fluid photon numbers versus disorder. The spectrum splits first into bands of fixed photon number separated by ω_0, and then into bands of fixed numbers of overlapping particles separated by the interaction energy U. Within each of these bands, the states are split by fractions of the tunneling energy J,

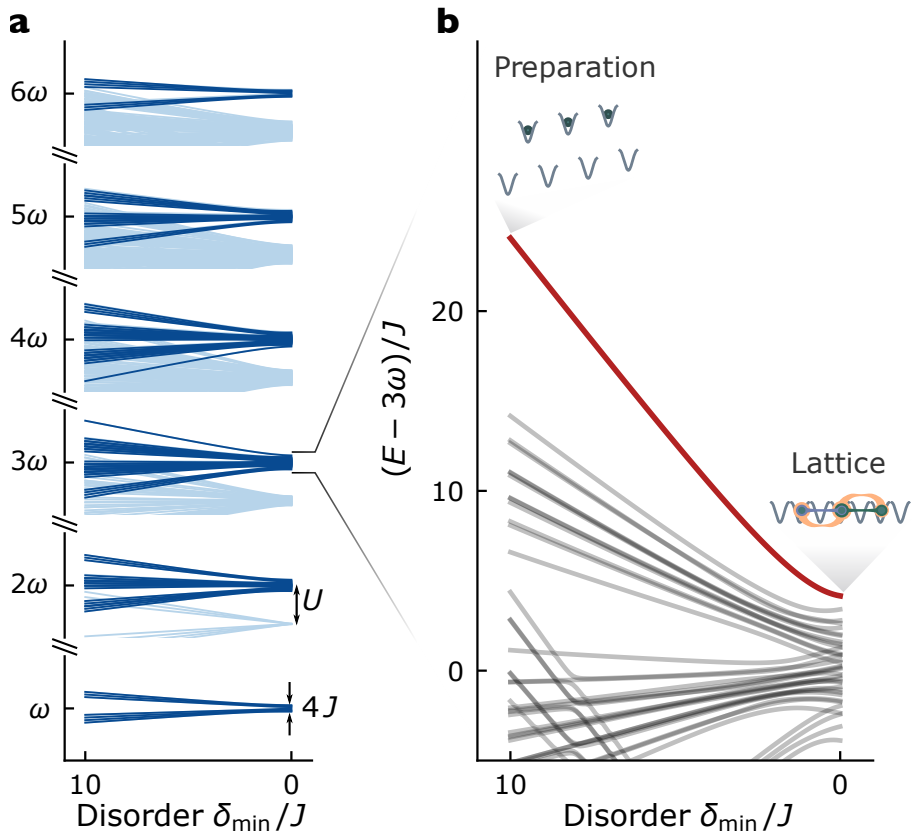

Figure 5.5: **Adiabatic preparation of strongly correlated fluids of light: Energy Spectra**. The ground states of the Hubbard lattice below unit filling are compressible fluids because motion of the particles is not fully blocked by collisions as it would be in the unit-filled Mott state. This is reflected in the many-body spectrum in **a**, where in the absence of disorder, there are bands of states (dark blue) of width $\sim J$ in which the photons do not overlap with one another, rather than a single state, as would be the case for an incompressible system. These states are spectroscopically isolated by the onsite interaction U from all other states (light blue). In the incompressible Mott state there is a single gapped (by U) ground state. In the particular case of three particles in the lattice shown in **b**, the highest energy state, which is the fluid 'ground' state (because $U, J < 0$), exhibits the largest energy gap to all other states, and can thus be prepared most quickly. This figure is adapted from [97].

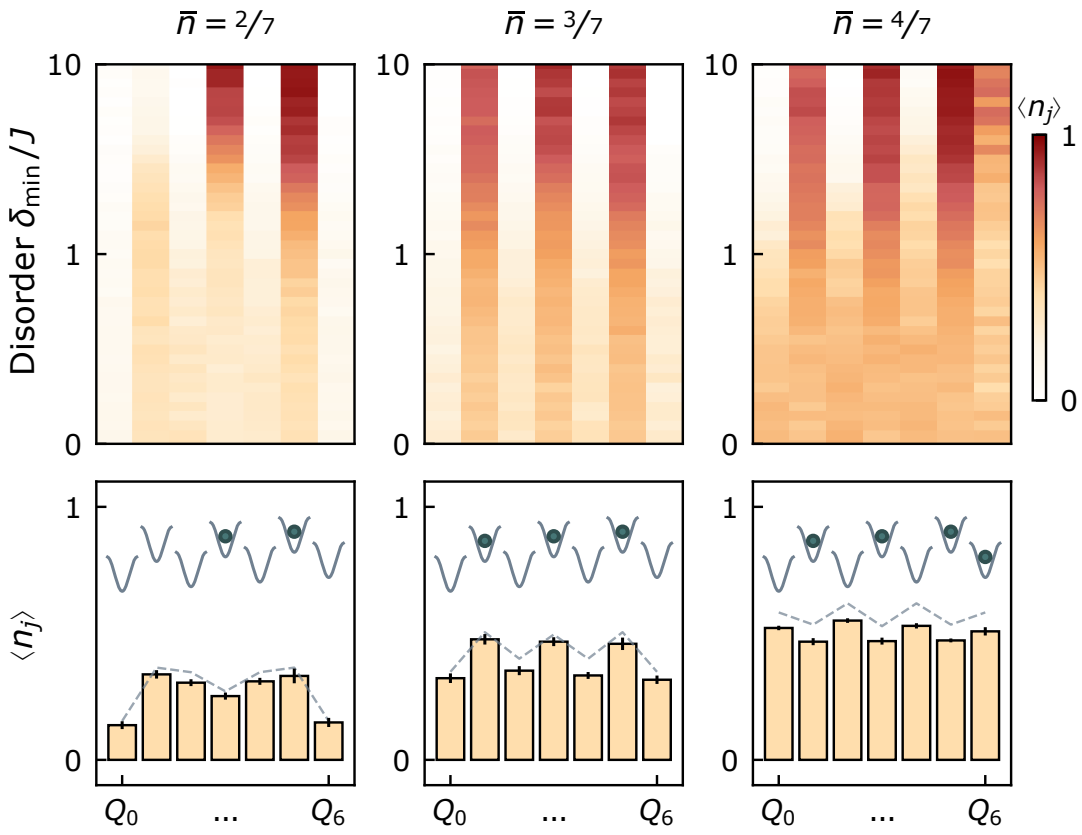

Figure 5.6: **Adiabatic preparation of strongly correlated fluids of light: Density Profiles**. We adiabatically prepare the fluid ground states for two, three, and four particles in the seven site lattice. The upper panels display the density profiles for these states as the system is tuned from disordered to ordered configurations and the particles delocalize and become entangled. We highlight the measured fluid densities at degeneracy (bars in lower panels) compared to theory (dashed curve). The insets depict particle placements in the disordered configuration, which adiabatically connect to the fluids. This figure is adapted from [97].

reflecting phonon excitations of the fluid. Fig. 5.5b provides a detailed view of the spectrum relevant for preparing a three-photon ground state. The preparation trajectory is highlighted, beginning in the disordered lattice with photons occupying the three highest-energy sites, and ending in the ordered lattice with the photons delocalized and entangled.

We perform the disorder-assisted preparation for up to four photons, measuring, in Fig. 5.6, average density profiles as the lattice is tuned from disordered to disorder-free configurations (see Extended Data Fig. SA.2 for 5 & 6 photons). These data demonstrate that during the melt the photons delocalize from their initial sites into all lattice sites, with the melted density profiles in good agreement with the disorder-free numerics from exact diagonalization.

Because we operate at large U/J, the physics is well-captured by the Tonks-Girardeau model (see Sec. 2.3), whose ground state is of the Bijl-Jastrow form. This wavefunction is written as the product of single- and two-particle components $\Psi_B(\mathbf{x}) = \phi(\mathbf{x})\varphi(\mathbf{x})$, for $\mathbf{x} = (x_0, x_1, \ldots, x_6)$ [66]. The single-particle component $\phi(\mathbf{x}) = \prod_{i=0}^{6} \cos(\pi x_i/L)$ places each photon in the lowest-energy particle-in-a-box state of the lattice, while the two-particle component $\varphi(\mathbf{x}) = \prod_{i<j} |x_i - x_j|$ keeps the photons apart (whilst minimizing their kinetic energy) by ramping the wavefunction to zero whenever they overlap.

In the absence of interactions, the ground state density would be independent of particle number up to an overall scale, reflecting the single-particle eigenstate $q = \pi/L$ of Fig. 5.3b. The increasingly large deviations from such a sinusoidal form as density increases indicate that photon-photon collisions are shaping the fluid density profile. A deeper understanding of the fluid's structure requires exploring correlations and entanglement, which is the subject of the remainder of this investigation.

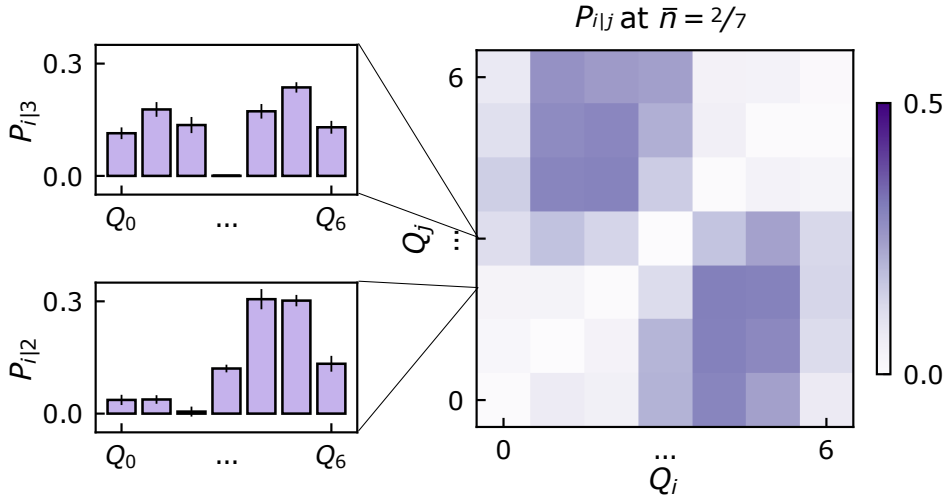

Figure 5.7: **Microscopy of the strongly correlated fluid: anti-bunching and delocalization in conditional probability**. The photon liquid is characterized by photons simultaneously (i) avoiding each-other and (ii) delocalizing. To show that the photons avoid one another in the fluid we measure the two-body correlator $P_{i|j}$ at $\bar{n} = 2/7$. $P_{i|j}$ quantifies the probability of detecting a photon at site i given one detected in site j. Suppression near $i = j$ reflects both the hard-core constraint and the minimization of kinetic energy by smoothing their wavefunction and thus avoiding nearby sites. The upper (lower) inset showing $P_{i|3}$ ($P_{i|2}$) demonstrates that when the first photon is detected in the middle site (one site left of the middle), the second photon occupies particle-in-a-box states boxes imposed by repulsion of the first photon. Error bars represent the S.E.M. (see SI A.3). This figure is adapted from [97].

5.5 Fluid Correlations

In the Tonks regime the photon fluid should exhibit short-range repulsion between the particles arising from the Hubbard $|U| \gg J$. We probe this physics directly through the two-body correlator $P_{i|j}$ which quantifies the probability of detecting a photon at site i conditioned on one being detected at site j. If we consider a two-particle state with a wavefunction $\Psi(x_1, x_2)$, the detection of a particle at lattice site $x_1 = x_j$ collapses the wavefunction to a product state $\Psi(x_1, x_2) = \delta(x_1 - x_j)\Psi'(x_2)$, with the conditional probability of the second photon given by $P_{i|j} = |\Psi'(x_i)|^2$. This measurement is performed on a minimal two-particle fluid in Fig. 5.7, where the insets show $P_{i|2}$ and $P_{i|3}$. The strong occupation suppression at $i = j$ reflects the hard-core constraint that forces the system wavefunction to vanish when two particles are on top of each other. Furthermore, the suppression *near* $i = j$ reflects the photons' preference to minimize their wavefunction curvature and thus kinetic energy. The projective measurement of a photon in the lattice has effectively reshaped the two-particle fluid into a single-particle fluid confined in *two* boxes, where the pinned (detected) photon acts as a potential barrier for the second photon.

To probe two-body correlations in fluids of more than two photons, we measure the system-averaged, normalized two-body correlator given by:

$$g^{(2)}(x) = \frac{1}{\bar{n}^2} \sum_i \langle n_i \, n_{i+x} \rangle, \tag{5.2}$$

which quantifies the probability of simultaneously detecting two particles separated by x (in lattice sites), normalized to the average density $\bar{n}$. The central intuition, that each photon has less 'space' at higher densities, is captured in Fig. 5.8, where the antibunched region ($g^{(2)}(x) < 1$) gets narrower as density increases. Indeed, when the separation is rescaled by the density, the correlator collapses onto a universal parameter-free Tonks-Girardeau theory, with each particle occupying a volume $1/\bar{n}$, and characteristic Friedel oscillations. These

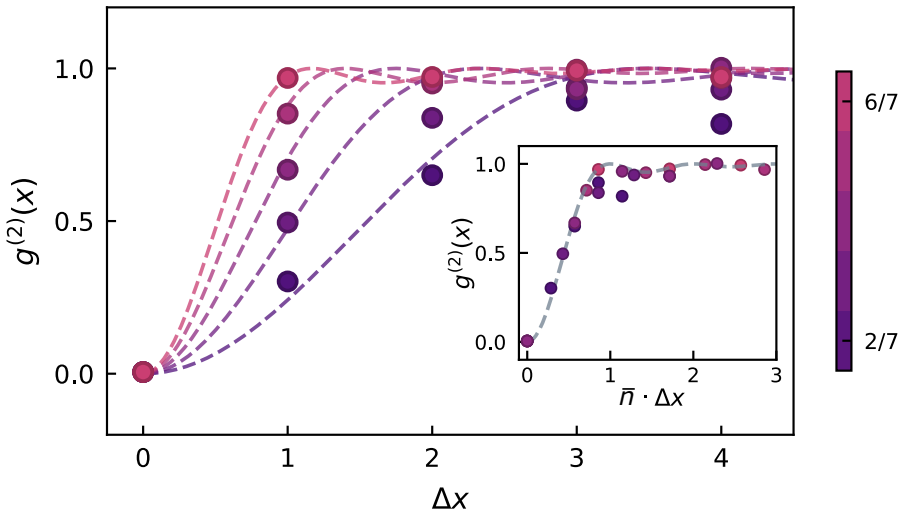

Figure 5.8: **Microscopy of the strongly correlated fluid: anti-bunching and delocalization in two-body correlator**. Here, we plot the normalized two-body correlator at various particle numbers (densities), demonstrating that the anti-correlation length decreases as the density increases, in agreement with a parameter-free Tonks-Girardeau theory (see Sec 2.3) and the intuition that photons occupy less space at higher densities. Also apparent are Friedel oscillations at wavevector $k_F = \pi\bar{n}$, signalling photon fermionization. Large-separation correlation data, polluted by edge effects, are omitted (see SI Fig. SA.4). Error bars represent the S.E.M. (see SI A.3); where absent, they are smaller than the data points. This figure is adapted from [97].

correlations, oscillating at the Fermi momentum, $k_F = \pi\bar{n}$, are a direct signature of the 'fermionization' of the photons [67].

5.6 Fluid Delocalization & Entanglement

As the photons melt into a fluid they optimize their energy by delocalizing as much as possible whilst avoiding one another. The two-body correlator explored in Sec. 5.5 quantifies this avoidance, and in this section we explore their delocalization. To achieve this we probe the entanglement of a single site with the remainder of the system by employing a metric developed for interacting spins [110]: we measure the reduced density matrix of each individual lattice site ρ_i, quantifying how strongly it is entangled with rest of the lattice from its impurity $1 - \mathrm{Tr}(\rho_i^2)$. Our global measure of multipartite entanglement/delocalization is this impurity averaged over all sites:

$$E_{\mathrm{gl}} = 2 - \frac{2}{N}\sum_{i=1}^{N} \mathrm{Tr}(\rho_i^2). \tag{5.3}$$

We wish to understand how the global entanglement scales with the number of particles and lattice disorder, which dictates the degree of delocalization. In Fig. 5.9b the entanglement is measured for a three-particle fluid as we vary the disorder along the adiabatic preparation trajectory. In the limit of strong lattice disorder the entanglement between sites is very small since the three-particle state is a product of localized photons. As we reduce the disorder, the entanglement grows, saturating to a maximum value when the sites are degenerate and the photons become fully delocalized. Residual entanglement in the disordered lattice arises from dissipative coupling to the environment – decoherence. We exclude the possibility that decoherence is the source of entanglement in the fluid phase by ramping the lattice back to its initial disordered configuration. The fact that the measured entanglement drops definitively proves that the entanglement observed at degeneracy comes from delocal-

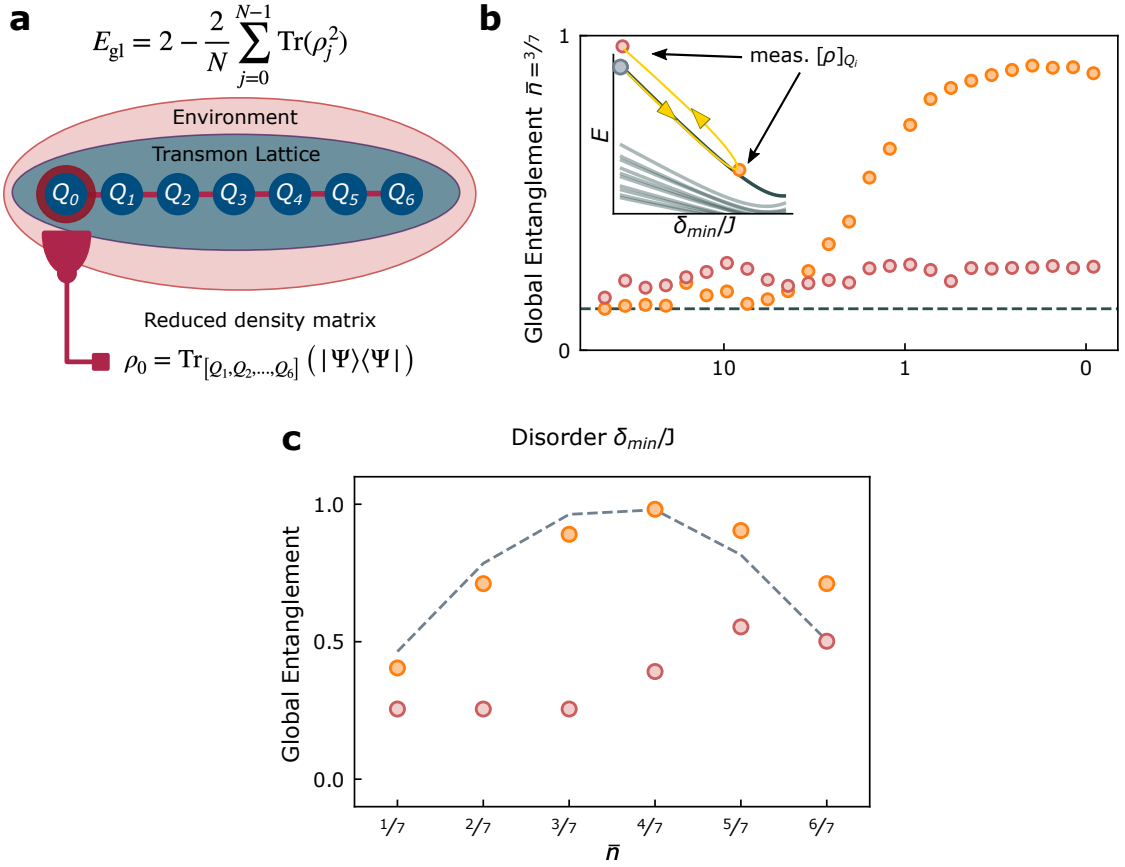

Figure 5.9: **Fluid Entanglement**. **a.**We probe delocalization during three-particle fluid preparation by measuring the average entanglement between each site and the rest of the system, $E_{gl} \equiv 2(1 - \langle p_i \rangle)$ (orange) via the purity of the single-site reduced density operator $p_i \equiv Tr(\rho_i^2)$. **b.**In the disordered lattice the state is a product of localized photons so entanglement is small. In the disorder-free lattice photons delocalize, purity drops and entanglement increases. We distinguish environmental entanglement (decoherence) from inter-site entanglement by returning to the initial configuration before measuring (red); this quantity remains small, proving the system remains un-entangled with the environment. The inset depicts the measurement time within the ramp for each curve. **c**. The entanglement peaks at half-filling where each site's occupancy provides maximal information about the rest of the system. Theoretical (dashed) particle-hole symmetry about ($\bar{n} = 1/2$) is not reflected in the data due to increased decay with more particles (increased entanglement after reverse ramp at high densities, red). Error bars represent the S.E.M. (see SI A.3); where absent, they are smaller than the data points. This figure is adapted from [97].

ization, and not dissipation. Similar measurements and conclusions are extracted for all the other particle sectors (see Extended Data Fig. SA.3).

The dependence of the entanglement at degeneracy on the average density is displayed together with the expected theoretical calculation in Fig. 5.9b. The discrepancy at larger filling fractions is due to increased particle loss, as anticipated from the increased entanglement after the time-reversed ramp. As highlighted in theory, there is a particle-hole symmetry in the extracted entanglement measure. This is expected because in the hardcore limit, particles at filling $\bar{n}$ tunnel and avoid one another analogously to holes at filling $1-\bar{n}$. Entanglement is maximized at half-filling because that is the situation in which knowledge of the occupancy of any given site provides the *most* information about the occupancy of adjacent sites: at lower (higher) fillings, most sites are empty (occupied), so knowledge of any given site's occupancy provides less information.

5.7 Outlook

In this work we have demonstrated a way to harness controlled disorder to individually index and prepare the eigenstates of a strongly interacting many-body system. In particular, we have assembled quantum fluids of light in a 1D Bose-Hubbard circuit composed of capacitively coupled transmon qubits. Leveraging our site-resolved tuning capabilities, we tune the qubits out of resonance with one another, individually excite only particular qubits, and then melt these excitations into a fluid. Site-resolved probes of correlation, entanglement, and reversibility reveal that this system realizes a Tonks-Girardeau gas [67, 95]. The dissipative stabilization technique of Ref. [31] will yield lower entropy per particle when manybody gaps are large but the gaps at the critical point are small; the approach demonstrated here is preferable when the phase is compressible, so dissipative stabilization will be unable to stabilize a specific particle number. Leveraging both techniques, the Bose-Hubbard circuit is now prepared to study most phases of quantum matter. It remains to be seen how our

adiabatic preparation approach scales with system size; it seems certain that it will be controlled by the Kibble-Zurek mechanism [111] in the thermodynamic limit, though the precise disorder employed will likely impact the structure of the excitations generated at the critical point.

By combining the techniques developed in this work with topological [15, 23] circuit lattices, it should be possible to prepare topological fluids of light [89]. In conjunction with auxiliary qubits, these adiabatic preparation techniques will enable direct measurements of out-of-time-order correlators & information scrambling [112], as well as anyon statistics [113].

CHAPTER 6

MANYBODY INTERFEROMETRY OF QUANTUM FLUIDS

Characterizing strongly correlated matter is an increasingly central challenge in quantum science, where structure is often obscured by massive entanglement. From semiconductor heterostructures [114] and 2D materials [115] to synthetic atomic [42], photonic [22, 38] and ionic [116] quantum matter, progress in *preparation* of manybody quantum states is accelerating, opening the door to new approaches to state characterization. It is becoming increasingly clear that in the quantum regime, state preparation and characterization should not be treated separately – entangling the two processes provides a quantum advantage in information extraction. From Loschmidt echo [117] to measure the effect of a perturbation, to out-of-time-order-correlators (OTOCs) to characterize scrambling [112, 118, 119] and manybody localization [14], to impurity interferometry to measure topological invariants [113], and even quantum Fourier transform-enhanced sensing [120], protocols that blur the distinction between state preparation and characterization are becoming prevalent. Here we present a new approach which we term "manybody Ramsey interferometry" that combines adiabatic state preparation and Ramsey spectroscopy: leveraging our recently-developed one-to-one mapping between computational-basis states and manybody eigenstates [97], we prepare a superposition of manybody eigenstates controlled by the state of an ancilla qubit, allow the superposition to evolve relative phase, and then reverse the preparation protocol to disentangle the ancilla while localizing phase information back into it. Ancilla tomography then extracts information about the manybody eigenstates, the associated excitation spectrum, and thermodynamic observables. This work opens new avenues for characterizing manybody states, paving the way for quantum computers to efficiently probe quantum matter. This section is adapted from Ref. [121].

6.1 Introduction

Advances in controllable quantum science platforms have opened the possibility of creating synthetic quantum materials, in which the physical laws governing the material are built-to-order in the lab [22, 38, 41, 46]. Such experiments enable time- and space-resolved probes [44, 99, 122] of quantum dynamics inaccessible in solid-state matter, as well as explorations of extreme parameter regimes [16, 39, 43, 123, 124]. Indeed, as the community has become increasingly adept at leveraging the flexibility of synthetic matter platforms to realize arbitrary physical laws, we now face the challenge of capitalizing on this same flexibility for preparing and characterizing quantum manybody states.

In electronic materials, preparing low-entropy equilibrium states relies upon *refrigeration*: harnessing the coupling of the material to a low-temperature reservoir that can absorb its entropy. By contrast, synthetic material platforms are known for their coherent, low-dissipation evolution, and hence their lack of reservoir coupling. State preparation has thus relied upon the development of new approaches based upon engineered reservoirs [30, 31, 38, 125–127] and adiabatic evolution [43, 105, 128], elucidating, among other things, microscopic aspects of quantum thermodynamics [129, 130] and the importance of symmetry breaking [131], respectively.

Even once a manybody state is prepared, characterizing it presents unique challenges. The intuitively simplest but technically most demanding characterization approach is state tomography, where n-body correlations are measured in complementary bases, allowing complete reconstruction of the system density matrix [132]. This approach has the advantage that *all* information about the state is extracted, and the disadvantage that the required statistics (and thus measurement time) scale exponentially with system size. If *specific* rather than *complete* information about the state is desired, more carefully crafted protocols have been shown to relax measurement requirements: Expansion imaging measures single-particle coherence [133]; noise correlations measure two-body ordering [134]; in-situ density probes

equation of state [135]; Bragg spectroscopy is sensitive to density- (and spin-) waves [136]; particle-resolved readout accesses higher-order correlations [16, 18, 37, 99, 137]; parity oscillations are clear signatures of GHZ states [138]; single-qubit tomography probes global entanglement [16, 97]; and shadow tomography [139] provides an efficient way to extract observables from few measurements.

It has nonetheless become apparent that treating state *preparation* and state *characterization* as independent does not fully leverage quantum advantage – approaches that entangle the two tasks via an ancilla can be vastly more performant: Proposals & experiments to quantify scrambling [112, 118, 119] and verify manybody localization [14] rely upon out-of-time-order correlators (OTOCs) that compare manybody states to which a specific operator is applied either before or after coherent evolution. This is achieved by entangling the time at which the operator is applied with the state of an ancilla, and subsequently performing tomography on the ancilla. Similarly, Loschmidt echoes directly measure the impact of perturbations via state overlap measurements following evolution under two similar Hamiltonians [117, 140]. Sensitivity & dynamic range enhancements in sensing [120] can be achieved by sandwiching ancilla-conditioned dynamics between quantum Fourier transforms. Entangling initial states with an ancilla and applying ancilla-conditioned evolution can further probe anyon braiding phase [21] and system spectrum [15, 54].

In this work we introduce *manybody Ramsey interferometry* as a direct probe of thermodynamic observables: we entangle which manybody state we prepare in a Bose-Hubbard circuit with the state of an ancilla qubit, allow the superposition to evolve, disentangle from the ancilla, and perform ancilla tomography to learn about the manybody states. We rely upon our recently-demonstrated reversible one-to-one mapping of computational states onto manybody states [97] to achieve the ancilla/manybody state entanglement. Because we entangle and then disentangle the ancilla from the manybody system, we localize the sought-after information in a single qubit for efficient, high signal-to-noise readout, rather

than extracting it from a many-qubit state space [15, 54, 141, 142].

In Section 6.2 we introduce our circuit platform and manybody Ramsey protocol. In Section 6.3 we demonstrate the protocol and in Section 6.4 we use manybody Ramsey to probe adiabaticity of state preparation. Finally in Section 6.5 we employ manybody Ramsey to directly measure thermodynamic observables of a strongly interacting quantum fluid by studying superpositions of (i) particle number and (ii) system size.

6.2 The Platform

The properties of our synthetic quantum material platform are accurately captured by a 1D Bose-Hubbard model (see Fig. 6.1b), describing bosonic particles tunneling between lattice sites at rate J, in the presence of onsite interactions of energy U,

$$\mathbf{H}_{\mathrm{BH}}(t)/\hbar = J \sum_{\langle i,j \rangle} a_i^\dagger a_j + \frac{U}{2} \sum_i n_i \left(n_i - 1\right) \tag{6.1}$$

$$+ \sum_i \left(\omega_{\mathrm{lat}} + \delta_i(t)\right) n_i. \tag{6.2}$$

Our Hubbard lattice is realized in a quantum circuit [31, 38, 48]: sites are implemented as transmon qubits, particles as microwave photon excitations of the qubits, tunneling (J) as capacitive coupling between the qubits (Fig. 6.1a,b), and onsite interactions (U) as transmon anharmonicity. Lattice site energies (qubit frequencies) can be individually & dynamically tuned using flux bias lines (see Sec 3.2). For this work $J/2\pi = -9$ MHz, $U/2\pi = -240$ MHz, and $\omega_{lat}/2\pi \approx 5$ GHz. The tuning range of our qubits extends from $\omega_{qb}/2\pi \sim 3 - 6$ GHz. The photon lifetime $T_1 \approx 40$ µs is much longer than the timescale of the manybody dynamics (see SI C.2 for details).

We recently demonstrated adiabatic preparation of photonic fluids by leveraging real-time ($\ll$ tunneling time) control of lattice disorder [97]. This protocol begins with lattice sites

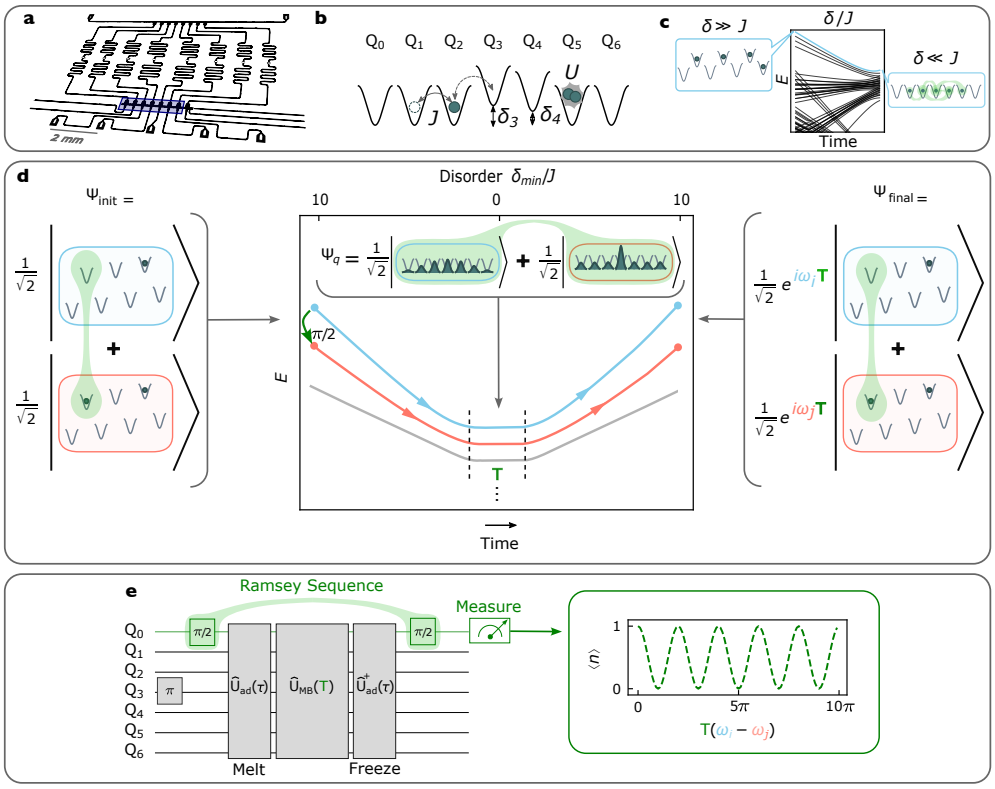

Figure 6.1: **Preparing and Interfering Manybody States**. The quantum system probed in this work consists of a chain of seven capacitively coupled superconducting transmon qubits [53] (blue in **a**) connected to site-resolved readout resonators (meandering traces) and flux control (bottom traces). **b,** The system is well described by the Bose-Hubbard model: particles (microwave photons) coherently tunnel between lattice sites (qubits) at a rate J, with on-site interactions $U \gg J$ arising from the transmon anharmonicity [31, 38, 48]. Real-time flux tuning provides control of lattice site energies (δ_i for site i), allowing the deterministic manipulation of disorder that we leverage to build highly entangled states: **c,** Starting in a highly disordered lattice, we initialize the system in the highest energy N-particle eigenstate by applying π-pulses to the N highest-energy sites (left), and adiabatically removing disorder to convert these states into eigenstates of the quantum fluid (right) [97]. **d,** To interfere superpositions of such states, we replace one of the assembly π-pulses with a $\frac{\pi}{2}$ pulse (green), producing a superposition of two (red/blue) eigenstates; adiabatically removing disorder produces a superposition of two manybody fluid states; coherently evolving for a time T allows the eigenstates to accumulate a relative phase proportional to their energy difference; ramping back to the disordered configuration (right) relocalizes the phase difference into the single qubit that started in a superposition; a final $\frac{\pi}{2}$ pulse on this qubit maps the phase information onto qubit occupancy for measurement. **e** reinterprets the full manybody Ramsey sequence as a set of gates on the qubits comprising the lattice, resulting in an interference fringe vs evolution time T.This figure is adapted from Ref. [121].

tuned apart in energy by more than the tunneling J. In this configuration, the many-particle eigenstates are localized into product states over individual sites, such that any eigenstate may be prepared via site-resolved microwave π-pulses that inject individual photons. By next adiabatically removing the lattice disorder, we smoothly convert the localized eigenstates of the disordered system into the corresponding highly entangled eigenstates of the disorder-free system (Fig. 6.1c). The combination of the one-to-one mapping and the ease of state preparation in the disordered (staggered) system render it straightforward to prepare *any* eigenstate of the ordered system provided sufficient coherence time to ensure adiabaticity in the disorder-removal ramp.

We now harness this precise eigenstate preparation to explore controlled interference of many-particle quantum states. Our approach can be understood in analogy to traditional Ramsey spectroscopy of a single qubit [143] with states $|0\rangle$ and $|1\rangle$: in this simpler case, a system prepared in $|0\rangle$ is driven into an equal superposition of $|0\rangle$ and $|1\rangle$ with a $\frac{\pi}{2}$ pulse, and after an evolution time T, the phase accrued on between $|0\rangle$ and $|1\rangle$ is read out with a second, phase-coherent $\frac{\pi}{2}$ pulse: the resulting population difference between $|0\rangle$ an $|1\rangle$ states oscillates (versus evolution time T) at a frequency set by the energy difference between the states.

To extend the protocol to measurement of the phase difference between two manybody states, we take the single-qubit Ramsey sequence above and sandwich the delay time T between qubit-conditioned assembly and disassembly of the manybody states. We call this approach 'manybody Ramsey interferometry' to connect with previous work exploring non-adiabatic evolution of manybody systems [119, 141, 142]. This procedure maps the phase accrued between the manybody states *entirely* onto the single qubit, avoiding any reduction in contrast due to residual entanglement, at measurement time, with the manybody system. The enabling ingredient for this protocol is qubit-conditioned manybody state preparation, which we implement via our disorder-assisted adiabatic assembly techniques [97].

An example of the full protocol is shown in Figure 6.1d. In the presence of disorder, we prepare a superposition of the highest energy states of the $N = 1$ and $N = 2$ particle manifolds $|\Psi_i\rangle = \frac{1}{\sqrt{2}}(|0000010\rangle + |0001010\rangle) = |000\rangle \otimes \frac{|0\rangle+|1\rangle}{\sqrt{2}} \otimes |010\rangle$. The key to this protocol is that in the presence of disorder the superposition of the two highest-energy manybody states is realized as a superposition of a *single control qubit*, realized with a $\frac{\pi}{2}$ pulse. As we adiabatically remove the disorder the localized states melt into corresponding eigenstates of the quantum fluid. During the subsequent hold time T, these states will accrue a relative phase proportional to their energy difference, $(\omega_i - \omega_j)T$. Finally, to relocalize the information back into the control qubit we adiabatically re-introduce lattice disorder, producing the final state: $|\Psi_f\rangle = \frac{1}{\sqrt{2}}(|0000010\rangle + e^{i(\omega_i-\omega_j)T}|0001010\rangle) = |000\rangle \otimes \frac{|0\rangle+e^{i(\omega_i-\omega_j)T}|1\rangle}{\sqrt{2}} \otimes |010\rangle$. The phase accrued between the manybody states has now been written entirely into the control qubit. We extract that phase information (and thus the manybody energy-difference) with a final $\frac{\pi}{2}$ pulse on the control qubit and a population measurement in the $|0\rangle$,$|1\rangle$ basis. The complete pulse sequence is illustrated in Fig. 6.1e.

6.3 Demonstration of the Protocol

We benchmark our manybody Ramsey protocol by studying the superposition of 1- and 2-photon fluid ground states in our Hubbard circuit. In Fig. 6.2a we prepare these states separately (red and blue boxes) by π-pulsing localized particles into the disordered lattice & then adiabatically removing the disorder, finding good agreement of the measured *in-situ* density profiles with a parameter-free Tonks gas model [64, 65] (see Sec 2.3). When the second particle is instead injected with a $\frac{\pi}{2}$ pulse, we create the desired superposition state, with a density profile reflecting the average of the two participating eigenstates (green box).

To measure the energy difference between these states we must interfere them. We achieve this by replacing the in-situ density measurement with a coherent evolution time T, allowing the states to accrue a relative phase (Fig. 6.2b), followed by adiabatically reintroducing the

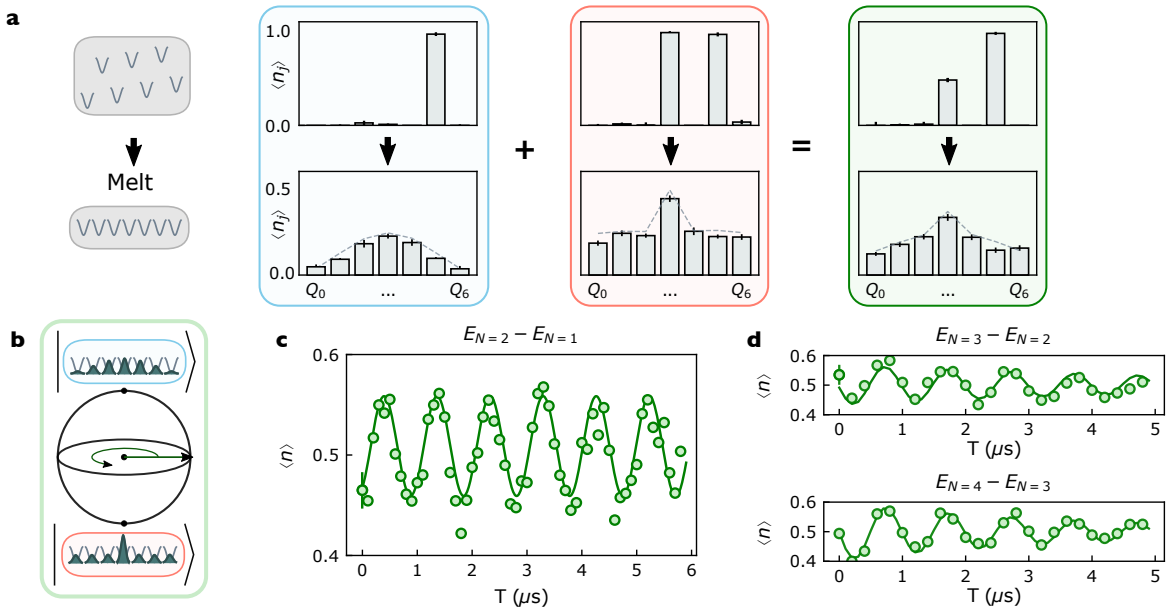

Figure 6.2: **Benchmarking the Manybody Ramsey Protocol**. **a,** To explore this protocol in the lab, we deterministically inject particles into a disordered lattice & remove the disorder (left), before imaging the resulting density distribution. When we inject precisely 1 photon (upper blue panel), adiabatic disorder removal produces the lowest-momentum particle-in-a-box state (lower blue panel); injecting two photons (upper red panel) produces the lowest energy two-body state after disorder is removed (lower red panel). If we deterministically inject the first particle with a π pulse but $\frac{\pi}{2}$ pulse the second photon, we should produce the manybody superposition state, and indeed we observe the average of the two density distributions (green panels). **b,** To demonstrate that this average density distribution corresponds to the macroscopic superposition of manybody states, we allow the superposition state to evolve on the Bloch sphere before adiabatically mapping the manybody superposition back onto a single qubit, where it can be read out via a second $\frac{\pi}{2}$ pulse. **c,** The resulting Ramsey fringe (vs hold time T in the manybody superposition state) evolves with a frequency given by the energy difference between the manybody states minus the frequency of the local oscillator from which the $\frac{\pi}{2}$ pulses are derived, exhibiting contrast over several microseconds limited by the single-qubit T_2 (see SI C.2). In **d,** we demonstrate the applicability of the approach to larger systems by applying it to superpositions of $N = 2, 3$ and $N = 3, 4$ particle fluids; the increased decay reflects the faster dephasing of states with more particles. Representative error bars (on first data point of each plot) reflect the S.E.M. This figure is adapted from Ref. [121].

disorder to re-localize the phase information into a single lattice site (qubit) and finally applying a $\frac{\pi}{2}$ pulse to interfere the states & read out the encoded phase in the occupation basis. The resulting sinusoidal Ramsey fringe (occupation vs T) is shown in Fig. 6.2c, with contrast limited by qubit dephasing (see SI C.2). The fringe frequency of 10 MHz is translated down (for clarity) from the actual energy difference of 5.317 GHz via a T-dependent phase offset of the second $\frac{\pi}{2}$ pulse (see SI B.1). Similar experiments enable single-qubit measurement of energy differences of 2/3 & 3/4 particle superposition states (Fig. 6.2d), with minimal contrast reduction, and only a small drop in coherence time. We are thus prepared to apply the protocol to exploration of manybody physics.

6.4 Probing the Excitation Spectrum

Our manybody Ramsey protocol relies upon our ability to adiabatically assemble and disassemble highly entangled states. If the state assembly is non-adiabatic, we imperfectly prepare the target states of our quantum fluid; if the disassembly is non-adiabatic then we imperfectly map them back to the initial qubits. One might expect that such non-adiabaticity would simply reduce the contrast of the resulting manybody Ramsey fringe, but the reality is more subtle: to the extent that the non-adiabaticity is minimal, only a small amount of population is transferred out of the instantaneous eigenstates during assembly, of which some fraction is transferred back during disassembly (see Fig. 6.3a). This has the effect of adding new frequency components to the Ramsey fringe that provide information about the excitation spectrum of the manybody system.

We investigate this phenomenon in Figure 6.3b-d by varying the length τ of our adiabatic assembly and disassembly ramps. In Fig. 6.3b, we plot the Fourier transform of the Ramsey fringe for the slowest (upper) and fastest (lower) ramps: When the ramp is slow compared with manybody gaps ($\tau = 1\mu s \gg J^{-1}$), we observe a single frequency component in the Ramsey spectrum indicating preparation of a superposition of only a single pair of states.

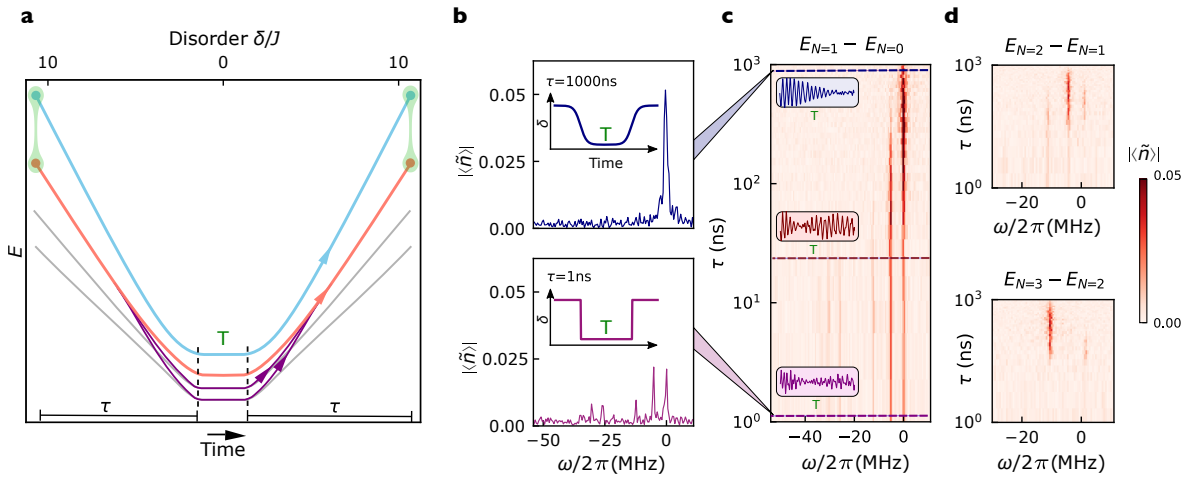

Figure 6.3: **Spectroscopic Signatures of Adiabaticity**. The manybody Ramsey protocol relies critically on the ability to adiabatically map localized states into and out of highly entangled states (in a ramp time τ). **a,** Ramping too quickly leads to diabatic excitations (purple) into other manybody states that do not interfere with the states (red/blue) in the prepared superposition (green) and thus reduce Ramsey fringe contrast. With some probability, however, these diabatic excitations are diabatically de-excited back into the initial state (red) during the backwards ramp; because these excitations evolve at different frequencies (corresponding to their energies) during the hold time T, they produce Ramsey fringes at other Fourier frequencies. **b,** For the slowest ramp ($\tau = 1$ µs) there are no diabatic excitations, producing a single Fourier feature in the Ramsey interference between $N = 0$ and $N = 1$ eigenstates. **c** For the fastest ramp ($\tau = 1$ ns), the many diabatic excitations are reflected in additional frequencies in the Ramsey fringe beyond the dominant feature in the slow ramp. **c,** As the ramp time τ is varied over three decades, frequency components furthest from the dominant feature disappear first, with the low-offset-frequency features disappearing only for the slowest ramps, consistent with excitation rates controlled by the energy gaps of the fluid. **Insets** depict the time-domain Ramsey fringes for slow, intermediate, and fast ramps (top to bottom). **d,** Repeating these experiments with superpositions of $N = 1, 2$ and $N = 2, 3$ particles demonstrates that while the proliferation of manybody states makes resolving diabatic excitations challenging, the dominant feature nonetheless appears for the slowest ramps. This figure is adapted from Ref. [121].

When the ramp is fast ($\tau = 1\text{ns} \ll J^{-1}$), we observe numerous frequency components in the Ramsey spectrum indicating that we have prepared numerous pairs of states that then interfere. In Fig. 6.3c we plot the Fourier spectrum as we tune the ramp time τ over three decades, observing the appearance of increasing numbers of peaks as the ramp gets faster. Repeating this experiment with more particles (Figure 6.3d) reveals fewer total peaks, despite the larger state space accessible with more particles. This occurs because the number of accessible states grows so rapidly that for all but the slowest ramps the features overlap and smear into a continuum.

In practice, achieving the best spectroscopic resolution for the Ramsey signal frequency is a balancing act between: (i) particle loss/dephasing if the protocol takes too long compared to the photon T_1/T_2 (see SI C.2) and (ii) reduction in the spectral weight of the correct Fourier peak if the adiabatic ramp time τ is too small and the wrong manybody states are prepared. In order to circumvent decoherence in larger systems, we choose faster ramps that induce some diabatic excitation without obscuring the correct Fourier feature.

6.5 Extracting Thermodynamic Observables

Having demonstrated the ability to interferometrically extract the energy difference of arbitrarily chosen manybody states, we now apply the technique to the measurement of thermodynamic observables of a quantum fluid. To do this we rely upon the fact that thermodynamic quantities like the chemical potential and the pressure may be understood as the rate of change of the system energy with density, and thus particle number, a quantity which our manybody interferometry technique probes directly.

The chemical potential is the energy required to add a particle to the manybody system at fixed system size V, $\mu = E_{N+1,V} - E_{N,V} \approx \frac{\partial E}{\partial N}\Big|^V$: we thus measure μ by performing manybody Ramsey interferometry between the N and $N+1$ particle ground states. In Fig. 6.4a we demonstrate this measurement for the superposition of $N = 1$ and $N = 2$ parti-

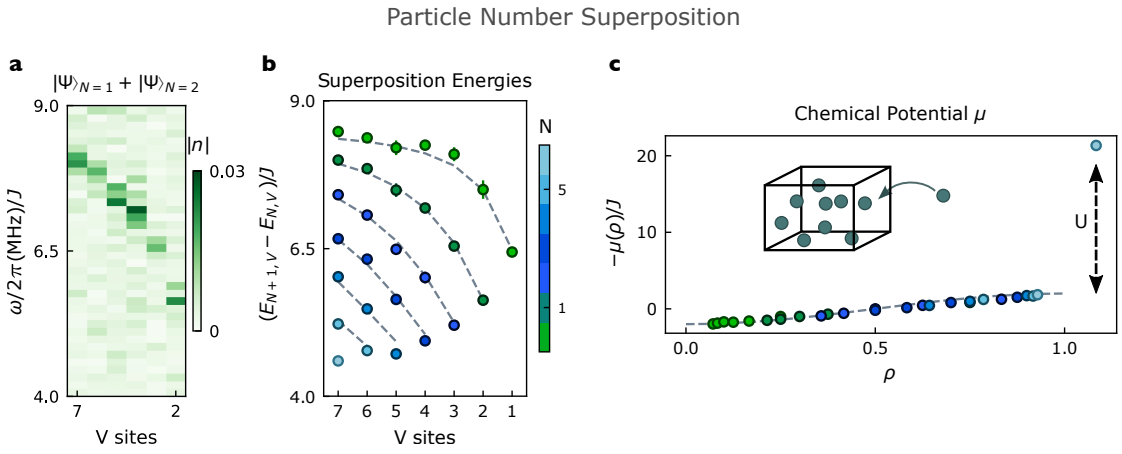

Figure 6.4: **Spectroscopic Probes of Thermodynamics**. Manybody Ramsey interferometry offers new ways to characterize synthetic quantum matter: **a...c,** The chemical potential $\mu = E_{N+1,V} - E_{N,V}$ quantifies the energy required to add a particle to a manybody system, and we measure it by interfering states of different particle number. **a** is a sample dataset showing the Ramsey spectrum for the superposition of $N = 1, 2$ particles as we vary the total system size V. For each V, the chemical potential μ is assigned to the frequency of maximal spectral density, which we plot in **b** for all fillings up to unit filling $N = 0...V - 1$, and all system sizes $V = 1...7$. In **c** we replot all data vs the density $\rho \equiv N/V$, finding a collapse onto a universal sinusoidal form (gray) consistent with a free-fermion model [66]. Error bars, where larger than the data-point, reflect the S.E.M. (see SI B.8). This figure is adapted from Ref. [121].

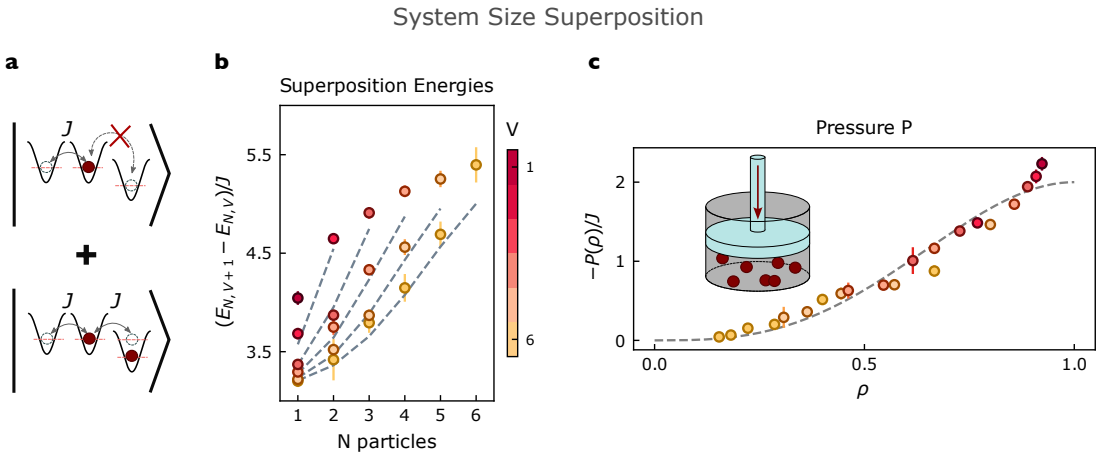

Figure 6.5: **Spectroscopic Probes of Thermodynamics**. The pressure $P = E_{N,V+1} - E_{N,V}$ quantifies the energy required to change the system size, and we measure it by interfering states of different system size. We achieve controlled superpositions of system sizes using the approach shown in **d**: the controlling site is U-detuned such that when it is empty, it is energetically inaccessible, reducing the system size by a single site; when it is filled, it becomes accessible and accordingly increases the system size. Using this site as the control in a manybody Ramsey experiment allows us to extract the energy difference between N particles melted into $V + 1$ vs V sites (see SI B.2). Performing this protocol for different volumes V and particle numbers N produces the raw data in **e**, which we rescale vs density in **f**, again finding agreement with a free-fermion theory. Error bars, where larger than the data-point, reflect the S.E.M. (see SI B.8). This figure is adapted from Ref. [121].

cles as we vary the number of accessible sites V. At each V, the Fourier frequency with the largest oscillation amplitude corresponds to the chemical potential. In Fig. 6.4b we plot this chemical potential vs. V, repeating the measurements for particle numbers from an empty system $N = 0$ to a filled system $N = V - 1$. In Fig. 6.4c we replot the data versus the density $\rho \equiv \frac{N}{V}$, finding collapse onto a universal (intensive) form $\mu = -2J\cos(\pi\rho)$: adding particles reduces the volume available to each particle, increasing the uncertainty-induced kinetic energy required to add it to the system. These data are consistent with a free-fermion model (see Sec 2.4) [66, 67] modulo small system-size corrections (see Sec 2.4.2, B.3.1). Beyond unit filling we observe an additional energy cost U per particle reflecting the incompressibility of the unit-filled Mott-insulating state [66].

The pressure is the force required to maintain the fluid at fixed size, or equivalently the

energy required to reduce the system size $P = E_{N,V} - E_{N,V+1} \approx -\frac{\partial E}{\partial V}\Big|^{N}$. To directly measure the pressure we thus need to perform manybody interferometry between systems of different sizes rather than different particle numbers. We achieve this by engineering our ancilla qubit to control the system size: as shown in Figure 6.5a, the ancilla site is detuned in energy by U, ensuring that when it is empty particles cannot tunnel onto it (reducing the system size by 1 site), and when it is occupied particles can tunnel. (Bose-enhanced tunneling onto the occupied ancilla is compensated by Floquet engineering, see SI B.2). The measured pressures for all particle numbers and system sizes are shown in Fig. 6.5b. They are replotted vs density in Fig. 6.5c, demonstrating that higher densities lead to more uncertainty pressure, again in agreement with a free fermion model anticipated to describe the 1D hardcore bosons in our experiments(See sec 2.3).

6.6 Conclusion

We have introduced a probe of synthetic quantum matter that accesses new observables by blurring the boundary between state preparation and measurement. Rather than first preparing a manybody state and then characterizing it, we instead control what manybody state we prepare with an ancilla qubit, coherently *reverse* the preparation procedure to disentangle the ancilla from the manybody system, and sandwich this process within an ancilla Ramsey sequence. This manybody Ramsey interferometry protocol enables direct measurement of energy differences of different eigenstates of the same system, as well as the same eigenstate of different systems. We employ it to directly extract thermodynamic properties of a quantum fluid.

Because the manybody Ramsey protocol relies upon reversible adiabatic assembly of manybody states [97], it requires only a small factor more coherence time than adiabatic state preparation. In other words, if you can build a state, you can characterize it with manybody Ramsey interferometry.

Marrying these techniques with recent advances in topological quantum matter [23] will enable probes of fractional statistics [113]; applying the techniques to glassy [144, 145] or time-crystalline [26, 27] phases has the potential to shed light on their structure. We anticipate opportunities to apply manybody Ramsey interferometry to cold atoms, particularly in topological [128] or fermionic sectors [35]. Marrying this tool with a quantum Fourier transform suggests yet more efficient approaches to quantum sensing in manybody systems [120]. More broadly, this work invites the question: what observables become accessible when *multiple* ancillas are entangled with, and then disentangled from, a quantum material? We envision a future where hitherto unimagined observables are probed by entangling quantum matter with small quantum computers.

CHAPTER 7

OUTLOOK

Using microwave photons in superconducting circuits, we have built a device whose physics is described by the 1D Bose-Hubbard model in the hardcore boson limit. In the first experiment described in this thesis in Chapter 5, we harnessed controlled disorder for state preparation, enabling the creation of compressible fluid states previously inaccessible with circuit QED tools. We started with a disordered lattice where all eigenstates were localized, and prepared desired eigenstates by injecting photons into individual sites. We then adiabatically removed the disorder, melting the system into the target many-body state. We characterised the resulting eigenstates' density profiles, entanglement, and correlation functions, capturing Friedel oscillations as direct microscopic evidence that the photons had fermionized.

The adiabatic disorder-tuning state preparation technique naturally lends itself to assembling superpositions of strongly interacting fluid states, explored in Chapter 6. In this experiment, we adiabatically prepared ancilla-controlled superpositions of strongly interacting fluids, evolved them to acquire a phase difference, and relocalized the interference phase into the ancilla for efficient measurement. Using this approach, we measured the coherence between pairs of manybody states, varied the adiabatic ramp speed to characterize how information spreads across the system, and extracted thermodynamic observables such as chemical potential and pressure. This procedure literally entangles state preparation and measurement, enabling low density, high signal-to-noise probes of complex manybody systems. The techniques demonstrated in this experiment apply equally well to other platforms with single-site control and adiabatic preparation capabilities such as cold atoms and ions.

The overall theme of this thesis has been demonstrating the strength of superconducting circuits as a platform to explore creative and powerful new methods of state preparation and characterization. There are a number of exciting future directions the project could take continuing along these themes! At the time of writing, there is another paper in preparation

by Andrei Vrajitoarea (postdoc on the project, now faculty at NYU!) using this device to probe transport and low-energy excitations (phonons) of these strongly interacting fluids, and combine manybody driving techniques with an ancilla qubit to prepare NOON states. Another possible direction would be to use sideband cooling to stabilize the lowest energy fluid states within a given particle manifold, demonstrating the use of reservoir engineering for a highly entangled manybody state (past work along this idea in Ref. [33]). We could also couple one frequency-tunable ancilla qubit to a large interconnected graph of fixed frequency qubits, and use the ancilla to adiabatically load the larger qubit system with particles as well as spectroscopically interrogate it. This experiment would explore the limits of extracting global manybody properties with simple single-qubit measurements, and showcase that control and measurement overhead need not to scale with system size.

It's an exciting time for quantum simulation! As platforms mature, new prospects abound for programming interesting Hamiltonians and exploring open questions in manybody physics from a ground-up microscopic approach. I await the results of the coming years with great interest, and hope this work helps illustrate the fascinating possibilities offered by experiments in building and measuring synthetic quantum matter. Whether you are a veteran quantum simulationist, a newcomer, or merely an interested reader, thank you for reading and retracing with me the adventures of my PhD! May your interactions be strong and your particles long-lived. Cheers!

REFERENCES

1. Daley, A. J. *et al.* Practical Quantum Advantage in Quantum Simulation. *Nature* **607,** 667–676 (2022).

2. Choi, J.-y. *et al.* Exploring the Many-Body Localization Transition in Two Dimensions. *Science* **352,** 1547–1552 (2016).

3. Chiu, C. S. *et al.* String Patterns in the Doped Hubbard Model. *Science* **365,** 251–256 (2019).

4. Feynman, R. P. Simulating Physics with Computers. *Int J Theor Phys* **21,** 467–488 (1982).

5. Cirac, J. I. & Zoller, P. Goals and Opportunities in Quantum Simulation. *Nature Phys* **8,** 264–266 (2012).

6. Lloyd, S. Universal Quantum Simulators. *Science* **273,** 1073–1078 (1996).

7. Nielsen, M. A. & Chuang, I. L. *Quantum Computation and Quantum Information: 10th Anniversary Edition* ISBN: 9780511976667 (2010).

8. Montanaro, A. Quantum Algorithms: An Overview. *npj Quantum Inf* **2,** 1–8 (2016).

9. Suzuki, M. Generalized Trotter's Formula and Systematic Approximants of Exponential Operators and Inner Derivations with Applications to Many-Body Problems. *Commun.Math. Phys.* **51,** 183–190 (1976).

10. Devitt, S. J., Munro, W. J. & Nemoto, K. Quantum Error Correction for Beginners. *Rep. Prog. Phys.* **76,** 076001 (2013).

11. Laflamme, R., Miquel, C., Paz, J. P. & Zurek, W. H. Perfect Quantum Error Correcting Code. *Phys. Rev. Lett.* **77,** 198–201 (1996).

12. Ofek, N. *et al.* Extending the Lifetime of a Quantum Bit with Error Correction in Superconducting Circuits. *Nature* **536,** 441–445 (2016).

13. Preskill, J. Quantum Computing in the NISQ Era and Beyond. *Quantum* **2,** 79 (2018).

14. Fan, R., Zhang, P., Shen, H. & Zhai, H. Out-of-Time-Order Correlation for Many-Body Localization. *Science Bulletin* **62,** 707–711 (2017).

15. Roushan, P. *et al.* Spectroscopic Signatures of Localization with Interacting Photons in Superconducting Qubits. *Science* **358,** 1175–1179 (2017).

16. Karamlou, A. H. *et al.* Quantum Transport and Localization in 1d and 2d Tight-Binding Lattices. *npj Quantum Inf* **8,** 1–8 (2022).

17. Mazurenko, A. *et al.* A Cold-Atom Fermi–Hubbard Antiferromagnet. *Nature* **545,** 462–466 (2017).

18. Hilker, T. A. *et al.* Revealing Hidden Antiferromagnetic Correlations in Doped Hubbard Chains via String Correlators. *Science* **357,** 484–487 (2017).

19. Koepsell, J. *et al.* Imaging Magnetic Polarons in the Doped Fermi–Hubbard Model. *Nature* **572,** 358–362 (2019).

20. Semeghini, G. *et al.* Probing Topological Spin Liquids on a Programmable Quantum Simulator. *Science* **374,** 1242–1247 (2021).

21. Satzinger, K. J. *et al.* Realizing Topologically Ordered States on a Quantum Processor. *Science* **374,** 1237–1241 (2021).

22. Clark, L. W., Schine, N., Baum, C., Jia, N. & Simon, J. Observation of Laughlin States Made of Light. *Nature* **582,** 41–45 (2020).

23. Owens, J. C. *et al.* Chiral Cavity Quantum Electrodynamics. *Nat. Phys.* **18,** 1048–1052 (2022).

24. Ozawa, T. *et al.* Topological Photonics. *Rev. Mod. Phys.* **91,** 015006 (2019).

25. Cooper, N. R., Dalibard, J. & Spielman, I. B. Topological Bands for Ultracold Atoms. *Rev. Mod. Phys.* **91,** 015005 (2019).

26. Zhang, J. *et al.* Observation of a Discrete Time Crystal. *Nature* **543,** 217–220 (2017).

27. Choi, S. *et al.* Observation of Discrete Time-Crystalline Order in a Disordered Dipolar Many-Body System. *Nature* **543,** 221–225 (2017).

28. Bluvstein, D. *et al.* Controlling Quantum Many-Body Dynamics in Driven Rydberg Atom Arrays. *Science* **371,** 1355–1359 (2021).

29. Choi, S., Bao, Y., Qi, X.-L. & Altman, E. Quantum Error Correction in Scrambling Dynamics and Measurement-Induced Phase Transition. *Phys. Rev. Lett.* **125,** 030505 (2020).

30. Barreiro, J. T. *et al.* An Open-System Quantum Simulator with Trapped Ions. *Nature* **470,** 486–491 (2011).

31. Ma, R. *et al.* A Dissipatively Stabilized Mott Insulator of Photons. *Nature* **566,** 51–57 (2019).

32. Mirhosseini, M. *et al.* Cavity Quantum Electrodynamics with Atom-like Mirrors. *Nature* **569,** 692–697 (2019).

33. Hacohen-Gourgy, S., Ramasesh, V. V., De Grandi, C., Siddiqi, I. & Girvin, S. M. Cooling and Autonomous Feedback in a Bose-Hubbard Chain with Attractive Interactions. *Phys. Rev. Lett.* **115,** 240501 (2015).

34. Monroe, C. *et al.* Programmable Quantum Simulations of Spin Systems with Trapped Ions. *Rev. Mod. Phys.* **93,** 025001 (2021).

35. Chiu, C. S., Ji, G., Mazurenko, A., Greif, D. & Greiner, M. Quantum State Engineering of a Hubbard System with Ultracold Fermions. *Phys. Rev. Lett.* **120,** 243201 (2018).

36. Ebadi, S. *et al.* Quantum Phases of Matter on a 256-Atom Programmable Quantum Simulator. *Nature* **595,** 227–232 (2021).

37. Zhang, X., Kim, E., Mark, D. K., Choi, S. & Painter, O. A Superconducting Quantum Simulator Based on a Photonic-Bandgap Metamaterial. *Science* **379,** 278–283 (2023).

38. Carusotto, I. *et al.* Photonic Materials in Circuit Quantum Electrodynamics. *Nat. Phys.* **16,** 268–279 (2020).

39. Kollár, A. J., Fitzpatrick, M. & Houck, A. A. Hyperbolic Lattices in Circuit Quantum Electrodynamics. *Nature* **571,** 45–50 (2019).

40. Vrajitoarea, A. *et al. Ultrastrong Light-Matter Interaction in a Photonic Crystal* 2022. arXiv: 2209.14972 [cond-mat, physics:quant-ph].

41. Bloch, I., Dalibard, J. & Nascimbène, S. Quantum Simulations with Ultracold Quantum Gases. *Nature Phys* **8,** 267–276 (2012).

42. Gross, C. & Bloch, I. Quantum Simulations with Ultracold Atoms in Optical Lattices. *Science* **357,** 995–1001 (2017).

43. Greiner, M., Mandel, O., Esslinger, T., Hänsch, T. W. & Bloch, I. Quantum Phase Transition from a Superfluid to a Mott Insulator in a Gas of Ultracold Atoms. *Nature* **415,** 39–44 (2002).

44. Browaeys, A. & Lahaye, T. Many-Body Physics with Individually Controlled Rydberg Atoms. *Nat. Phys.* **16,** 132–142 (2020).

45. Bohn, J. L., Rey, A. M. & Ye, J. Cold Molecules: Progress in Quantum Engineering of Chemistry and Quantum Matter. *Science* **357,** 1002–1010 (2017).

46. Blatt, R. & Roos, C. F. Quantum Simulations with Trapped Ions. *Nature Phys* **8,** 277–284 (2012).

47. Aspuru-Guzik, A. & Walther, P. Photonic Quantum Simulators. *Nature Phys* **8,** 285–291 (2012).

48. Houck, A. A., Türeci, H. E. & Koch, J. On-Chip Quantum Simulation with Superconducting Circuits. *Nature Phys* **8,** 292–299 (2012).

49. Brooks, M. *IBM Wants to Build a 100,000-Qubit Quantum Computer* 2023.

50. Acharya, R. *et al.* Suppressing Quantum Errors by Scaling a Surface Code Logical Qubit. *Nature* **614,** 676–681 (2023).

51. Roushan, P. *et al.* Chiral Ground-State Currents of Interacting Photons in a Synthetic Magnetic Field. *Nature Phys* **13,** 146–151 (2017).

52. Fisher, M. P. A., Weichman, P. B., Grinstein, G. & Fisher, D. S. Boson Localization and the Superfluid-Insulator Transition. *Phys. Rev. B* **40,** 546–570 (1989).

53. Koch, J. *et al.* Charge-Insensitive Qubit Design Derived from the Cooper Pair Box. *Phys. Rev. A* **76,** 042319 (2007).

54. Morvan, A. *et al.* Formation of Robust Bound States of Interacting Microwave Photons. *Nature* **612,** 240–245 (2022).

55. Yan, Z. *et al.* Strongly Correlated Quantum Walks with a 12-Qubit Superconducting Processor. *Science* **364,** 753–756 (2019).

56. Ejima, S. *et al.* Characterization of Mott-Insulating and Superfluid Phases in the One-Dimensional Bose-Hubbard Model. *Phys. Rev. A* **85,** 053644 (2012).

57. Gemelke, N., Zhang, X., Hung, C.-L. & Chin, C. In Situ Observation of Incompressible Mott-Insulating Domains in Ultracold Atomic Gases. *Nature* **460,** 995–998 (2009).

58. Léonard, J. *et al.* Realization of a Fractional Quantum Hall State with Ultracold Atoms. *Nature* **619,** 495–499 (2023).

59. Jaksch, D., Bruder, C., Cirac, J. I., Gardiner, C. W. & Zoller, P. Cold Bosonic Atoms in Optical Lattices. *Phys. Rev. Lett.* **81,** 3108–3111 (1998).

60. Krantz, P. *et al.* A Quantum Engineer's Guide to Superconducting Qubits. *Applied Physics Reviews* **6,** 021318 (2019).

61. Blais, A., Grimsmo, A. L., Girvin, S. M. & Wallraff, A. Circuit Quantum Electrodynamics. *Rev. Mod. Phys.* **93,** 025005 (2021).

62. Meinert, F., Mark, M. J., Lauber, K., Daley, A. J. & Nägerl, H.-C. Floquet Engineering of Correlated Tunneling in the Bose-Hubbard Model with Ultracold Atoms. *Phys. Rev. Lett.* **116,** 205301 (2016).

63. Yan, F. *et al.* Tunable Coupling Scheme for Implementing High-Fidelity Two-Qubit Gates. *Phys. Rev. Appl.* **10,** 054062 (2018).

64. Paredes, B. *et al.* Tonks–Girardeau Gas of Ultracold Atoms in an Optical Lattice. *Nature* **429,** 277–281 (2004).

65. Kinoshita, T., Wenger, T. & Weiss, D. S. Observation of a One-Dimensional Tonks-Girardeau Gas. *Science* **305,** 1125–1128 (2004).

66. Cazalilla, M. A., Citro, R., Giamarchi, T., Orignac, E. & Rigol, M. One Dimensional Bosons: From Condensed Matter Systems to Ultracold Gases. *Rev. Mod. Phys.* **83,** 1405–1466 (2011).

67. Girardeau, M. Relationship between Systems of Impenetrable Bosons and Fermions in One Dimension. *Journal of Mathematical Physics* **1,** 516–523 (1960).

68. Jordan, P. & Wigner, E. Über das Paulische Äquivalenzverbot. *Z. Physik* **47,** 631–651 (1928).

69. Bethe, H. Zur Theorie der Metalle. *Z. Physik* **71,** 205–226 (1931).

70. Lieb, E. H. & Liniger, W. Exact Analysis of an Interacting Bose Gas. I. The General Solution and the Ground State. *Phys. Rev.* **130,** 1605–1616 (1963).

71. Lieb, E. H. Exact Analysis of an Interacting Bose Gas. II. The Excitation Spectrum. *Phys. Rev.* **130,** 1616–1624 (1963).

72. Mattis, D. C. & Lieb, E. H. Exact Solution of a Many-Fermion System and Its Associated Boson Field. *Journal of Mathematical Physics* **6,** 304–312 (2004).

73. Cazalilla, M. A. Differences between the Tonks Regimes in the Continuum and on the Lattice. *Phys. Rev. A* **70,** 041604 (2004).

74. Bijl, A. The Lowest Wave Function of the Symmetrical Many Particles System. *Physica* **7,** 869–886 (1940).

75. Reatto, L. & Chester, G. V. Phonons and the Properties of a Bose System. *Phys. Rev.* **155,** 88–100 (1967).

76. Cazalilla, M. A. Bosonizing One-Dimensional Cold Atomic Gases. *J. Phys. B: At. Mol. Opt. Phys.* **37,** S1 (2004).

77. Saxberg, B. *Creating Compressible Many-Body States of Light through Adiabatic Tuning of Disorder* PhD thesis (The University of Chicago, 2023).

78. Schuster, D. I. *Circuit Quantum Electrodynamics* PhD thesis (Yale University, 2007).

79. Heinsoo, J. *et al.* Rapid High-Fidelity Multiplexed Readout of Superconducting Qubits. *Phys. Rev. Appl.* **10,** 034040 (2018).

80. Naghiloo, M. *Exploring Quantum Dynamics and Thermodynamics in Superconducting Qubits* PhD thesis (2019).

81. Karamlou, A. H. *Quantum Simulation of Many-Body Systems with Superconducting Qubits* Thesis (Massachusetts Institute of Technology, 2023).

82. Wang, H. *et al.* Cryogenic Single-Port Calibration for Superconducting Microwave Resonator Measurements. *Quantum Sci. Technol.* **6,** 035015 (2021).

83. Barrett, C. N. *et al.* Learning-Based Calibration of Flux Crosstalk in Transmon Qubit Arrays. *Phys. Rev. Appl.* **20,** 024070 (2023).

84. Sete, E. A., Martinis, J. M. & Korotkov, A. N. Quantum Theory of a Bandpass Purcell Filter for Qubit Readout. *Phys. Rev. A* **92,** 012325 (2015).

85. Lévesque, L. Nyquist Sampling Theorem: Understanding the Illusion of a Spinning Wheel Captured with a Video Camera. *Phys. Educ.* **49,** 697 (2014).

86. Johnson, B. R. *Controlling Photons in Superconducting Electrical Circuits* PhD thesis (Yale University, 2011).

87. Rol, M. A. *et al.* Time-Domain Characterization and Correction of on-Chip Distortion of Control Pulses in a Quantum Processor. *Applied Physics Letters* **116,** 054001 (2020).

88. Pezzè, L., Smerzi, A., Oberthaler, M. K., Schmied, R. & Treutlein, P. Quantum Metrology with Nonclassical States of Atomic Ensembles. *Rev. Mod. Phys.* **90,** 035005 (2018).

89. Grusdt, F., Letscher, F., Hafezi, M. & Fleischhauer, M. Topological Growing of Laughlin States in Synthetic Gauge Fields. *Phys. Rev. Lett.* **113,** 155301 (2014).

90. Dallaire-Demers, P.-L., Romero, J., Veis, L., Sim, S. & Aspuru-Guzik, A. Low-Depth Circuit Ansatz for Preparing Correlated Fermionic States on a Quantum Computer. *Quantum Sci. Technol.* **4,** 045005 (2019).

91. Kapit, E., Hafezi, M. & Simon, S. H. Induced Self-Stabilization in Fractional Quantum Hall States of Light. *Phys. Rev. X* **4,** 031039 (2014).

92. Lebreuilly, J. *et al.* Stabilizing Strongly Correlated Photon Fluids with Non-Markovian Reservoirs. *Phys. Rev. A* **96,** 033828 (2017).

93. Albash, T. & Lidar, D. A. Adiabatic Quantum Computation. *Rev. Mod. Phys.* **90,** 015002 (2018).

94. Zurek, W. H., Dorner, U. & Zoller, P. Dynamics of a Quantum Phase Transition. *Phys. Rev. Lett.* **95,** 105701 (2005).

95. Tonks, L. The Complete Equation of State of One, Two and Three-Dimensional Gases of Hard Elastic Spheres. *Phys. Rev.* **50,** 955–963 (1936).

96. Goldman, N., Budich, J. C. & Zoller, P. Topological Quantum Matter with Ultracold Gases in Optical Lattices. *Nature Phys* **12,** 639–645 (2016).

97. Saxberg, B. *et al.* Disorder-Assisted Assembly of Strongly Correlated Fluids of Light. *Nature* **612,** 435–441 (2022).

98. Chen, Q., Stajic, J., Tan, S. & Levin, K. BCS–BEC Crossover: From High Temperature Superconductors to Ultracold Superfluids. *Physics Reports* **412,** 1–88 (2005).

99. Bakr, W. S., Gillen, J. I., Peng, A., Fölling, S. & Greiner, M. A Quantum Gas Microscope for Detecting Single Atoms in a Hubbard-Regime Optical Lattice. *Nature* **462,** 74–77 (2009).

100. Trotzky, S. *et al.* Time-Resolved Observation and Control of Superexchange Interactions with Ultracold Atoms in Optical Lattices. *Science* **319,** 295–299 (2008).

101. Islam, R. *et al.* Measuring Entanglement Entropy in a Quantum Many-Body System. *Nature* **528,** 77–83 (2015).

102. Brown, P. T. *et al.* Bad Metallic Transport in a Cold Atom Fermi-Hubbard System. *Science* **363,** 379–382 (2019).

103. McIver, J. W. *et al.* Light-Induced Anomalous Hall Effect in Graphene. *Nat. Phys.* **16,** 38–41 (2020).

104. Eisert, J., Friesdorf, M. & Gogolin, C. Quantum Many-Body Systems out of Equilibrium. *Nature Phys* **11,** 124–130 (2015).

105. Simon, J. *et al.* Quantum Simulation of Antiferromagnetic Spin Chains in an Optical Lattice. *Nature* **472,** 307–312 (2011).

106. Ma, R., Owens, C., Houck, A., Schuster, D. I. & Simon, J. Autonomous Stabilizer for Incompressible Photon Fluids and Solids. *Phys. Rev. A* **95,** 043811 (2017).

107. Bak, P. Commensurate Phases, Incommensurate Phases and the Devil's Staircase. *Rep. Prog. Phys.* **45,** 587 (1982).

108. Umucalılar, R. O., Simon, J. & Carusotto, I. Autonomous Stabilization of Photonic Laughlin States through Angular Momentum Potentials. *Phys. Rev. A* **104,** 023704 (2021).

109. Zhou, Y., Kanoda, K. & Ng, T.-K. Quantum Spin Liquid States. *Rev. Mod. Phys.* **89,** 025003 (2017).

110. Meyer, D. A. & Wallach, N. R. Global Entanglement in Multiparticle Systems. *Journal of Mathematical Physics* **43,** 4273–4278 (2002).

111. Chandran, A., Erez, A., Gubser, S. S. & Sondhi, S. L. Kibble-Zurek Problem: Universality and the Scaling Limit. *Phys. Rev. B* **86,** 064304 (2012).

112. Swingle, B., Bentsen, G., Schleier-Smith, M. & Hayden, P. Measuring the Scrambling of Quantum Information. *Phys. Rev. A* **94,** 040302 (2016).

113. Grusdt, F., Yao, N. Y., Abanin, D., Fleischhauer, M. & Demler, E. Interferometric Measurements of Many-Body Topological Invariants Using Mobile Impurities. *Nat Commun* **7,** 11994 (2016).

114. Manfra, M. J. Molecular Beam Epitaxy of Ultra-High-Quality AlGaAs/GaAs Heterostructures: Enabling Physics in Low-Dimensional Electronic Systems. *Annual Review of Condensed Matter Physics* **5,** 347–373 (2014).

115. Cao, Y. *et al.* Unconventional Superconductivity in Magic-Angle Graphene Superlattices. *Nature* **556,** 43–50 (2018).

116. Pagano, G. *et al.* Quantum Approximate Optimization of the Long-Range Ising Model with a Trapped-Ion Quantum Simulator. *Proceedings of the National Academy of Sciences* **117,** 25396–25401 (2020).

117. Braumüller, J. *et al.* Probing Quantum Information Propagation with Out-of-Time-Ordered Correlators. *Nat. Phys.* **18,** 172–178 (2022).

118. Landsman, K. A. *et al.* Verified Quantum Information Scrambling. *Nature* **567,** 61–65 (2019).

119. Mi, X. *et al.* Information Scrambling in Quantum Circuits. *Science* **374,** 1479–1483 (2021).

120. Vorobyov, V. *et al.* Quantum Fourier Transform for Nanoscale Quantum Sensing. *npj Quantum Inf* **7,** 1–8 (2021).

121. Roberts, G. *et al. Manybody Interferometry of Quantum Fluids* 2023. arXiv: 2309.05727 [cond-mat, physics:quant-ph].

122. Cheuk, L. W. *et al.* Quantum-Gas Microscope for Fermionic Atoms. *Phys. Rev. Lett.* **114,** 193001 (2015).

123. Wintersperger, K. *et al.* Realization of an Anomalous Floquet Topological System with Ultracold Atoms. *Nat. Phys.* **16,** 1058–1063 (2020).

124. Barbiero, L. *et al.* Coupling Ultracold Matter to Dynamical Gauge Fields in Optical Lattices: From Flux Attachment to Z2 Lattice Gauge Theories. *Science Advances* **5,** eaav7444 (2019).

125. Wineland, D. J. & Itano, W. M. Laser Cooling of Atoms. *Phys. Rev. A* **20,** 1521–1540 (1979).

126. Ketterle, W. & Druten, N. J. V. in *Advances In Atomic, Molecular, and Optical Physics* (eds Bederson, B. & Walther, H.) 181–236 (1996).

127. Poyatos, J. F., Cirac, J. I. & Zoller, P. Quantum Reservoir Engineering with Laser Cooled Trapped Ions. *Phys. Rev. Lett.* **77,** 4728–4731 (1996).

128. Léonard, J. *et al.* Realization of a Fractional Quantum Hall State with Ultracold Atoms. *Nature* **619,** 495–499 (2023).

129. Hafezi, M., Adhikari, P. & Taylor, J. M. Chemical Potential for Light by Parametric Coupling. *Phys. Rev. B* **92,** 174305 (2015).

130. Kurilovich, P., Kurilovich, V. D., Lebreuilly, J. & Girvin, S. M. Stabilizing the Laughlin State of Light: Dynamics of Hole Fractionalization. *SciPost Physics* **13,** 107 (2022).

131. He, Y.-C., Grusdt, F., Kaufman, A., Greiner, M. & Vishwanath, A. Realizing and Adiabatically Preparing Bosonic Integer and Fractional Quantum Hall States in Optical Lattices. *Phys. Rev. B* **96,** 201103 (2017).

132. Roos, C. F. *et al.* Control and Measurement of Three-Qubit Entangled States. *Science* **304,** 1478–1480 (2004).

133. Ketterle, W., Durfee, D. S. & Stamper-Kurn, D. M. *Making, Probing and Understanding Bose-Einstein Condensates* 1999. arXiv: cond-mat/9904034.

134. Greiner, M., Regal, C. A., Stewart, J. T. & Jin, D. S. Probing Pair-Correlated Fermionic Atoms through Correlations in Atom Shot Noise. *Phys. Rev. Lett.* **94,** 110401 (2005).

135. Yefsah, T., Desbuquois, R., Chomaz, L., Günter, K. J. & Dalibard, J. Exploring the Thermodynamics of a Two-Dimensional Bose Gas. *Phys. Rev. Lett.* **107,** 130401 (2011).

136. Ernst, P. T. *et al.* Probing Superfluids in Optical Lattices by Momentum-Resolved Bragg Spectroscopy. *Nature Phys* **6,** 56–61 (2010).

137. Shtanko, O. *et al. Uncovering Local Integrability in Quantum Many-Body Dynamics* 2023. arXiv: 2307.07552 [cond-mat, physics:quant-ph].

138. Monz, T. *et al.* 14-Qubit Entanglement: Creation and Coherence. *Phys. Rev. Lett.* **106,** 130506 (2011).

139. Huang, H.-Y., Kueng, R. & Preskill, J. Predicting Many Properties of a Quantum System from Very Few Measurements. *Nat. Phys.* **16,** 1050–1057 (2020).

140. Xu, K. *et al.* Probing Dynamical Phase Transitions with a Superconducting Quantum Simulator. *Science Advances* **6,** eaba4935 (2020).

141. Knap, M. *et al.* Probing Real-Space and Time-Resolved Correlation Functions with Many-Body Ramsey Interferometry. *Phys. Rev. Lett.* **111,** 147205 (2013).

142. Zeiher, J. *et al.* Many-Body Interferometry of a Rydberg-Dressed Spin Lattice. *Nature Phys* **12,** 1095–1099 (2016).

143. Ramsey, N. F. Experiments with Separated Oscillatory Fields and Hydrogen Masers. *Rev. Mod. Phys.* **62,** 541–552 (1990).

144. Dupuis, N. & Daviet, R. Bose-Glass Phase of a One-Dimensional Disordered Bose Fluid: Metastable States, Quantum Tunneling, and Droplets. *Phys. Rev. E* **101,** 042139 (2020).

145. Meldgin, C. *et al.* Probing the Bose Glass–Superfluid Transition Using Quantum Quenches of Disorder. *Nature Phys* **12,** 646–649 (2016).

146. Place, A. P. M. *et al.* New Material Platform for Superconducting Transmon Qubits with Coherence Times Exceeding 0.3 Milliseconds. *Nat Commun* **12,** 1779 (2021).

SUPPLEMENT A

SUPPLEMENT FOR CHAPTER 5

A.1 Extended Data

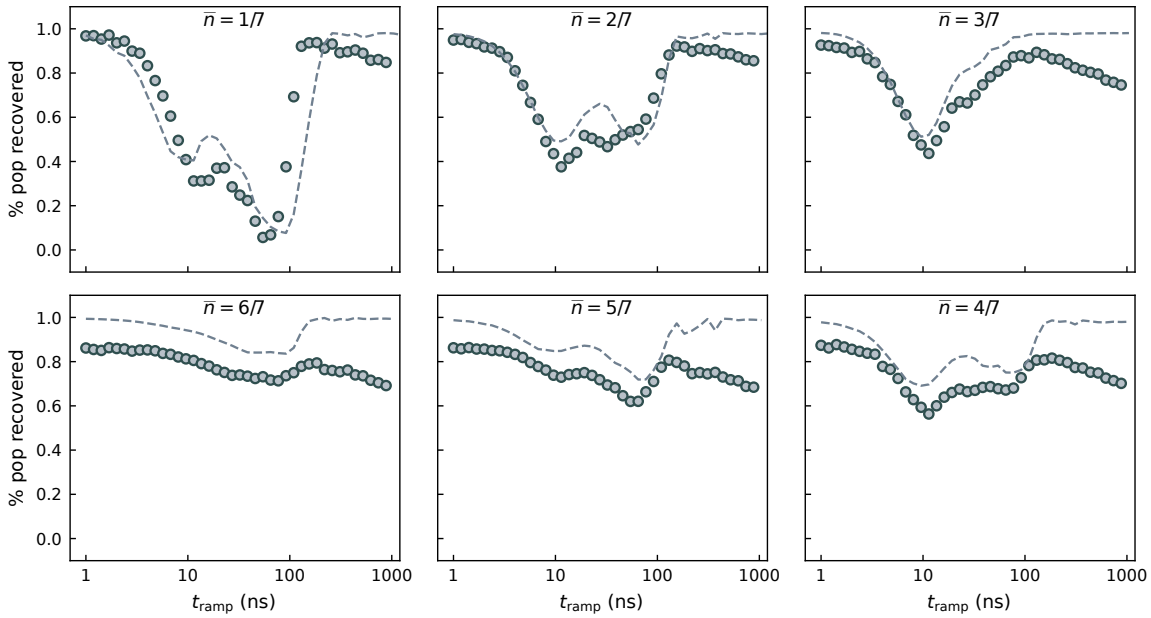

SI Fig. SA.1: **Adiabaticity Curves for All $\bar{n}$ Fillings.** Adiabaticity is given by the average number of photons that return to the originally excited sites as a function of ramp length. Here, we measure adiabiaticty curves for the highest energy eigenstate for all $\bar{n}$ fillings, revealing the minimum ramp length needed to be adiabatic when preparing these many-body states. As particle number increases, we start to suffer more from loss and no longer fully recover the initial starting population.

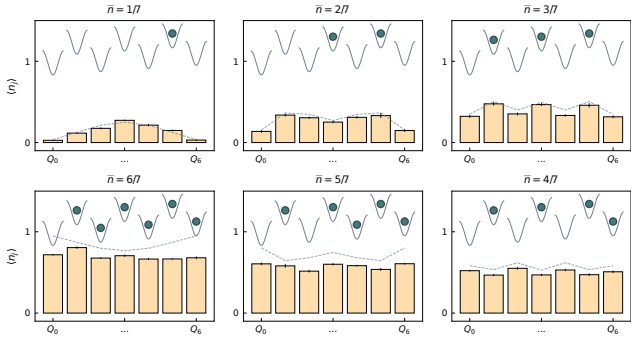

SI Fig. SA.2: **Profiles for $\bar{n}$ Fillings** Density profiles for the highest energy eigenstates, corresponding to fluid ground states, for filling $\bar{n}$=$\frac{1}{7}$ through $\frac{6}{7}$. For 5 and 6 particles, our results suffer from particle loss.

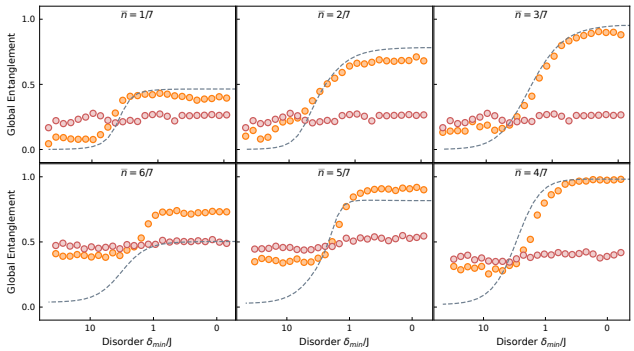

SI Fig. SA.3: **Entanglement for $\bar{n}$ Fillings** Data: Measure of Entanglement vs Disorder, for Filling $\bar{n}$=$\frac{1}{7}$ through $\frac{6}{7}$. Error bars reflect S.E.M.; here, they are smaller than markers.

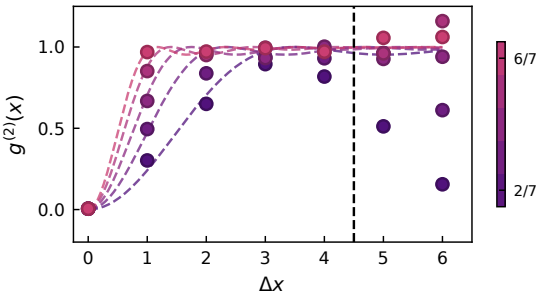

SI Fig. SA.4: $g^{(2)}(x)$ **for $\bar{n}$ Fillings** Measure of the two-body correlator $g^{(2)}(x)$ for all lattice spacings. In the main text, we only displayed results to the left of the black dashed line. Our results differ from infinite 1D TG theory due to finite size effects. The deviation from theory due to finite size is greater for larger "x" and lower particle fillings. We chose the cutoff for what to display in the main text at the "x" for which deviation is still small at all particle densities.

A.2 Pulse Sequences and Operating points

This experiment uses two kinds of frequency configurations for the qubits: one where the qubits are in a disordered stagger, and the other where the qubits are all degenerate. All our experiments involve tuning the qubits between these frequency configurations either diabatically or adiabatically depending on what the experiment requires.

In the disordered stagger, three qubits are above the lattice frequency and four qubits are below. The qubits are staggered in a zig-zag, so that neighbors are detuned by much greater than J. This configuration is useful for both readout and state preparation. Since eigenstates consist of localized particles and are well separated in energy, eigenstate preparation simply consists of applying a sequence of calibrated microwave π-pulses. Similarly in this disordered configuration, each readout resonator is only sensitive to the population of its individual qubit, enabling site-resolved readout.

There are two versions of the disordered (detuned) stagger used in this experiment. The first is the large disordered stagger (given in Table C.1), where neighboring qubits are spaced by $> U$ apart, and next-to-nearest-neighbors are spaced by $> 2J$. This stagger configuration is good for readout, but not for state preparation. At this lattice, we notice minimal readout crosstalk (values listed in Fig. 4.12). However, since the qubits are staggered with neighbors spaced by $> U$ (i.e. the $|2\rangle$ state of the upper qubits is above the $|1\rangle$ state of the lower qubits), the highest energy eigenstate for $N > 3$ particle prep involves prepping $|2\rangle$ states of the upper three qubits. This means that when ramping all the qubits to degeneracy, the ramp needs to be adiabatic both for the upper qubit $|2\rangle$ crossing the lower $|1\rangle$ as well as adiabatic when all the qubits approach degeneracy. Dealing with extra transitions is non-ideal, as it increases the ramp time needed to preserve adiabaticity.

In the second, smaller disordered stagger configuration, neighboring qubits are spaced by $\simeq \frac{U}{2}$ apart, and next-to-nearest-neighbors are spaced by $\sim 1.5J$. This stagger configuration is good for state preparation, but not good for readout. At this lattice, we measure more

significant readout crosstalk (more than 20% on at least four sites in any given configuration). However, eigenstates are still very localized, so preparing eigenstates still can be done with π-pulses. Further, ramping to degeneracy does not involved any $|2\rangle$ state crossings.

For all data in this experiment except for the entanglement vs disorder profiles, states were prepared in the small disordered stagger and read out in the large disordered stagger.

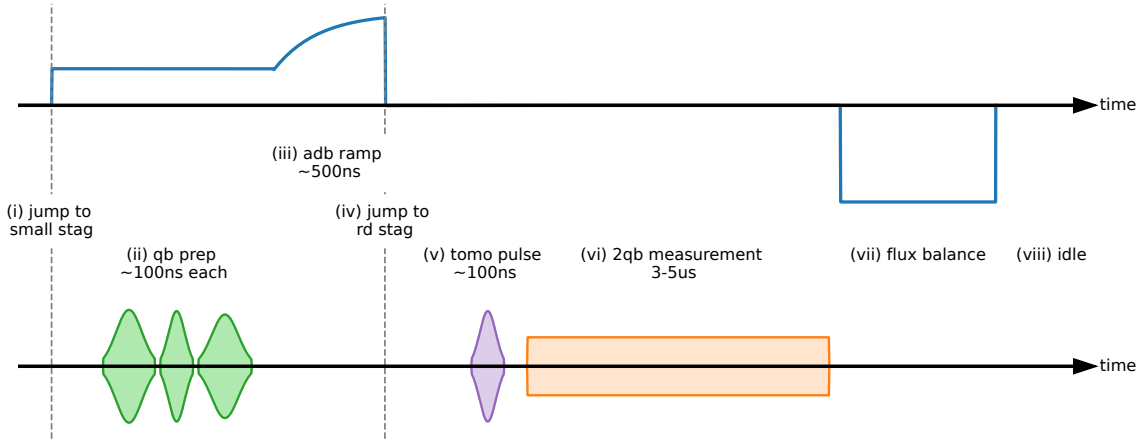

SI Fig. SA.5: **Pulse Sequence** All experiments begin with the qubits at the large disordered stagger. First (i), qubits are jumped to the small disordered stagger using RF flux (blue). Once the qubit frequencies settle, (ii) qubit preparation pulses are applied (green). Qubits are (iii) adiabatically ramped to degeneracy, then (iv) jumped back to the large stagger for single-site-resolved readout. (v) X90 and Y90 tomography gates (purple) are applied if the experiment involves full qubit tomography. (vi) a long readout pulse (orange) is applied to the resonator/s of the qubit/s being read out. Finally, (vii) a flux balancing pulse is applied to stop long timescale inductances from building up. The experiment idles so that the total experiment time is 500 μs to ensure all the qubits decay and are reset to the $|0\rangle$ state for the start of the next experiment.

A typical experiment pulse sequence is illustrated in Fig. SA.5. Before the start of an experiment, qubits are tuned to the large disordered stagger using DC flux bias. All microwave signals are off and the lattice is empty. During an experiment, qubit frequencies are controlled using the RF flux lines. At the start of an experiment, qubits are (i) diabatically "jumped" (i.e. rapidly tuned) to the small disordered stagger configuration for state preparation. After waiting 600ns to ensure the qubit frequencies are stable, (ii) π-pulses

are sequentially applied to several of the qubits. The qubits are (iii) adiabatically ramped to lattice degeneracy, adiabatically preparing the state of interest. After the qubits hit degeneracy/the state is prepared, (iv) the qubits are jumped to the large disordered stagger frequency configuration to freeze tunneling dynamics and onsite occupancy (or for reversibility experiments, ramped adiabatically back to the small stagger and then jumped to the large stagger for readout). After waiting 600 ns for qubits to settle, (v) X90 and Y90 pulses are applied if doing tomography. Then, (vi) a readout pulse is applied (or two readout pulses are applied simultaneously if doing correlation measurements). Finally, a flux-balancing pulse is applied so that the total experiment flux is zero, to avoid charging up any stray long-term inductances [86]. The experiment is repeated every 500 μs, leaving enough idle time between pulse sequences to ensure all the qubit excitations decay and are reset to the $|0\rangle$ state for the start of the next experiment.

We chose an exponential ramp shape for our adiabatic qubit ramp. The timing to preserve adiabaticity for different ramp shapes will obviously differ, but the exponential ramp simplifies the number of free variables to optimize over and captures the usual process of the many-body gap decreasing as more lattice sites approach resonance with one-another. For data in this paper, we found an exponential ramp of the form $e^{-t/\tau}$ gave good reversibility results (see Fig. 5.4) with $\tau = \frac{2}{5} \times t_{ramp}$. All qubit pulses are Gaussians truncated at $\pm 2\sigma$.

When the system is at the small disordered stagger configuration, placing an excitation in a qubit shifts the frequency of its neighbor by ~ 1 MHz. This is expected from theory, and occurs because of the proximity of the upper qubits' ω_{12} transition to the lower qubits' ω_{01} transition. We take these shifts into consideration by calibrating π-pulse amplitude and frequency depending on the order of qubit preparation.

For entanglement vs disorder profiles, we used different preparation methods in order to measure entanglement starting at greater disorders than the small stagger. For $N < 4$ entanglement vs disorder profiles (see SI SA.3), the qubits are prepped at the large stagger

and ramped to degeneracy directly from there. For $N \geq 4$ entanglement vs disorder profiles, qubits are prepped at the large stagger, all filled qubits are then jumped to lattice degeneracy, and the holes are ramped in. We do not use this method for $N > 3$ generally because we cannot jump filled qubits directly to the lattice fast enough to be fully diabatic, so we get a small but significant number of unwanted transitions (see Sec. 4.8.3).

A.3 Uncertainty Calculations

For each experiment, we measure 2000 shots, bin the shots, apply relevant confusion matrices, and extract the averaged quantity of interest (MB profile, entanglement, $g^{(2)}$, etc). We then repeat the experiment 10-11 times, and calculate the mean of the averages and standard deviation of the averages (i.e. calculate the standard error on the mean, or S.E.M.) for the values and error bars that we report in this chapter. The experiment repetitions are performed close in time (typically within a 10-30 min span) so that our error bars are not affected by slow experimental drift over hours or days.

SUPPLEMENT B

SUPPLEMENT FOR CHAPTER 6

B.1 Ramsey Interferometry Measurements

A Ramsey interferometry experiment on a single qubit measures that qubit's ω_{01} frequency (relative to the frequency of the tone used to drive the qubit). The experiment sequence is as follows. First, the qubit is driven into an equal superposition of $|0\rangle$ and $|1\rangle$ with a microwave $\pi/2$ pulse. The two states evolve relative to each other for time T with phase $\phi = \omega_{01}T$. A second $\pi/2$ pulse is applied, mapping oscillations around the equator of the Bloch sphere to population oscillations. The qubit population is read out, producing a fringe oscillating at $\omega_{01}T$ minus the frequency of the drive that the qubit is referenced to.

Manybody Ramsey works in a similar fashion. When measuring the energy difference of states with N vs $N-1$ particles when the qubits are all on resonance at the lattice frequency, the energy difference is approximately one lattice photon, 5.2 GHz. However, the qubit drive to which the energy difference is compared is at the frequency of the ancilla in the staggered position, on the order of hundreds of MHz detuned from the lattice frequency. The time resolution of our AWG is 1 ns; the maximum frequency we can physically record without aliasing is 500MHz; the maximum frequency we can comfortably measure is 250 MHz. In practice, we use a sampling rate of $3-4$ μs, which brings our maximum measurable frequency even lower. We thus add a time-dependent virtual phase to our second Ramsey $\pi/2$ pulse in order to virtually change the frequency of the qubit drive used as reference, bringing the measured oscillation frequency below the aliasing limit.

While measuring states with V vs $V-1$ sites, at first glance it seems like the energy differences involved should be within the same particle manifold. However, because of the way we measure volume superpositions (see SI B.2), the states we compare do differ by a particle, so we measure Ramsey oscillation as above.

To achieve appropriate frequency resolution for experiments involving examining Ramsey Fourier peaks, we record the Ramsey fringe for a minimum of $T = 800$ ns in steps of $3-4$ ns for a frequency resolution of at maximum 1.25 MHz (Fig. 6.3 2.7 µs, Fig. 6.4/Fig. 6.5 804ns). We choose our time resolution to balance experiment time (long experiments suffer more from frequency drift) and retaining the ability to distinguish frequencies we care about without encountering frequency aliasing.

B.2 Thermodynamic Observable Methods

B.2.1 Chemical Potential

To extract chemical potential, we compare the energy differences of states with N vs $N-1$ particles in a given volume V for a range of volumes and particle numbers by extracting the interference fringe between the relevant states. We compare highest energy eigenstates of each particle manifold, which map to the ground states of a repulsive-U model (see Sec. 2.4.1). Depending on the number of particles, volume, and adiabatic ramp time, this measurement is operated at the edge of the coherence time of our qubits. To extract consistent signal, we play a few tricks. First, which of the qubits participate in the highest energy eigenstate in the disordered configuration depends on which qubits we place highest in frequency. Therefore, we can arbitrarily choose which qubits to use for any given eigenstate (limitations: neighbors need to start properly detuned so that disordered state is separable). For volumes V less than 7, we can also choose different contiguous sets of qubits as our volume for that experiment. To find the configuration with best coherence and least noise for a given superposition, we cycle through qubits, volume sets (where possible), and ramp times, until we hit a combination that has a peak of prominence 6σ above background noise after applying a digital low-pass filter cutting off frequency components below 20 MHz with the Ramsey virtual frequency chosen to fall between 30 MHz and 100 MHz (see SI B.1). We then repeat the experiment

to acquire error bars on peaks.

In order to have small qubit-readout crosstalk, when reading out we place the qubits in a stagger with nearest-neighbor detuning $\gg U$. For Fig. 6.2 and Fig. 6.3 superpositions were prepared directly from this point. When preparing superpositions of states for Fig. 6.4 and Fig. 6.5 however, since some states at higher densities involve nearest neighbors, to avoid unwanted crossings with the U-band, qubits were first populated with photons, then rapidly jumped from their readout position to a stagger with nearest-neighbor detuning less than U and qubit position chosen to minimize hybridization. We found we suffered minimally from Landau-Zener transitions (i.e. unwanted population transfer between nearest-neighbors during rapid ramps) and were consistently able to choose staggers where eigenstates still consisted of local qubit states. The adiabatic melt was then performed from this smaller stagger.

Data is plotted with ω_{lat} subtracted off, such that the theory and data curves are centered around 0.

B.2.2 Pressure

We apply a similar procedure to measure pressure, with one extra step. As a reminder, to measure the energy of N particles in V vs $V+1$ sites in order to extract pressure, we detune an edge qubit by the anharmonicity, and place that qubit into a superposition of $|0\rangle$ and $|1\rangle$ to make the qubit $|2\rangle$-state in a superposition of being accessible vs not to the rest of the lattice. However, when tunneling into the $|2\rangle$-state, the tunneling is Bose-enhanced by a factor of $\sqrt{2}$. As a sanity check, we measure energy differences in this configuration and compare to an exact numerical model, where we indeed see the spectrum affected by the Bose-enhanced tunneling to the edge site (see Fig. SB.1). To suppress this extra tunneling, we frequency modulate [62] the edge qubit. When frequency modulating, in the rotating frame, the qubit effectively lives with amplitude given by $J_m(\frac{\epsilon}{2\nu_{sb}})$ at the base frequency

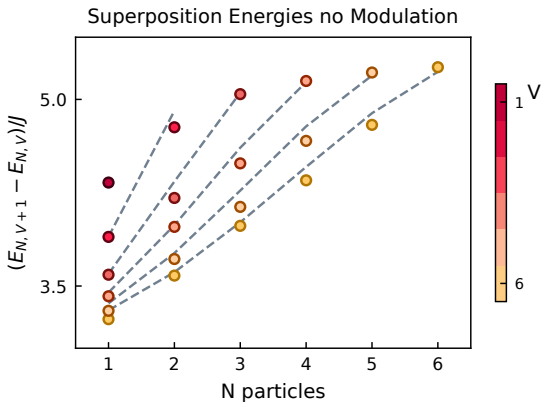

SI Fig. SB.1: **Interferometry of volume superpositions without modulating to correct for Bose-enhancement**. We measure $E_{N,V+1} - E_{N,V}$ for different particle numbers and volumes without modulating the edge qubit to correct for Bose-enhancement. Our measurements line up well with disorder-free numerics (grey dashed lines), confirming that there is low frequency disorder between the qubits before adding the extra complexity of the modulation step. Error bars, where larger than the data-point, reflect the S.E.M.

plus multiples m of the modulation frequency, where J is a Bessel function of the first order, ϵ is the strength of modulation in qubit frequency, and ν_{sb} is the sideband frequency. If one modulates at the right amplitude, one can engineer a $\sqrt{2}$ suppression of tunneling at the base frequency.

We choose to modulate at 100 MHz in order to have the higher sidebands be far enough detuned from the lattice to not affect its physics. Because the flux vs current curve of the qubits isn't linear, flux modulating also gives a DC offset term given by $\delta_{DC} = \frac{\epsilon_\phi^2}{4}\frac{d^2\nu_{01}}{d\phi^2}$ where ϵ_ϕ is the amplitude of modulation in terms of flux ϕ applied to the qubit and ν_{01} is the frequency of the qubit $|0\rangle$ to $|1\rangle$ transition. We calibrate the flux drive amplitude by fitting single qubit Ramsey frequency components to corresponding Bessel functions and measuring DC offset, see Fig. SB.2.

Applying the modulation from the start of the ramp of the disorder makes adiabaticity quite hard to achieve; the higher sidebands of the modulated qubit can interact with neighbors during the ramp. We found it easier to instead adiabatically ramp qubits onto

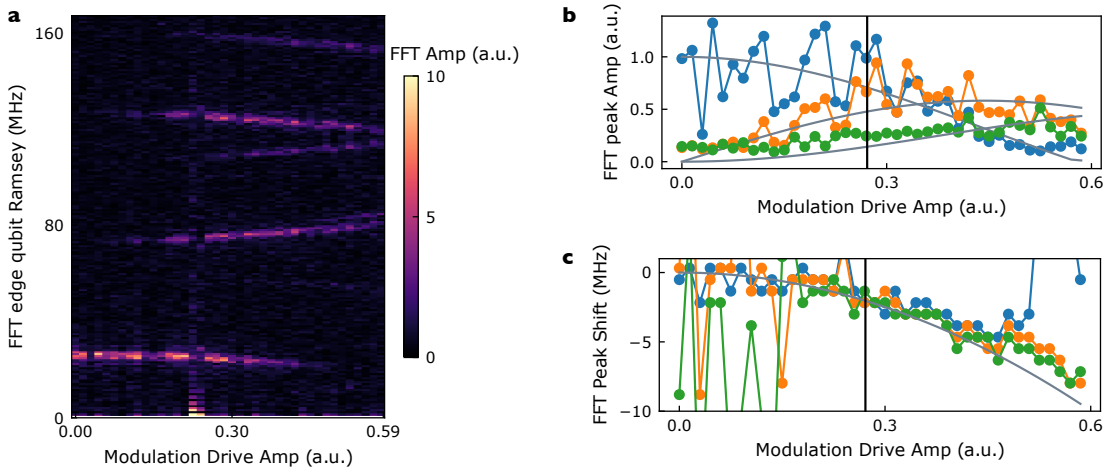

SI Fig. SB.2: **Modulation Calibrations**. We frequency modulate $Q6$, the lattice edge qubit, at 100 MHz and measure the corresponding Ramsey signal at different modulation amplitudes. In **a**, the Fourier transform of the corresponding $Q6$ Ramsey fringes are plotted vs modulation drive amplitude, with a 20 MHz virtual offset. The peaks correspond to the different sidebands, and the peaks' shift in frequency as a function of amplitude is the DC-offset caused by the the non-linearity in the qubit flux-frequency curve. Several of the peaks at higher frequency are frequency folded/aliased because of finite sampling bandwidth. In **b**, the first peaks at the first three sidebands are extracted and their amplitude plotted. By fitting these amplitudes to the expected analytic expressions (Bessel functions), we extract the modulation amplitude where the signal at the base qubit frequency (blue) is suppressed by a factor of $\sqrt{2}$, marked by the black vertical line. Using the same fit parameters as for the Bessel functions, we also fit the DC shift for the range of modulation drives in **c**. This fit is used to extract and correct for the DC shift detuning when modulating by tuning the qubit to compensate.

resonance, and then adiabatically turn on the modulation. In the code loop aiming to find good parameters, we also varied ramp time for turning on modulation.

Similarly to the data set for chemical potential, to get signal for a given superposition, we cycle through qubits, volume sets (where possible), and ramp times, until we hit a combination that has a peak of prominence 6σ above background noise after applying a digital low-pass filter cutting off frequency components below 20 MHz with a Ramsey virtual frequency chosen to fall between 30 MHz and 100 MHz (see SI B.1). The exception is for large volume and particle number: for $V = 7$ vs $V = 6$ sites at filling $N = 4, 5, 6$ there are no peaks 6σ above background noise. We instead choose peaks 4σ above the background noise

and apply a 30 MHz low pass filter (higher filter since because of our lower peak cutoff we are more susceptible to low frequency noise, and because these energy differences are expected to be higher in frequency).

B.2.3 Derivative

The x-axis point for a measurement comparing $y(x+1) - y(x)$ is $x + 0.5$. For example, for $E(N+1, V) - E(N, V)$, the density point in the plot is $\rho = (N + 0.5)/V$.

B.3 Souces of Deviation from Non-Interacting Fermion Analytics

B.3.1 Finite N and V effects

The gray theory curves plotted in Fig 6.4 and Fig 6.5 are theory for thermodynamic limit. However, our system is finite in size, and so deviates from this limit. Our data is better captured by finite-size analytics, see Fig SB.3.

B.3.2 Finite U/J Effects in a Finite Size System

Zooming in further reveals that at the next level of correction, our data also deviate from even the finite-size correction because of the interaction energy U being finite; the mapping to non-interacting fermions is not perfect, see Fig. SB.4.

B.4 Anharmonicity Disorder

We measured the Mott insulator gap at all lattice volumes, with $Q1$ as the qubit in a superposition of $|1\rangle$ and $|2\rangle$. However, because of strong variation in the qubits' anharmonicities, lattice configurations beyond $V = 2$ that include $Q2$ were effectively restricted to $Q0$ and $Q1$: $Q2$'s $|2\rangle$ is 26 MHz detuned from its neighbors, causing data at higher particle number

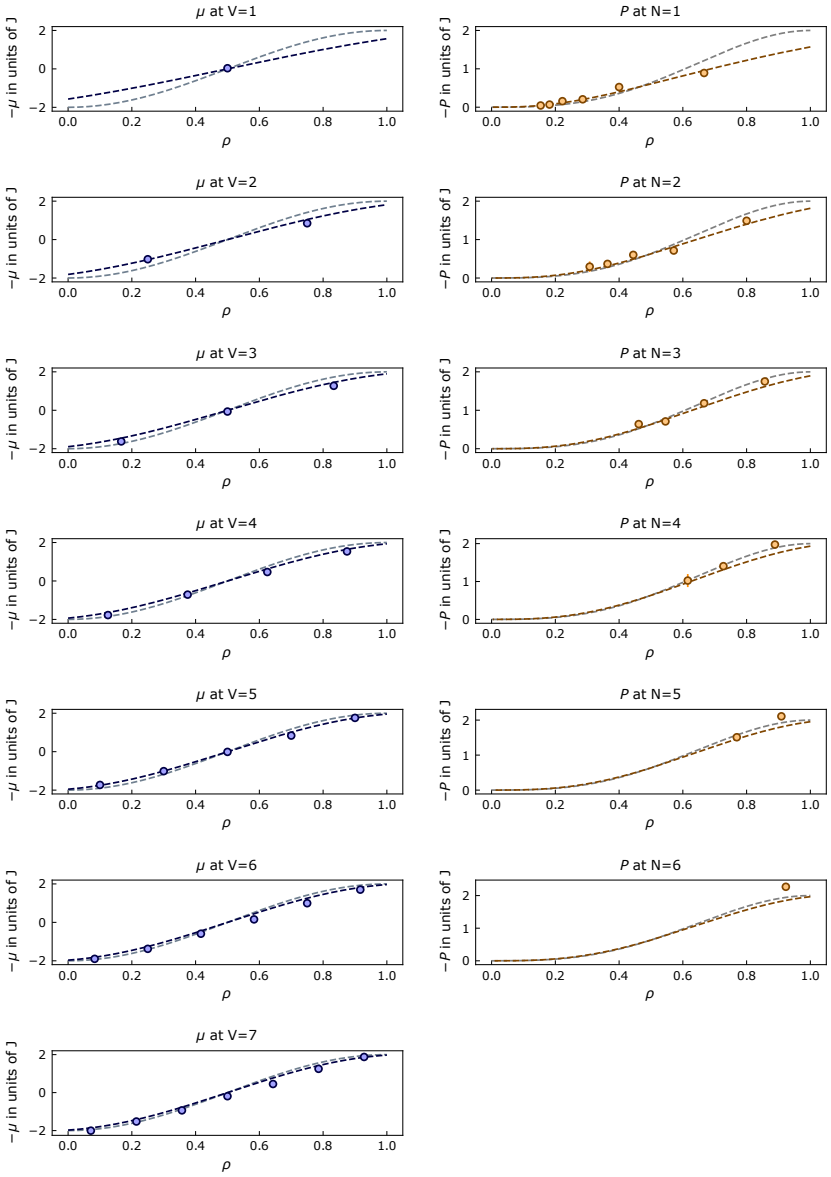

SI Fig. SB.3: **Finite Size N and V Effects in Chemical Potential and Pressure**. Grey dashed lines correspond to free fermion analytics in the thermodynamic limit, dashed colored lines correspond to free fermion analytics in finite size limit indicated by subplot title, and circles correspond to data. Error bars, where larger than the data-point, reflect the S.E.M.

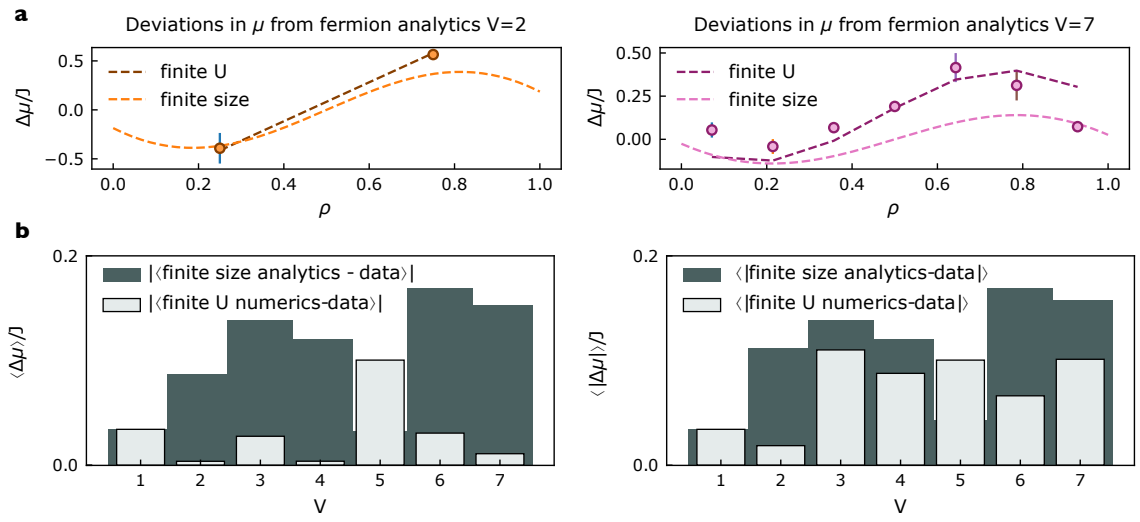

SI Fig. SB.4: **Example of finite U/J effects in chemical potential**. In **a**, we plot the deviation from the infinite size fermion chemical potential for finite size analytics (dashed light line), finite size & finite U numerics (dashed dark line), and our data (circles). In both representative volumes $V = 2$ and $V = 7$, it emerges that while there is scatter in the data, data agrees more closely with finite U & finite size numerics than just the finite size theory. In **b**, in the first panel, for each volume, we measure the average deviation between data and finite size fermion (ie infinite U) analytics (dark grey) and between data and numerics calculated with our finite experimental value of U (light grey). In the second panel, we plot the average of the absolute value of the deviation. These panels illustrate that while the magnitude of the deviation in the data between finite U numerics and infinite U analytics is similar, the data still agrees more closely with finite U numerics. Error bars, where larger than the data-point, reflect the S.E.M.

Qubit	1	2	3	4	5	6	7
$U_{\text{lattice}}/2\pi$ (MHz)	-236	-235	-209	-234	-236	-231	-225
$(U_{\text{lattice}} - U_{Q1})/2\pi$ (MHz)	-1	0	27	1	-1	4	10

Table B.1: **Disorder in Qubit Anharmonicity**

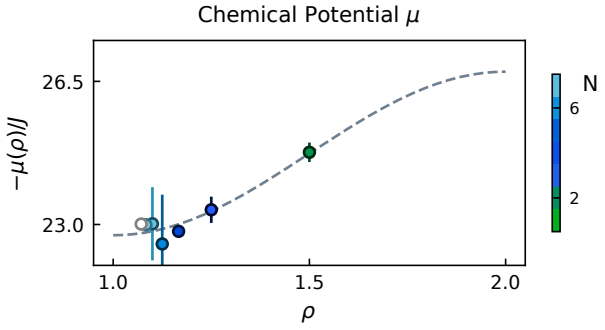

SI Fig. SB.5: **Chemical Potential Above Mott Insulator Gap**. We plot the energy difference between the lattice being fully filled and the lattice being fully filled with one particle band of second excited states U below the first band. Because of Bose enhancement, the effective tunneling in this second band is $2J$, reflected in the grey dashed lines from non-interacting fermion analytics. Because of lattice site disorder, data deviates from free fermion analytics at higher volumes (i.e. lower densities in plot above since particle number here is fixed at $N = 1$). Error bars, where larger than the data-point, reflect the S.E.M.

to deviate from values expected in an uniform-U case.

B.5 Same Particle Manifold Superpositions

We perform a two-qubit gate, preparing the state $\frac{1}{\sqrt{2}}(|01\rangle + |10\rangle)$ between two qubits, to create a superposition of these eigenstates at when the qubits are far detuned from each other, in the stagger configuration. There are several ways to enact a two qubit gate: the way we choose here is to π-pulse one qubit, bring it in resonance with its neighbor for half the J tunneling time, and then jump both qubits back to the stagger. We then proceed with the reversible adiabatic ramp protocol as normal. In Fig. SB.6**a** we prepare and measure density profiles for two different single particle states at the stagger and at the lattice degeneracy point where all the qubits are on resonance, as well as the density

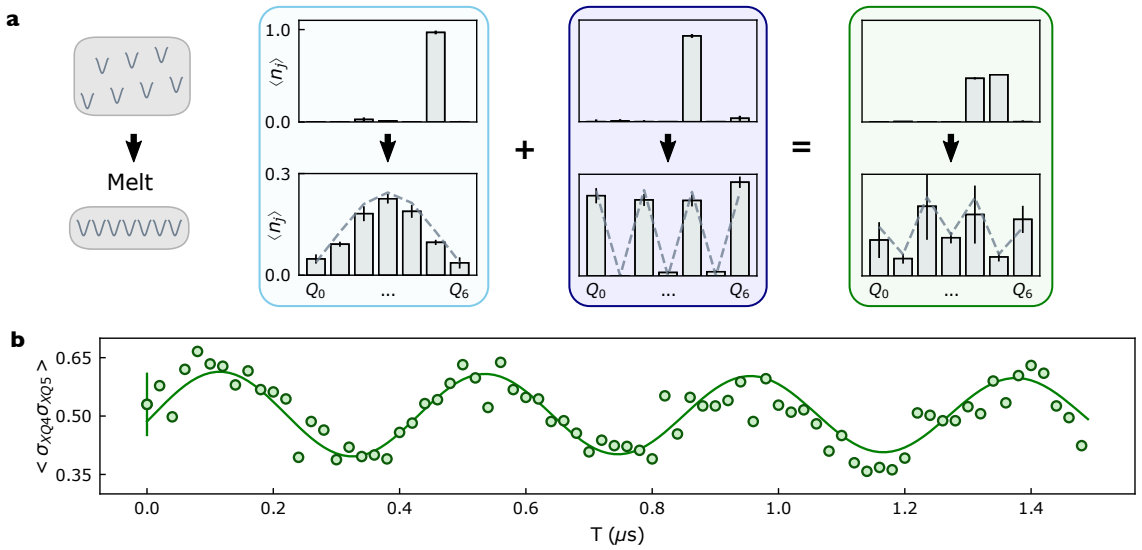

SI Fig. SB.6: **Same Particle Manifold Superpositions**. In **a**, we create and measure density profiles for two different one-particle states, and their superposition, at the disordered stagger position and at the lattice position. We then record the Ramsey beating between the two states by measuring $\langle \sigma_{XQ4}\sigma_{XQ5} \rangle$ in **b**. Representative error bars reflect the S.E.M.

profile for their superposition. We extract the Ramsey trace by measuring $\langle \sigma_{XQ4}\sigma_{XQ5} \rangle$ in Fig. SB.6**b**, which is within 3 MHz of the expected value.

B.6 Compressibility

The compressibility reflects how much the pressure changes with volume. In Fig. SB.7 we compare compressibility computed by differentiating pressure data ($\kappa_s^{-1} = -V\frac{\partial P}{\partial V}$) to compressibility computed by differentiating chemical potential data ($\kappa_s^{-1} = V\rho^2 \frac{\partial \mu}{\partial N}|_S$). The agreement that we find further validates that the equation of state is intensive (dependent on particle number and system size only through density).

We calculate the compressibility by taking numeric N and V derivatives of μ and P. The thermodynamic compressibility at constant entropy and particle number is defined as

$$\kappa_s^{-1} = -V\frac{\partial P}{\partial V}\bigg|_{S,N}. \tag{SB.1}$$

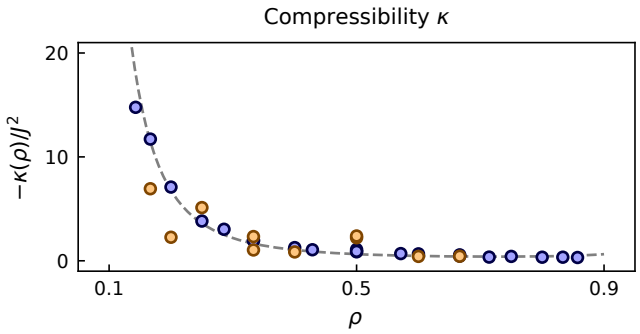

SI Fig. SB.7: **Compressibility**. We plot the quantum fluid compressibility at different density points by differentiating pressure data (orange) and chemical potential data (blue). Error bars, where larger than the data-point, reflect the S.E.M.

However, with this expression, we can only take a numeric derivative of our pressure data set with respect to volume; it would be be nice to use our chemical potential data set as well.

In the thermodynamic limit, the Gibbs-Duhem expression holds, which states

$$0 = -V\partial P + S\partial T + N\partial\mu. \tag{SB.2}$$

Since we are at $T = 0$, this implies $\partial P = N/V\partial\mu = \rho\partial\mu$. Therefore,

$$\kappa_s^{-1} = -V\frac{\partial P}{\partial V}\bigg|_{S,N} = -N\frac{\partial\mu}{\partial V}\bigg|_{S,N} = -N\frac{\partial}{\partial V}\bigg|_{S,N}\frac{\partial E}{\partial N}\bigg|_{S,V}. \tag{SB.3}$$

We flip the order of the derivatives, and once again replace $\partial P = N/V\partial\mu = \rho\partial\mu$ to get the expression $\kappa_s^{-1} = -V\rho^2\frac{\partial^2 E}{\partial N^2}\Big|_{S,V}$ [76].

B.7 Disorder Correction

Ensuring that the qubits in the on-resonance lattice configuration are degenerate in frequency is extremely important when measuring pressure and chemical potential. For several densities, the energy differences between ground states are on the order of a few MHz; lattice

disorder can cause significant error in the quantities we are attempting to measure. Using our RF flux crosstalk matrix correction and measured qubit $\omega_{01}(\phi)$ relations, we are able to place qubits within $1-2$ MHz of the desired lattice frequency. To ensure we hit lattice degeneracy to the required precision, we feed back on the local $\omega_{01}(\phi)$ relations by comparing our manybody profiles to expected theory. To ensure our corrections are robust, we feed back on a full set of manybody profiles at $V = 7$: the ground state for $N = 1$, $N = 2$, and $N = 3$. Using this method, we are able to achieve error on the order of $200-400$ kHz, which is the same order of magnitude as experiment-to-experiment qubit frequency drift.

It is also important that the qubits not only be on resonance with each other, but also that we know what lattice frequency they are being placed at after the round of corrections described above. Energy differences between eigenstates of different particle number depend on what energy the particles are at. To ensure we are normalizing correctly (see Sec 2.4), it is important that we actually be placing our lattice at the expected frequency. Feeding back on profiles helps correct for relative detuning between qubits, but does not give us insight into the absolute lattice frequency. To measure this quantity, we first measure via standard Ramsey interferometry the frequency of individual qubits brought to the lattice one at a time using the disorder corrections calculated from feedback back on profiles. Usually there is some scatter (from an imperfect crosstalk matrix); we take the average of this scatter. Recent results have shown that using machine learning on flux crosstalk matrices allows for very low disorder [83], this would be a better solution going forward.

B.8 Error and Uncertainty Calculations

For each experiment in Fig. 6.2, we measure 2000 shots, bin the shots, apply relevant confusion matrices, and extract the averaged quantity of interest (in this case, Ramsey traces). We then repeat the experiment 10-11 times. Because of the long ramp times and wait times in the experiment, very small frequency variations experiment-to-experiment cause large phase

variations in our measurement. We calculate the starting phase in each trace from fits, and numerically zero the phase. We then calculate the mean of the averages and standard deviation of the resulting traces (i.e. calculate the standard error of the mean, or S.E.M.) for the values and error bars that we report in this figure. The experiment repetitions are performed close in time (typically within a 10-30 minute span) so that our error bars are not affected by slow experimental drifts over hours or days.

For error bars in Fig. 6.4 and Fig. 6.5 come from repeating the procedure described in SI B.2 3 times and 10-15 times respectively, then taking the mean and standard deviation of the collections of measured peaks. We then propagate the error to gain the error bars in Fig. 6.2**c**, **f**, and **g**. The exception is the U-detuned point in **c**, where we did not have enough repetitions of the data point. There, the error bar is the variance in a Lorentzian fit to the measured Ramsey peak.

Note that our error bars in Fig. 6.4 and Fig. 6.5 are smaller than points' deviation from exact numerical models of our system (average deviation of 700 kHz for particle number superpositions and 800 kHz for volume superpositions). This is likely because of residual frequency disorder (see SI B.7).

SUPPLEMENT C

DEVICE PARAMETERS

C.1 Device Details Chapter 5

Qubit	**1**	**2**	**3**	**4**	**5**	**6**	**7**
$U_{\text{lattice}}/2\pi$ (MHz)	-241	-240	-240	-239	-239	-239	-240
$J_{i,i+1}/2\pi$ (MHz)	9.0625	9.032	8.842	8.936	9.023	9.040	–
$\omega_{\text{disorder-large}}/2\pi - 4000$ (MHz)	410	992	466	956	513	1020	489
$\omega_{\text{disorder-small}}/2\pi - 4000$ (MHz)	742	860	767	875	782	890	797
$T1(\mu s)$	14.6	35.5	57.7	28.4	60.3	54.7	40.0
$T2^*(\mu s)$	0.85	0.64	1.31	0.77	3.57	0.84	1.4
$\text{fidelity}_{\text{ge}}$	0.91	0.92	0.93	0.95	0.87	0.92	0.83
$\omega_{\text{read}}/2\pi$ (GHz)	6.197	6.323	6.556	6.78	6.871	6.655	6.427
$\kappa_{\text{read}}/2\pi$ (KHz)	359	553	203	235	292	220	894
$g_{\text{rd-qb}}/2\pi$ (MHz)	60	63	72	64	78	70	70
$\chi_{\text{rd-qb}}/2\pi$ (MHz)	0.48	1.23	0.78	1.24	0.90	1.71	0.73
$\omega_{\text{purcell}}/2\pi$ (GHz)	6.256	6.486	6.706	6.936	7.055	6.843	6.604
$\kappa_{\text{purcell}}/2\pi$ (MHz)	77.5	52.7	92.5	72.4	103.1	56.9	60.8
$g_{\text{rd-pf}}/2\pi$ (MHz)	3	3.5	6	6.5	5	6	4.5

Table C.1: **System Parameters Chapter 5**

C.2 Device Details Chapter 6

Qubit	**1**	**2**	**3**	**4**	**5**	**6**	**7**
$U_{\text{lattice}}/2\pi$ (MHz)	-236	-235	-209	-234	-236	-231	-225
$J_{i,i+1}/2\pi$ (MHz)	-9.62	-9.58	-9.63	-9.74	-9.76	-9.63	–
$T1(\mu s)$	14.6	35.5	57.7	28.4	60.3	54.7	40.0
$T2^*(\mu s)$	0.85	0.64	1.31	0.77	3.57	0.84	1.4

Table C.2: **System Parameters Chapter 6**

The optimal lattice frequency varied on a scale of weeks depending on the frequency distribution of low lifetime defects. For data taken for Fig. 6.2 we used lattice frequency 5.31 GHz, for Fig. 6.3 we used lattice frequency 4.820 GHz, and for Fig. 6.4 and Fig. 6.5 we used lattice frequency 5.0 GHz. Our qubit $T1$s and $T2$s similarly varied over time, with the average $T1 = 40$ µs and average $T2^* = 1.3(\mu s)$. Our qubit T2 times when all the qubits are on resonance improve, since because of the avoided crossings the eigenvalue vs flux curves become flatter (we generate our own sweet spot). We did not quantitatively measure this effect.

The RF crosstalk measured at 100 MHz for experiments involving modulation in this work is lower, close to $2 - 3\%$. The next-to-nearest neighbor expected to be of magnitude $\approx 0.06 \times J$ from microwave finite-element simulations. The tunable transmon SQUID consists of two asymmetric square-shaped junctions with sizes of 130 nm and 230 nm, embedded in a loop of dimension 20 μm by 8 μm.

SUPPLEMENT D

FABRICATION

D.1 Fabrication Recipe

The sample is a 10×20 mm sapphire chip with a tantalum base layer and aluminum Josephson junctions and SQUID loops. Our substrate is a 450 μm thick C-plane sapphire wafer that has been annealed at 1500° C for 2 hours, solvent cleaned, etched in 80°C Nano-Strip® for 10 min, and then etched again in 140° C sulfuric acid to fully remove all contaminants [146]. The large scale features of the device are defined using optical lithograpy. The base layer is 200 nm of tantalum deposited at 800° C, then patterned with a direct pattern writer (Heidelberg MLA 150) and wet etched in HF. Next, the junctions and SQUID loops are defined with electron beam lithography, using an MMA-PMMA bilayer resist, written on a Raith EBPG5000 Plus E-Beam Writer. The Al/AlOx/Al junctions are e-beam evaporated in an angled evaporator (Plassys MEB550). Before Al deposition, Ar ion milling is used on the exposed Ta to etch away the Ta oxide layer in order to ensure electrical contact between the Ta and Al layers. The first layer of Al (60 nm, deposited at 0.1 nm/s) is evaporated at an angle of 30° to normal, followed by static oxidation in O_2 for 24 minutes at 50 mBar. The second layer of Al (150 nm, 0.1 nm/s) is then evaporated at 30° to normal but orthogonal to the first layer in the substrate plane to form the Manhattan-style junctions.

After fabrication, the E_J of a junction can be estimated by measuring the junction's room temperature resistance (you cannot individually measure each junction in a SQUID loop, so we made test structures with each half of the SQUID loop and measured those). The quantities are related by:

$$E_J = \frac{\Phi_0 I_c}{2\pi} \tag{SD.1}$$

$$= \frac{\Phi_0}{2\pi}\frac{\pi\Delta}{2Re} \tag{SD.2}$$

where Δ is the superconducting gap, Φ_0 is the magnetic flux quantum, e is the electron charge, and R is the room temperature resistance of the junction.

D.2 Packaging

The device is then mounted and wirebonded to a multilayer copper PCB. The ground plane around the device features is also heavily wirebonded to avoid slotline modes and to fully connect the ground plane across the chip. The device is enclosed in an OFHC copper mount designed to eliminate spurious microwave modes near our operating frequencies. The copper enclosure has a solenoid mounted on top for global flux tuning.

SUPPLEMENT E

MEASUREMENT SETUP

The packaged sample is mounted to the base plate of a BlueFors dilution refrigerator at a nominal temperature of 8 mK. A solenoid of coiled niobium-titanium (NbTi) wire is fixed to the packaged sample to provide a global bias field with little heating, useful for getting close to desired lattice flux bias point without driving to much current through the DC flux lines. The sample is placed in a heat-sunk can consisting of a thin high-purity copper shim shield, followed by a high-purity superconducting lead shield, followed by two μ-metal shields (innermost to outermost) to provide additional shielding from radiation and external magnetic fields.

The experimental setup is shown in SE.1. All input and flux lines have Eccosorb (CRS-117) filters at base to protect the sample from IR radiation. A Keysight PNA-X N5242 is used to perform spectroscopy of the readout resonators/Purcell filters and to measure the flux tuning curves of each qubit. For experiments, a SignalCore SC5511A is used to generate an LO tone near the qubit frequency. This tone is windowed using a custom-built microwave switch, then I/Q modulated by a Keysight PXIe AWG (M3202A, multichannel, 1 GS/s) to generate the individual qubit drive pulse. There are two copies of this qubit drive setup, enabling simultaneous pulses to the qubits staggered both above and below the lattice frequency, a bandwidth otherwise inaccessible with the 1 GS/s AWG. The readout tones are also generated with SC5511A SignalCores windowed by microwave switches. There are two readout LOs, enabling simultaneous two-qubit readout. The qubit drive and readout pulses are combined outside the fridge and sent to the sample on a common input line. The output signal coming from the chip passes through three cryogenic isolators (64 dB total isolation) at base, then travels via a NbTi low-loss superconducting line to the 4K plate where it is amplified by a Low Noise Factory HEMT amplifier.The output signal coming out of the fridge passes through additional room temperature amplifiers (Miteq AFS3-00101200-22-

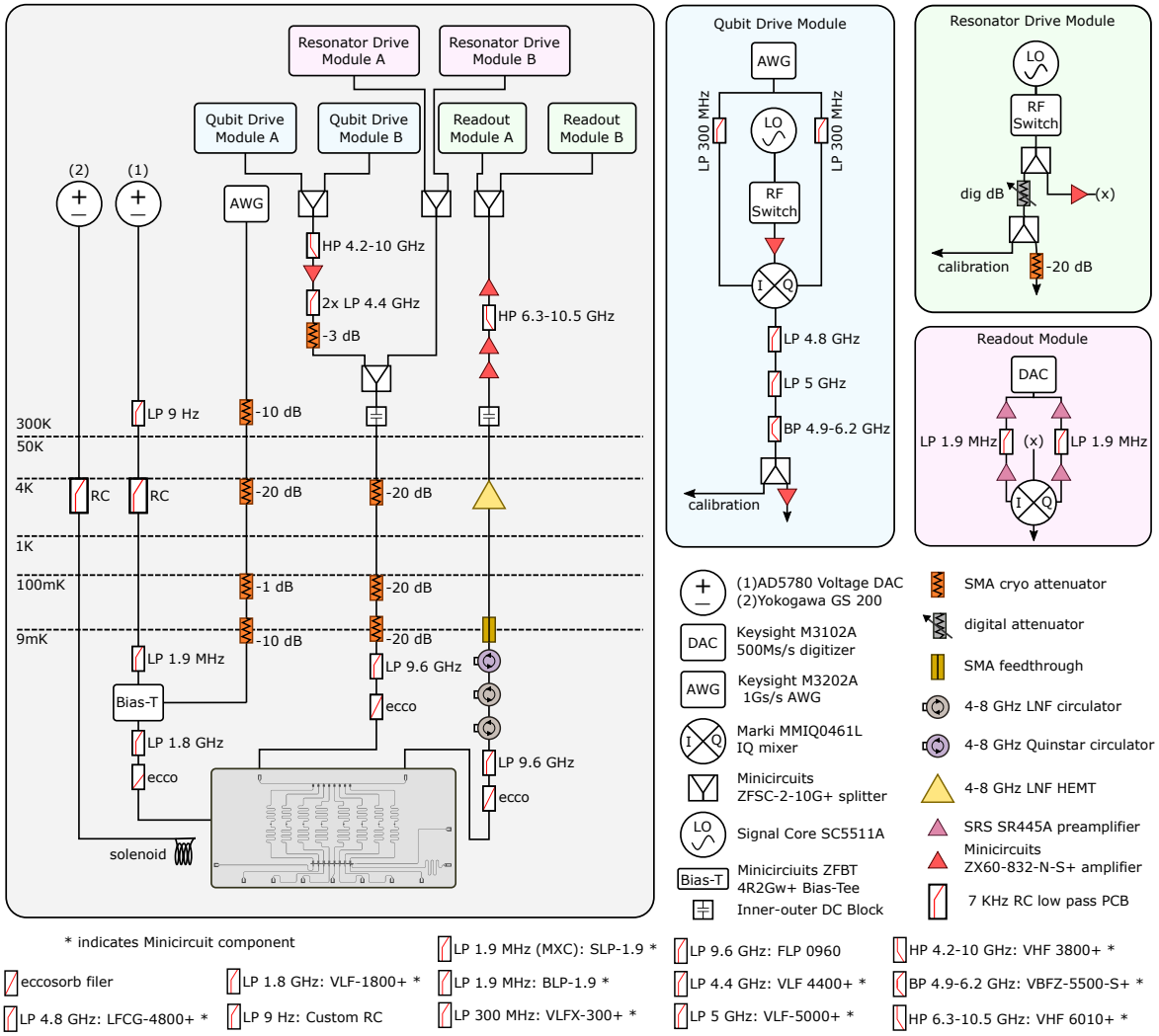

SI Fig. SE.1: **Experiment Setup** Schematic drawing of cryogenic and instrumentation setup.

10P-4, Minicircuits ZX60-123LN-S+). The signal is then split and demodulated against both of the readout LO tones using an I/Q mixer, and recorded using a fast digitizer (Keysight M3102A, 500 MSa/s). DC and RF pulses are combined at a MiniCircuits Bias Tee (ZFBT-4R2GW) with the capacitor removed before traveling to the chip. Each qubit has its own combined RF+DC flux line.